

ATOMISTIC SIMULATION OF GRAPHENE–POLYURETHANE  
NANOCOMPOSITE FOR USE IN BALLISTIC APPLICATIONS

A Dissertation

by

JEAN LEAH NJOROGE

Submitted to the Office of Graduate Studies of  
Texas A&M University  
in partial fulfillment of the requirements for the degree of

DOCTOR OF PHILOSOPHY

Chair Committee           Tahir Cagin  
Committee Members:    Zhengdong Cheng  
                                  Anastasia Muliana  
                                  Hong Liang  
Intercollegiate Faculty Chair: Ibrahim Karaman

August 2013

Major Subject: Materials Science and Engineering

Copyright 2013 Jean Leah Njoroge

## ABSTRACT

Exposure to high impact velocity is the principle limiting factor of material performance in ballistic applications for use in civilian and defense industries. Graphene has emerged as a material of scientific interest due to its exceptional mechanical and thermal properties. When incorporated appropriately in a polymer matrix, graphene can significantly improve properties of polymers at small loading, while preserving the integrity of the polymer. Graphene based polymer nanocomposites provide a novel approach for material design for ballistic applications. The reliability of graphene/polymer nanocomposites on end use applications depends on understanding the effect of structure-property relationship of nanocomposite.

A first approach to engineering nanocomposite for ballistic applications requires thorough understanding of physical properties change with incorporation of nanofillers in polymer matrix. One significant class of properties tremendously affected by inclusion of nanofiller is thermodynamic properties. Therefore, a first investigative study, we explore non-linear elastic behavior of graphene using first principle method, specifically Density-Functional Theory (DFT), and atomistic simulation. Using DFT, we calculated the equation of state (EOS) and elastic constants of graphene. The results are in agreement with experimental and other theoretical studies using DFT. However, accuracy of atomistic simulations is limited by empirical potentials. Nevertheless, general anisotropic, non-linear mechanical behavior of graphene is evident on both approaches.

Additionally we use molecular dynamics (MD) simulations to study effect of graphene nanofiller on thermo-mechanical properties of polyurethane. We have calculated thermodynamic, structural and mechanical properties of the amorphous polyurethane and its graphene nanocomposite. Our results show significant enhancement of thermal-mechanical properties. The final part of this dissertation, we used non-equilibrium molecular dynamics (NEMD) simulations to investigate dynamic response behavior of polyurethane and its graphene nanocomposite. Calculation of Hugoniot states of polyurethane agrees with experimental studies. However, a phase change phenomenon observed in experimental work was not visible in the present work. This is due to bond breaking and formation, which is a

clear characterization of phase changes. Graphene-polyurethane nanocomposites demonstrate similar shock wave propagation illustrating characteristics of impeding shock wave when subjected to different particle velocities. This is due to graphene inducing stress concentrations in the composite, which may increase yield strength.

## ACKNOWLEDGEMENTS

I would like to express my gratitude to my advisor Professor Tahir Cagin, for his patient, support and mentorship throughout my PhD journey at Texas A&M University; his continuous guidance was not only of fundamental importance for the development of this thesis, but also for my professional growth. My appreciation also goes to Prof. Anastasia Muliana, Prof. Zengdong Cheng, and Prof. Hung-Jue Sue for serving in my committee, and for their time, and insightful suggestions along the way to make this dissertation possible. Prof. Hong Liang for her time in evaluating my final exam on this dissertation.

Special thanks to my group fellows for the support and creating a joyful environment to work in, I will never forget the good moments we have gone through, and I strongly hope that our paths cross again in the future. I would like to thank Dr. Arnab Chakrabarty and Dr. Bedri Arman for sharing their knowledge, discussions and contributing to this dissertation.

I am deeply grateful to Lisa J. Kibutu and Peter Mbugua, Dr. Macharia Waruingi, Ruthie Mbeche, Timothy and Dr. Faith Kairo, and Dr. Tennyson Maliro for the their support at various stages of my PhD experience. Your words of encouragement and support have been invaluable. Last but not least, this dissertation is dedicated to my grandparents, parents, brothers and sisters; nieces and nephews for their endless care, support, patient and love that has kept me so motivated in achieving my goals.

# TABLE OF CONTENTS

	Page
ABSTRACT.....	ii
ACKNOWLEDGEMENTS.....	iv
LIST OF FIGURES.....	vii
LIST OF TABLES.....	xi
1. INTRODUCTION.....	1
1.1. Background and Motivation.....	1
1.2. Objective.....	4
1.3. Dissertation Layout.....	5
2. LITERATURE REVIEW.....	8
2.1. Polyurethane.....	8
2.2. Graphene.....	11
2.3. Overview of Graphene for Composite Filler.....	16
3. COMPUTATIONAL METHODS FOR MATERIAL SIMULATIONS.....	20
3.1. Quantum Mechanics and Density Functional Theory.....	23
3.2. Molecular Mechanics and Molecular Dynamics.....	26
3.2.1. Molecular Mechanics.....	27
3.2.2. Molecular Dynamics.....	30
4. NONELASTIC BEHAVIOR OF GRAPHENE: FIRST PRINCIPLE AND MOLECULAR MECHANICS CALCULATIONS.....	38
4.1. Motivation.....	38
4.2. Theoretical Framework.....	41
4.2.1. Equation of State.....	41
4.2.2. Nonlinear Elastic Theory.....	42
4.3. Computational Details.....	48
4.4. Results and Discussion.....	50
4.4.1. Equation of State.....	50
4.4.2. Elastic Constants: Second and Third Order.....	53
4.5. Concluding Remarks.....	56

5. THERMAL- MECHANICAL PROPERTIES OF AMORPHOUS POLYURETHANE AND ITS GRAPHENE NANOCOMPOSITE .....	58
5.1. Motivation.....	58
5.2. Calculation of Properties .....	59
5.2.1. Elastic Constants by Molecular Mechanics .....	62
5.2.2. Elastic Constants by Molecular Dynamics .....	63
5.3. Computational Details .....	64
5.3.1. Generation of Amorphous Polymer Models .....	64
5.3.2. Graphene Structure .....	67
5.3.3. Graphene-polyurethane Nanocomposite Structure .....	68
5.4. Results and Discussion .....	71
5.4.1. Volume Dependence on Temperature .....	75
5.4.2. Evaluation Mechanical Properties .....	78
5.5. Concluding Remarks.....	83
6. DYNAMIC RESPONSE OF AMORPHOUS POLYURETHANE AND ITS GRAPHENE NANOCOMPOSITE TO SHOCK-WAVE LOADING.....	85
6.1. Motivation.....	85
6.2. Basics of Shock-wave Physics.....	87
6.2.1. Equation of State and Jump Conditions.....	88
6.2.2. Experimental Techniques.....	92
6.3. Computational Details .....	94
6.3.1. Generation of Polyurethane Model for Shock Simulation.....	94
6.3.2. Graphene-polyurethane Nanocomposite Consists of Graphene .....	95
6.3.3. Shock Simulations .....	96
6.4. Results and Discussion .....	98
6.4.1. Shock Response in Polyurethane .....	98
6.4.2. Shock Response in Nanocomposite.....	104
6.5. Concluding Remarks.....	105
7. SUMMARY .....	106
REFERENCES .....	109
APPENDIX.....	123

## LIST OF FIGURES

	Page
Figure 1: Schematic of the relationship between time and length scales for multi-scale simulation methodology[26] .....	3
Figure 2: Schematic of basic reaction scheme of urethane formation .....	8
Figure 3: Structure of segmented polyurethane (a), two-phase structure of the bulk polymer (b)[29]. .....	9
Figure 4: Molecular structure of monomer of linear polyurethane ( $[C_{12}H_{24}N_2O_4]$ ).....	10
Figure 5: Monomer of polyurethane matrix model from material studio.....	10
Figure 6: Some allotropes of carbon, fullerene, graphene and single walled carbon nanotube[42]......	12
Figure 7: Schematic of (a) honeycomb crystal lattice of graphene (b) graphene lattice with two atoms representation of unit cell. ....	13
Figure 8: Potential application of graphene.....	16
Figure 9: Illustration of the interdependence of methods and the nature of experiment, theory and simulations. ....	20
Figure 10: An illustrative view of periodic boundary conditions.....	31
Figure 11: Undeformed graphene lattice; four-atom unit cell enclosed by rectangular red-dashed line in sub-lattice A. Two atom unit cell enclosed by rhombohedron red-dashed line in sub-lattice B.....	43
Figure 12: Orthonormal structure of graphene used for molecular mechanics simulations, with 4 graphene per unit cell and 240 atoms per simulations box.....	49
Figure 13: EOS fit for graphene under hydrostatic pressure showing a variation of atomic energy as a function of lattice constant in orthogonal graphene with 2 atoms and 4 atoms using DFT calculations. ....	51

Figure 14: EOS fit for graphene under hydrostatic pressure showing a variation of atomic energy as a function of lattice constant in orthogonal graphene monolayer structure with 128 atoms using molecular mechanics (MM) calculations. ....	53
Figure 15: Energy-strain response for uniaxial strain in armchair, zigzag and equibiaxial strain for graphene with (a) 4atoms per unit cell and (b) 2 atoms per unit cell. ....	53
Figure 16: Energy per atom versus strain of graphene monolayer under uniaxial stretch using molecular mechanics approach using (a) New_Tersoff and (b) Tersoff, potential functions. ....	56
Figure 17: Monomer of polyurethane matrix (a) schematic (b) material studio model. ....	65
Figure 18: Atomic model for (a) pristine graphene (C680) (b) pristine graphene with hydrogen end groups G(H)-(C620H70). ....	69
Figure 19: Snapshot of Gr-PUR nanocomposite structure with graphene at the bottom of simulations cell; (right) snapshot of Gr-PUR nanocomposite with graphene flakes at the bottom of the bottom of the simulations cell. ....	69
Figure 20: Volume (a) and total energy (b) evolution during the equilibration of the individual polyurethane samples (PUR-1–PUR-5) at 300K and 1atm. ....	70
Figure 21: Combined volume (a) and total energy (b) evolution during the equilibration of the initial polyurethane sample at 300K and 1atm. ....	71
Figure 22: Density vs. time plots of (a) pristine polyurethane, (b) nanocomposites of 14wt% and 17wt% of graphene nanosheet in polyurethane, and (c) 13wt% of graphene flakes in polyurethane. ....	73
Figure 23: RDF of entire system for pristine PUR and graphene nanocomposite. ....	74
Figure 24: Graphs of (a) average RDF for the equilibrated polyurethane models (b) the V-T curves at 1atm from NPT dynamics, the arrow locates the position of the $T_g$ as determined from the MD simulations. ....	75
Figure 25: Specific volume vs temperature for (a) PUR vs. PUR+ graphene flakes, (b) PUR vs. PUR with 14wt%graphene sheet (c) comparison of PUR nanocomposite with 14wt% and 17wt% graphene (d) comparison of PUR and PUR with 17wt% graphene. ....	76
Figure 26: Temperature vs. volume of simulates samples of amorphous polyurethane models. ....	77



Figure 27: Comparing amorphous polyurethane models in terms of uniaxial deformation in xx and zz using molecular dynamics simulation in NPT ensemble at 300K.....	79
Figure 28: Average volume/monomer vs. pressure curve of polyurethane models. ....	81
Figure 29: Schematic of rigid piston moving and driving shock into compressible fluid[172]. ....	88
Figure 30: A schematic diagram of shock wave conditions with density $\rho_0$ , particle velocity $u_p$ , shock velocity $u_s$ pressure (P), energy (E) and volume (V) before and shock wave and after shock wave.....	89
Figure 31: Shock pressure vs particle velocity for some standard materials [176]. ....	90
Figure 32: P-V Hugoniot curve and the Rayleigh line relationship ([172]).....	91
Figure 33: Hugoniot (OH curve), HR is the isentropic release paths and OH straight line is the Rayleigh line[172]......	92
Figure 34: Graphene-polyurethane composite molecular level computational cell with graphene positions in (a) Zhi and (b) at the origin Zlow, density $0.845\text{g/cm}^3$ . ....	95
Figure 35: Energy and pressure profiles for polyurethane $2 \times 2 \times 4$ 9(128 640 atoms) super cell structure at 1 atom and 300 K using NVT-MD.....	97
Figure 36: Energy and pressure profiles for polyurethane $2 \times 2 \times 4$ 9(128 640 atoms) super cell structure at 1 atom and 300 K using NVT-MD.....	98
Figure 37: Spatial shock wave profiles as a function of propagation distance, with piston velocity of (a)0.1km/s , (b) 0.5m/s, (c)1.0km/s (d) 1.5km/s , (e) 2.0km/s and (f) 2.5km/s respectively in amorphous polyurethane from MD simulations.....	99
Figure 38: Molecular-level computational analysis of (a) Hugoniot of relations particle-velocity dependence of the shock velocity for pristine amorphous polyurethane from direct MD shock simulations, and (b) For comparison, similar polymer (polyuria) experimental results obtained in the study of Mock et al. [25] and the ones predicted by the continuum-level polyurea material model of curve labeld Grujicic et al. [1] are also displayed. ....	100
Figure 39: Shock velocity vs particle velocity of PMM, (adapted from ref [182]), to highlight the curvature that characterizes the three different regimes found in polymers under shock compression.....	101

Figure 40: Graphs of (a) Hugoniot stress vs. particle velocity (b) Hugoniot stress versus strain of amorphous polyurethane using MD simulations. .... 103

Figure 41: Spatial shock wave profiles as a function of propagation distance, with piston velocity of (a)0.1km/s , (b) 0.5m/s, (c)1.0km/s , and (d) 1.5km/ respectively in Graphene-polyurethane (Gr-pur) from MD simulations. .... 103

Figure 42: Shock profiles of (a) shockspeed ( $U_p$ ), stress ( $P_{zz}$ ) and with piston velocity of 1.5km/s after 800ps respectively of graphene-polyurethane nanocomposite at Zhi (Gr-pur Zhi), at Zlow (Gr-pur Zlow), and amorphous polyurethane (pur) from NEMD simulations..... 105

## LIST OF TABLES

	Page
Table 1: Physical properties of carbon based materials. The mass density of graphene represents the two-dimensional graphene layers in $\text{g}/\text{cm}^2$ .....	14
Table 2: Mechanical, thermal and electrical properties of graphene, CNT, and polymeric materials .....	18
Table 3: Different type of interactions for that define a force-field .....	29
Table 4: EOS parameters for graphene using first principle and molecular mechanics atomistic simulations .....	52
Table 5: Elastic constants calculated from (a) first principle approach based on density functional theory (DFT) (b) molecular mechanics approach based on inter-atomic potential and (c) experimental values for comparison.....	55
Table 6: Characteristic of computational models polyurethane systems.....	65
Table 7: Initial density, final density and potential energies of polyurethane samples .....	72
Table 8: Bulk densities of polyurethane in pristine PUR and in nanocomposite. ....	73
Table 9: Calculation from glass transition temperature ( $T_g$ ), coefficient of thermal expansion above and below $T_g$ , Specific heat ( $C_p$ ), Isothermal compressibility ( $KT$ ) and bulk modulus ( $K$ ) from atomistic simulations.....	78
Table 10: Elastic constants of amorphous polyurethane calculated by molecular mechanic approach: $C_{11}$ - $C_{23}$ are elastic constants in Gpa, bulk modulus ( $B$ ), young modulus ( $Y$ ), shear modulus ( $G$ ) in Gpa and Poisson's ratio $\nu$ .....	78
Table 11: Elastic constants of amorphous polyurethane calculated by molecular dynamics approach, modulus in Gpa.....	80
Table 12: Bulk modulus $K$ for various polyurethane models by hydrostatic pressure .....	82
Table 13: Elastic constants, bulk modulus, young modulus and Poisson's ratio of pristine polymer, graphene and graphene flakes calculated from stiffness matrix .....	82
Table 14: Relationship between variables obtained during shock simulations .....	91

Table 15: Steps to generate shock simulation structure..... 95

# 1. INTRODUCTION

## 1.1. Background and Motivation

Continuous attacks and threats ranging from sniper fire on civilian targets to using improvised explosive devices (IEDs) have heightened safety concern from ballistic impact. A ballistic impact deals with variety of phenomena that begin when a projectile is propelled to a target, to when its effects are felt in the target. Ballistic impact exhibits high velocity impact in the range of 0.05 to 2km/s[1, 2]. High velocities impacts are developed from firearms or explosive fragments propelled through air into other objects in defense applications, or bird strike in engine for aviation industry. The greatest threat during ballistic impact comes from explosive fragments. Debris from pieces of equipment, walls, shattered window glass flying at high velocity cause extensive injury and loss of life. Consequently, resulting shock waves propagate through human body causing blunt trauma. Blunt trauma results in severe bruising, concussions, laceration, and damage to critical body organs, and eventually loss of life. Furthermore, shock waves incapacitate functional capability of sensitive sensors and instrumentation[1, 3, 4].

During ballistic impact, structures in defense, aerospace or transportation industry are exposed to extreme conditions of high stress, strain and strain rate. For example, strain rates developed during an asteroid impact on earth are likely to be in the order of  $10^8/s$ , resulting to a hyper velocity impact, i.e. impact velocities greater than 5km/s. For impact velocities associated with defense ballistics, high or peak strain rates developed are in the order of  $10^5/s$  to  $10^6/s$  [5]. Exposure to these extreme conditions results in structural damage, thus limiting material performance. As such, new innovative materials with enhanced ballistic protection and improved thermal-mechanical stability are required for future needs for ballistic protection technology. In addition, these materials need to be lightweight to allow maneuverability and have ability to absorb energy in a controlled manner for shock mitigations.

One approach with substantial potential to improve material structure and performance is polymer nanocomposites. Polymer nanocomposites (PNCs) combine two

concepts in material design, i.e. polymer matrix and a reinforcing nanoscale material referred to as nanofiller. A nanofiller is any material organic, inorganic or metallic with at least one dimension in the order of 1~100 nanometer. The nanofiller component gives rise to intrinsically new properties not present in pristine polymer [6]. Incorporation of nanofillers such as, graphite nanoplatelets [1, 7], exfoliated nanoclays [8-11] and carbon nanotubes[9] into polymer matrices have shown potential improvement in mechanical[9], thermal[12] and electrical properties[13]. This is attributed to fewer defects in filler particles at nanoscale, as compared to traditional filler particles at micro scale [4, 14, 15]. In addition, nanofillers have a high aspect ratio which is directly linked to effectiveness of nanofiller to enhance these properties; the higher the aspect ratio the higher the property reinforcement. Furthermore, nanofillers have the potential to be homogeneously distributed than traditional fillers, and in some cases allow for specific designed shape and functionality, influencing the material properties at molecular scales.

Nevertheless, one of the challenges with the nanofillers comes from their dispersion into the polymer matrix. A good dispersion of the filler within the polymer matrix is important. The extremely large surface area lead to strong tendency to form agglomerates and thus it is important to stabilize the dispersion to prevent aggregation of the filler[15]. However, various techniques have been used to overcome this challenge, for example, in the use of sonication or mechanical mixing during the fabrication of nanocomposite[4, 8, 11, 14, 16]. Hence, it becomes obvious that dispersion and stabilization are not simple issues and compromises have to be made depending on the applications[17].

Blumstein, first reported polymer nanocomposites, in 1961[8, 18, 19]. Blumstein demonstrated improved thermal stability by reinforcing poly (methyl methacrylate (PMMA) polymer with layered silicate [16, 18]. However, real commercial interest in PNCs did not occur until 1990s with Toyota's work on exfoliation of clay in nylon-6, to produce timing belt covers[15, 20]. The Toyota research group, observed exfoliation of layered silicates in nylon 6 greatly improved thermal, mechanical and barrier properties of the polymer[8, 10]. These property improvements made it possible to extend use of low-cost polymers in automotive applications. Interests continued to spur with extraordinary combination of properties of nanocomposites. Meredith et.al[4] demonstrated an increase of 58% in Young's modulus by adding a 4 vol.% mica-type silicate (MTS) to epoxy matrix[21]. Yano et.al

reported a 50% decrease in the permeability of polyimide at only 2% loading of MTS[22]. While use of silicate as nanofiller revolutionized nanocomposite research, discovery of fullerene by Smalley in 1985 followed by discovery of multi wall Carbon nanotubes in 1991, and more recently discovery of graphene by Geim and Novoselov in 2004 led to increased interest in nanocomposite research [15, 23-25].

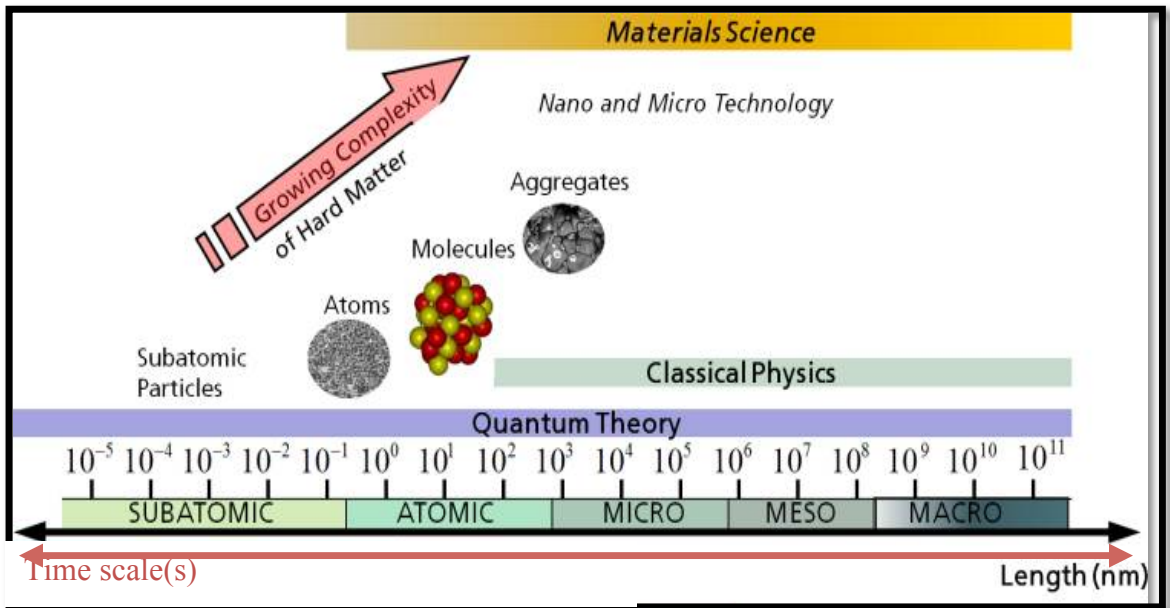


Figure 1: Schematic of the relationship between time and length scales for multi-scale simulation methodology[26]

One major benefit of polymer nanocomposites is the incorporation of multifunctional capabilities. For example nanocomposites for ballistic applications require a high thermal-mechanical stability to withstand extreme conditions of high temperature; they need to be lightweight to allow maneuverability; protect against high impact velocity; and mitigate the resulting shock wave. However, a nanocomposite with these desired properties is synthesized through large number of material systems, and painstaking experimental techniques. In addition, an experimental technique is costly and time intensive, due to specialized equipment required in ballistic and mechanical testing of materials.

Moreover, experimental techniques present difficulty in study of local interactions of constituent phases at nanoscale. For example, at nanoscale particle interactions is used to control assembly of nanometer-sized particles. Consequently, understanding behavior of

both materials at nanoscale is essential to elucidate material properties at macroscopic level. Such material behavior is governed by physical phenomena acting over several different lengths and time scales [3–24], as shown in Figure 9, which is critical for designing polymer/nanocomposite systems with multi-functionality, not only for enhanced impact resistance, but also in other applications where composite structures are increasingly needed.

Ballistic impact applications benefit from graphene polyurethane nanocomposite with a direct impact on weight savings, resulting from efficient multifunctional materials, performing more functions than being just structural members. In addition to savings in operational costs, weight reduction is of particular interest in unmanned air vehicles (UAV) and other defense applications where every pound of weight reduction has profound effects--resulting in improved flight time, maneuverability and survivability.

## 1.2. Objective

The goal of this work is to implement and use computational techniques to simulate processes at the atomistic level for investigating the structure-properties relationship, and dynamic response of hybrid material (polymer nanocomposite). Specifically this work will examine bulk properties of polymer matrix polyurethane, nanofiller (graphene) and polymer-graphene nanocomposite. In addition, since materials in many key applications today, such as in aerospace and defense applications are exposed to extreme environments; we will also address effects of exposure to extreme conditions including, high-pressure shock compression to thermodynamic and mechanical properties.

Understanding structure-property and dynamic response of these materials at atomistic level will establish guiding principles to predict bulk properties and help design new material beyond ballistic application. As a result of improved understanding emerging from computation-assisted design of materials, it will also become possible to design better structures using these materials. These opportunities, if exploited, can produce many protective materials of the future. Furthermore, molecular modeling and availability of higher performance computational resources provide a new paradigm for understanding condensed matter. This understanding will not only be achieved by incremental advances in materials science, but also by an interdisciplinary approach.



### 1.3. Dissertation Layout

Section 2 contains a literature description of components used for polymer nanocomposite, i.e. polyurethane, graphene, and graphene based nanocomposites. Particularly highlighting use of graphene nanofiller in enhancing thermal and mechanical properties of polymer matrices. This discussion aims, to provide a conceptual framework for development of polyurethane/graphene nanocomposite. Section 3 introduces an overview of basic fundamentals of computational models for material simulations. Computational simulations have evolved to bridge gap between traditional theory and experiments. This section highlights methods applied in this study, first atomistic simulation based on molecular mechanics (MM), molecular dynamics (MD), and secondly, quantum mechanics and density functional theory (DFT). By combining the right computational models with appropriate computational software, it is possible to understand material behavior without performing physical experiments.

Section 4 describes application of density functional theory (DFT) and Molecular mechanics (MM) in obtaining elastic constants of graphene using elasticity theory. In order to obtain accurate and comparable results to previously published work, we initially determined total energy convergence of graphene with respect to energy cutoff, and k-point sampling of Brillouin zone. We compared our results with previous theoretical and experimental work. Interestingly, our calculated results are very close to the theoretical and experimental data, leading us to conclude that our structure is plausible. Additionally, we calculated the elastic constant of monolayer graphene with MM using different potential functions, i.e. reactive force field (ReaxFF), Tersoff and New\_Tersoff. The general anisotropic, non-linear mechanical behavior of graphene is evident in both approaches. However, the accuracy of the mechanical properties predicted by MM approach is limited by empirical potentials. Both the Tersoff and New\_Tersoff potential predict an elastic modulus comparable with DFT calculations. While ReaxFF potential underestimates elastic constants of graphene significantly, this is a major shortcoming of potential functions in modeling the mechanical behavior of graphene.

Section 5 described studies on thermal-mechanical properties of polyurethane and its graphene nanocomposite. First, amorphous polyurethane models were successfully generated

using Dreiding potential function, with exponential six forms of van der Waals interactions. Electrostatic interactions were evaluated using Ewald Summation where atomic charges are determined from charge equilibration method. We calculated properties relating to intermolecular interactions, including density, glass transition temperature and mechanical properties. To obtain mechanical properties we utilized both molecular mechanics and molecular dynamics using uniaxial deformation. The stiffness matrix results show basic feature of an isotropic material. We have calculated moduli and Poisson's ratio for all polyurethane models; these properties are essential in characterizing the mechanical properties of a system. Calculation of equilibrium density and mechanical tests gives us confidence over the simulations, since they predict the properties with the same order of magnitude as experimental, this step is important because later investigation of polymer nanocomposite will have significant credibility. Secondly, we successfully generated the graphene-polyurethane nanocomposite models, varying the weight percent of 13.65wt % and 17.28 wt%. Additionally, we also looked at the effects of graphene flakes on the thermo-mechanical properties. The elastic and thermodynamics properties on the effect of graphene sheets and graphene flakes on amorphous polyurethane were investigated with molecular dynamics simulation. Young's modulus of 95.98 Gpa was estimated for polyurethane reinforced with graphene sheet compared to 3.76 Gpa for polyurethane reinforced with graphene flakes. Elastic properties obtained for were significantly higher for the polyurethane/graphene sheet nanocomposite compared with the graphene flakes. This behavior is attributed to the lack of surface effects in the infinite sheets, while the surface effects contributed to the increase in thermal expansion coefficient.

Section 6 concludes the last part of this dissertation. We investigated the dynamic response of polyurethane and its graphene nanocomposite using non-reactive molecular dynamics. Using the projectile/wall approach, planar shock waves with particle velocity ranging from 0.1 to 2.5 km/s were propagating along the z-direction of the polymer. Additionally, graphene was added into the polymer matrix, perpendicular to the z-direction. Furthermore, we have used non-equilibrium molecular dynamics (NEMD) simulations to investigate the dynamic response behavior of polyurethane and its graphene nanocomposite. Calculation of the Hugoniot states of polyurethane agrees with the experimental studies. However the phase change phenomena observed in experimental work was not visible in the

present work. This is likely due to the bond breaking and formation, which is a clear characterization of the phase changes. The graphene-polyurethane nanocomposites demonstrate similar shock wave propagation illustrating characteristics of impeding the shock wave when subjected to difference particle velocities. This is likely due to graphene inducing stress concentrations in the composite and may increase the yield strength. Moreover, our simulations suggest that the bulk shock response of the composites depends on the position of the graphene, with a slight difference being observed between the shock response in the Zlow position (initial direct contact with the projectile) or Zhi, (initial direct contact with the polymer).

This work highlights the promise of atomically thin, periodic nanostructures like graphene for shock wave mitigation in various applications such as in aerospace, transportation and military. Our approach strongly suggests that a bottom-up, systematic redesign of composite materials can yield significant improvements over existing technological methods. We expect that this work will add to the understanding of next generation nanocomposites for materials for ballistic technology. Furthermore, this work contributed to the broad knowledge of graphene nanocomposites and confirms even at the atomistic level, that the aggregated graphene flakes need to be exfoliated in the form of graphene sheets and uniformly dispersed into a matrix system

## 2. LITERATURE REVIEW

When dealing with different materials in a composite, it is essential to have knowledge of properties of individual components in order to estimate properties of the entire system. Thus this section provides a literature review on the components used in this study, i.e polyurethane (polymer matrix) and graphene (nanofiller). Furthermore, the second part of this section highlights use of graphene nanofiller in enhancing thermal and mechanical properties of polymer matrices. The discussion aims to provide a conceptual framework for development of polyurethane/graphene nanocomposite for potential use in ballistic applications in both civilian and defense applications.

### 2.1. Polyurethane

Polyurethanes (PURs) are a versatile class of polymers formed by reacting long a diol or polyol (OH–R–OH) and a diisocyanate (OCN–R'–NCO) (Figure 1). Generally, R is a linear hydrocarbon chain and R' is an aromatic or aliphatic moiety. PURs are considered copolymers with alternating macrodiol soft segment (SS) and urethane hard segments (HS) of crystalline and amorphous regions. The soft and hard segments are incompatible in terms of polarity and chemical nature, driving the phase separation into nanoscale domains that control PUR properties [27, 28]. The extent at which phase separation occurs is dependent on; the size of both hard and soft segments; type of diisocyanate and polyol and molecular weight of the hydrogen bond formation between urethane linkages.

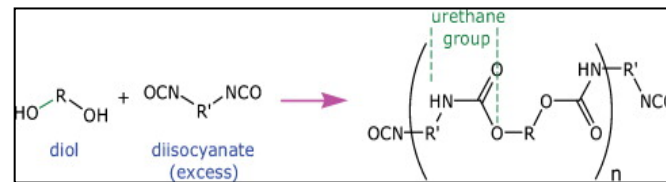


Figure 2: Schematic of basic reaction scheme of urethane formation

The urethane group, Figure 2, acts as a linker between the hard and soft segments of the polyurethane. The linkage is achieved by covalent and hydrogen bonding. Hydrogen bonds are either parallel or anti parallel [27, 28] forming an infinite stack of hydrogen

bonded arrays. Furthermore, hydrogen bonding has a significant effect reaction kinetics that drives formation of urethane group. The strength of the hydrogen bond is enhanced by thermal annealing, thus increasing the PURs melting points resulting to greater uniformity of the polymer network.

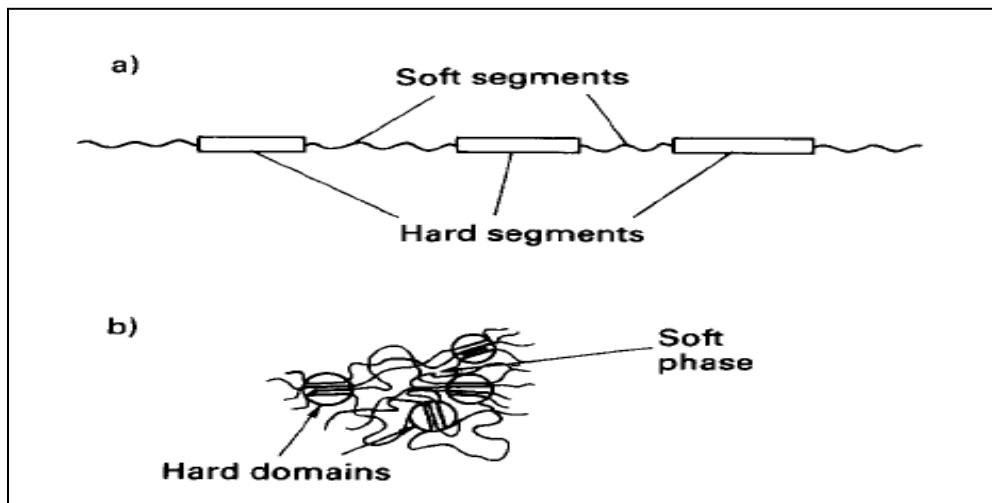


Figure 3: Structure of segmented polyurethane (a), two-phase structure of the bulk polymer (b)[29].

Since the first development of PURs by Otto Bayer and coworkers in 1937 [1], PURs have been exploited for wide range of applications, from structural[29, 30], industrial[31] to medical applications [32]. In addition, PURs are efficiently tailored to a diverse range of products such as foams, coatings, adhesives, fibers, rubbers or thermoplastic elastomers[27]. Moreover, the properties of PURs are tailored by varying the chemical nature and composition of polyol, diisocyanate, and chain extender or by dispersing fillers in a polymer matrix (6-11). Furthermore, the alternating soft and hard segments self-assemble into two phases. Such phase separation contributes to the excellent mechanical properties of PUR [33]. However, low stiffness, tensile strength and thermal stability can limit PURs in its applications. To overcome these limitations PURs can be enhanced by reinforcing the polymer matrix with rigid, strong nanometer size range material to produce what is commonly referred to as a polymer nanocomposite.

The wide range of use for PURs lies in its advantages of high hardness for a given modulus, high abrasion and chemical resistance, excellent mechanical and elastic properties [27, 28, 34]. Furthermore, PURs synthesis is tailored by varying type and ratio of the diol and diisocyanates, by changing formulation to give properties ranging from soft elastomers to relatively hard reinforced rubbers[35]. Also, physical crosslinks provided by HS micro domains in PURs can be melted, allowing materials to be molded or extruded for most commercial applications.

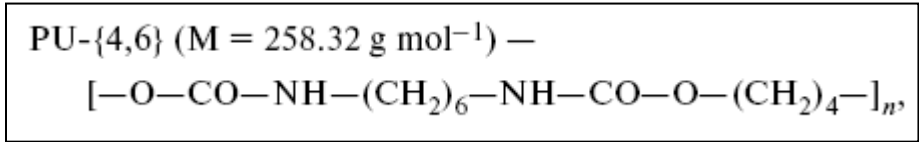


Figure 4: Molecular structure of monomer of linear polyurethane ([C12H24N2O4]).

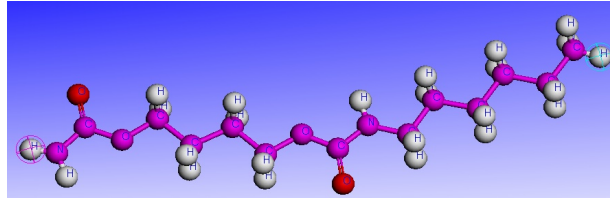


Figure 5: Monomer of polyurethane matrix model from material studio.

More recently PUR has gained interest in the research community to study the blast and shock mitigations effects of polyurethane [36, 37]. For example polyurethane coatings, have recently been used to laminate material used to for high impact resistance [38, 39]. PUR coating help to minimize fragmentation from injury-causing blast-pressure propelled debris [3, 33]. PUR coatings are also applied to military armor to increase resistance to ballistic penetration [3, 33, 38, 40, 41]. PURs have good properties that can dissipate and divert shock pressure in a controlled manner[36]. The dissipative nature of polyurethane could arise from its morphology of repeating units of hard and soft segments. Interestingly, such a chain structure allows for the phase separation of hard domains to remain covalently linked to each other via the soft segments. How the chain architecture of polyurethane, or any polymer, might enhance its shock mitigation or energy dissipation properties necessitates a more detailed examination to clear understanding the mechanisms responsible for the superior energy dissipation properties in polyurethane.

Thus as a first step in this work, we explore thermal--mechanical properties of the pristine polyurethane presented in section 4 of this dissertation. Determination of ultimate thermo-mechanical properties of matrix material is critical for development of better polymer nanocomposites. In the present work, we will consider a linear polyurethane with molecular structure of 1, 4 butane diol (BDO) and 1, 6 hexylmethylene dissociate (HDI). The molecular structure of the monomer is  $([C_{12}H_{24}N_2O_4])_n$ , where  $n$  is the repeat units of the monomer (Figure 3). Since our polymer is amorphous in nature, the backbone of the polymer structure is linear, with no crystallinity, making their strength temperature dependent.

## 2.2. Graphene

The second component, nanofiller is graphene. Graphene is an allotrope of carbon. Carbon is one of six most abundant chemical elements in the universe discovered by A.L Lavoisier in 1789[42, 43]. It is a unique element not only in material science, but also in practical applications, with its greatest use in iron and steel industries in form of coke to reduce iron ore in blast furnaces.

Carbon uniqueness lays in its ability to bond in different ways forming different carbon allotropes, with completely different properties, for example, diamond and graphite. These different allotropes are due to the flexibility of carbon's valence electrons, are shared equally, i.e.  $sp^3$  hybridized, to form an isotropic of diamond crystal. Furthermore, when three valence electrons are covalently bonded between neighbors in a plane, i.e  $sp^2$  hybridized, the fourth is delocalized amongst all atoms. Resulting material from this type of bonding is layered structure known as graphite. Graphite has strong in-plane bonds, but weak out of plane bonding of the van der Waals type. The weak van der Waal bonding allows them to slide relatively easily across each other resulting to the softness in graphite pencils.

The notion that carbon could exist in other forms other than graphite and diamond, generated interest amongst global research community, which led to discovery of new forms of carbon within the last thirty years [43-46]. These forms of carbon include fullerene (1985), carbon nanotubes (1991) and graphene (2004). Fullerene ( $C_{60}$ ) was discovered in 1985 by a team headed by Smalley et al.[45], and led to Nobel Prize in Chemistry in 1997.  $C_{60}$  resembles a soccer ball like molecule made of pure carbon atoms bonded in hexagonal and

pentagonal crystal configurations. Fullerene is  $sp^2$  hybridized carbon form, which is stable but not totally un-reactive.

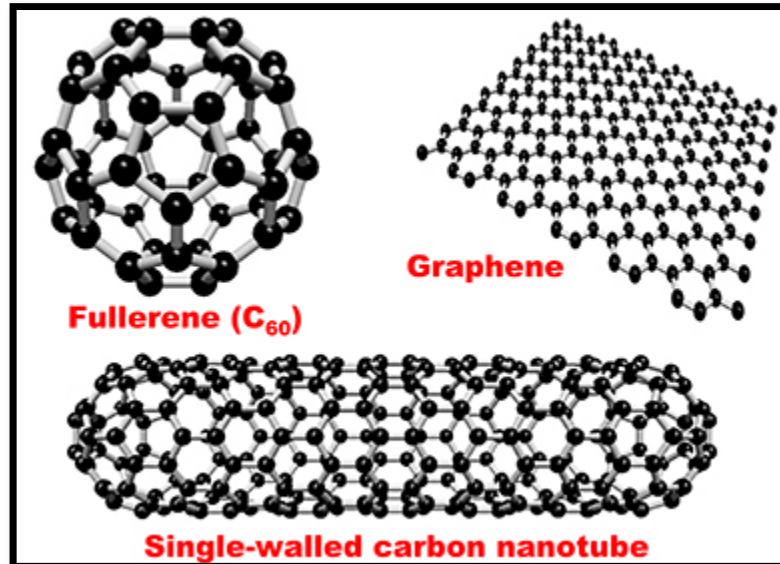


Figure 6: Some allotropes of carbon, fullerene, graphene and single walled carbon nanotube[42].

Carbon nanotubes (CNTs), were first reported in 1991, by Iijima. His first discovery was in the form of multi-wall carbon nanotubes (MWNTs) from carbon soot by arc-discharge method [44]. A couple of years later, he observed single wall nanotubes (SWNTs)[46]. Both of MWNTs and SWNTs are typically a few nanometers in diameter and several micrometers to centimeters long. The bonding in carbon nanotubes is  $sp^2$ , with each atom joined to three neighbors, as in graphite. CNTs have assumed an important role in the context of nanomaterials, because of their novel chemical and physical properties[43]. They are mechanically very strong, with a Young's modulus is over 1 Tpa, making CNTs as stiff as diamond, (Table 1), and can conduct electricity extremely well[47, 48]. All of these remarkable properties give CNTs a range of potential applications: for example, in reinforced composites, sensors, nanoelectronics and display devices[43].

Graphene is a two dimensional material. It is said to be the starting point of all calculations on 3-D graphite, 1-D carbon nanotubes and 0-D fullerenes [49]. Graphene was first explored in 1947 as a starting point for understanding electronic properties of more complex graphite [50, 51]. However, it was presumed thermodynamically unstable and could



not exist in a free state. For this reason 2D materials were presumed not to exist independently and were known only to be an integral part of 3D crystals. This notion was put to rest in 2004, when Andres Geim and Konstantin Novoselov managed to isolate a single atomic layer of graphene sheets, by mechanical exfoliation of graphite using scotch tape [52]. Consequently, this ground breaking experiment led to Geim and Novoselov winning the 2010 Nobel Prize in Physics. To date, graphene has captured the attention of many researchers worldwide. Hence, a significant amount of research has been explored to reveal electrical[24], optical absorption[53] mechanical properties[54] and thermal[55],of graphene and to explore what might be the key applications of this novel material.

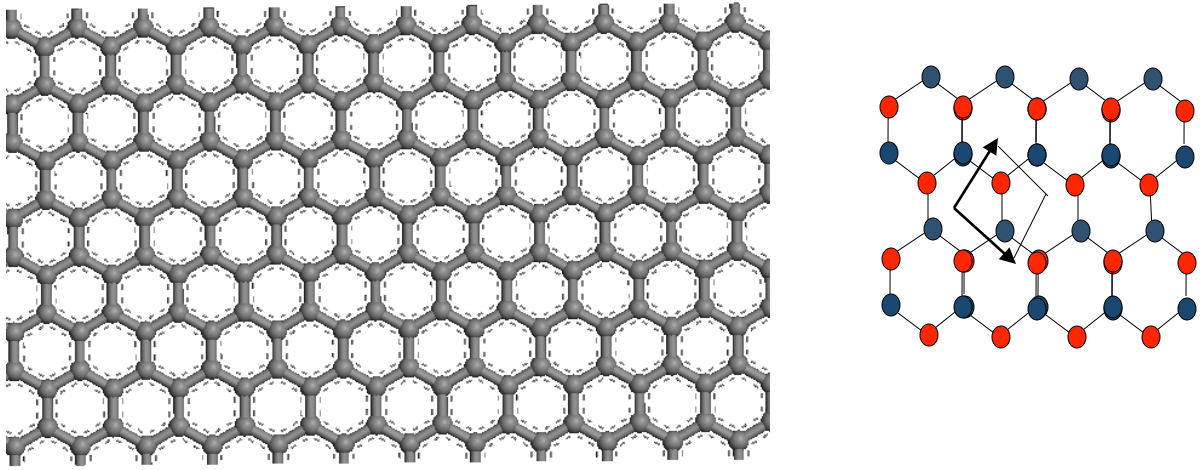


Figure 7: Schematic of (a) honeycomb crystal lattice of graphene (b) graphene lattice with two atoms representation of unit cell.

Graphene is composed of  $sp^2$  carbon atoms arranged in a honeycomb crystal lattice as shown in Figure 5(a). The lattice vectors of graphene are expressed as follows:

$$a_1 = \frac{a}{2}(3, \sqrt{3}), \quad a_2 = \frac{a}{2}(3, -\sqrt{3}) \quad (2.1)$$

Where  $a$  is the carbon-carbon inter-atomic length of  $1.42\text{\AA}$ , and  $a_1 = a_2$  represent the lattice constant, which has a value of  $2.46\text{\AA}$ . The rotation angle of  $120^\circ$  around carbon-carbon atom, and inter-atomic length is much shorter than in cubic diamond of  $1.54\text{\AA}$ . Lattice consists of two interpenetrated triangular sub-lattice. Atoms of one sub-lattice are at the center of the triangle, which is defined by the other sub-lattice as shown in Figure 5(b). Graphene structure

is classified as zigzag and armchair type. These structures differ according to their orientations and directions along the edges. Looking at Figure 5(a) and considering the edge along y-axis we see an armchair structure, while the edge along the x-axis indicates a zigzag structure.

Table 1: Physical properties of carbon based materials. The mass density of graphene represents the two-dimensional graphene layers in  $\text{g}/\text{cm}^2$

Physical properties	Diamond	CNTs	Graphite	Graphene	Reference
Density ( $\text{g}/\text{cm}^3$ )	3.52	1.3-1.4	2.26	$0.76 \times 10^{-7}$	[42, 47, 55]
Tensile strength (Gpa)	>1.2	11-63	0.0048	130	[56, 57]
Bulk Modulus (Gpa)	442	462-546	444	340	[58]
Young's modulus (Gpa)	1050	1000	1060	500-1000	[55],[59]
Poisson's ratio	0.2	0.06 to - 0.20	0.16	0.146	[55],[59]

Graphene, like graphite, consists of  $sp^2$  hybridizations of one  $s$  orbital and two in-plane  $p$  orbital, which contribute to mechanical stability of graphene sheet. The  $sp^2$  hybridizations makes the structure trigonal planar which causes a sigma ( $\sigma$ ) bond between the two carbon atoms. The  $\sigma$  bonds occur in all allotropes of carbon and are responsible for the robustness of the lattice structure. The remaining  $2p$  orbital is perpendicular to molecular framework and overlap in a side-by-side manner to give pi ( $\pi$ ) bond, which contains valence electrons or  $\pi$  electrons. The pi bond and valence electrons are responsible for conduction and valence bands, which dominate the planar conduction phenomena in graphene [60]. This  $\pi$  bond is responsible for band structure of graphene being semi-metallic with unusual dispersion of Dirac Fermions [42, 48, 60]. The  $\pi$  bond shows graphene layer has clouds of electrons above and below which is responsible for its semi-metallic nature.

All carbon-based nanostructures mentioned above have excellent mechanical properties because of the  $sp^2$  carbon hybridization. For example, Young modulus of CNTs was theoretically estimated to approximately 1TPa[61, 62], and experimental estimated in

the range  $\sim 0.3\text{-}1.5\text{Tpa}$ [59, 63, 64]. Using atomistic simulations, fracture strains of CNTs were calculated to approximate values of 10-16% at a failure stress in the range of  $\sim 63\text{-}95\text{Gpa}$ [65]. Young modulus of a mono-layer graphene sheet is theoretically estimated to approximately  $1.02\text{Tpa}$  with a reported Poisson's ratio of 0.149[66] and validated experimentally with a fracture strength of  $42\text{N/m}$  [67]. Also, Faccio et al. used using ab initio approach to calculate the Young modulus and Poisson's ratio of graphene nanoribbons (GNRs) of  $\sim 3.2\text{-}5\text{TPa}$  and  $\sim 0.15\text{-}0.26$  respectively[68]. A comparison for some physical properties of carbon-based nanostructures is summarized in Table 1.

Since its discovery, graphene has emerged as an interesting material because of its remarkable set of diverse properties in mono-layer, few-layer and graphene-oxide. Theoretical and experimental results have revealed that graphene is the strongest material developed to date, [67, 69, 70]. The exceptional mechanical properties with a reported value of Young modulus as  $1.0\text{ Tpa}$  [67] opens up opportunities for graphene as a nano-mechanical material. In addition, the explosive growth of the new field of thermal properties of graphene is driven by the unique thermal conductivity of graphene. Thermal conductivity of graphene is  $5000\text{ Wm}^{-1}\text{K}^{-1}$ , mobility of charge carriers of  $200000\text{-cm}^2\text{ V}^{-1}\text{ s}^{-1}$ , a calculated value of  $2620\text{m}^2\text{g}^{-1}$  for specific surface area and captivating transport phenomena such as the quantum Hall effect [54, 71]. These properties match the limitation of other materials, such as CNTs, graphite, hetero-structure 2D electron gas that have been studied and used as nanofillers. Compared to CNTs, graphene continues to receive considerable attention due to their aforementioned properties, in addition to their low aspect ratio and density. Therefore nanocomposites utilizing graphene as nanofillers offer the opportunity to impart superior mechanical and thermal properties essential in structural applications.

These extraordinary properties of graphene have generated a great deal of research interest for its possible use in numerous applications (Figure 6). Such as in high frequency transistors[72], ultra-thin carbon films[73, 74], gas sensors[75], hydrogen storage[76] biodevices for drug delivery imaging[53, 77], nano-mechanical actuators[78, 79], and nanocomposites[74, 75, 80]. Of interest in this work is the use of graphene as nanofiller in polymer nanocomposites. Graphene nanofillers have been dispersed successively on polymer matrices [81-84]. Polymer/graphene nanocomposites (PGNs) show significant enhancement in electrical mechanical, gas barrier, and thermal stability of polymer matrix with an addition

of low volume fraction of graphene [24, 39, 67, 85, 86]. However more research on the high-performance PGNs is needed to facilitate a fundamental understanding of the design of new materials and devices using PGNs [74, 80]. The next section discusses the effectiveness of graphene as nanofiller on the thermal and mechanical properties on various polymers.

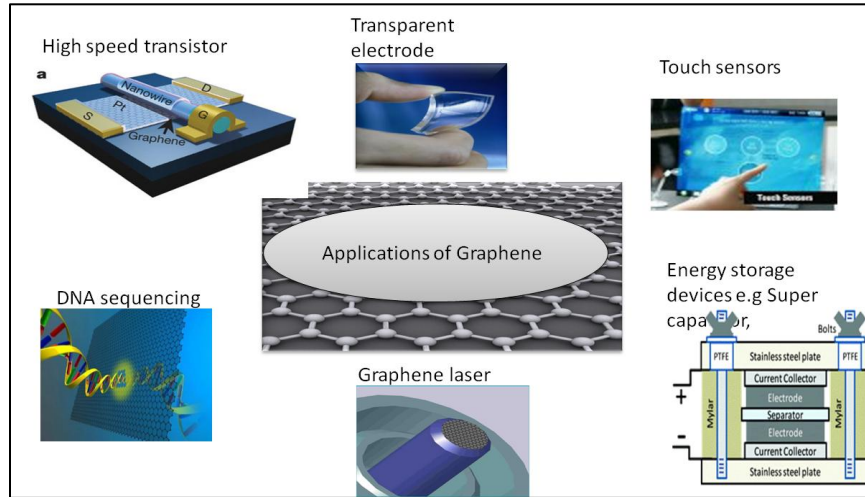


Figure 8: Potential application of graphene.

### 2.3. Overview of Graphene for Composite Filler

The discovery of graphene by Geim and Novosoleve opened a new dimension in the field of nanocomposites. Graphene nanofillers have been dispersed successively on polymer matrices using various approaches [81-84]. For example researchers recently dispersed graphene fillers into polymers by using a melt blending technique. A technique whereby graphene fillers and a melted polymer are mixed together using a shear mixing approach, and mixture fed into an extruder machine to develop the nanocomposite [87-90]. Additionally, emulsion polymerization method, is utilized to produce an aqueous colloidal suspension of graphene oxide sheets for applications in latex-based polymers [91, 92]. Since scope of this work is investigating the effect of graphene on thermal mechanical properties, this section discusses effectiveness of graphene as nanofiller on thermal and mechanical properties on various polymers.

Thermal behavior of polymer matrix is significantly enhanced in PGNs. This has been demonstrated on a wide range of polymers matrices, for example, in polyethylene

(PE)[84], polypropylene(PP)[93], polyamide(PA)[84], and epoxy[94-96] polymer matrices. In epoxy/graphene nanocomposites, a significant increase in thermal conductivity was observed by incorporations 25 vol %[94] or 33vol %[95] of graphene nanofiller. Conversely, with a same amount of graphene in PP, PE, and PA, thermal conductivity of this nanocomposites did not show a significant increase[84]. In the epoxy/graphene study, Haddon and co-workers[94] observed an increase of more than 3000% in thermal conductivity of epoxy polymer with similar loading of 25vol%. This remarkable value was achieved by applying different thermal temperatures to control the aspect ratio of graphene. These results have been attributed to the strong interfacial interactions between polymer chains and graphene surface. Moreover, vigorous perturbations of local and global polymer chain dynamics lead to changes related to physical aging and the glass transition temperature ( $T_g$ )[97].

Glass transition temperature ( $T_g$ ) is one of the most important properties in engineering applications of polymers. It is largely influenced by incorporation of nanofillers in polymer matrix. The nanofiller leads to a high surface area of polymer/nanofiller interfaces even at low loading, thus far, only a few studies report  $T_g$  values of polymer/graphene nanocomposites. For example, Ramanathan et al. [85] observed a 30°C increase in  $T_g$  in PMMA with only 0.05wt% functionalized graphene sheet(FGS), and 46°C in poly(acrylonitrile) loaded with 1% wt FGS. Furthermore, Salagione et al[98] reported a significant increase in  $T_g$  of 25°C with a 1.4wt% loading of a nanocomposite of reduced graphene oxide in polyvinyl chloride (PVC). The increase in  $T_g$  from these studies may be attributed to an enhanced mechanical interlocking of the polymer chains and the FGS thereby resulting to a better interfacial adhesion. These improved, thermal and glass transition properties show enhanced thermal stability in PGNs compared to pristine polymer. Hence, polymer/graphene nanocomposites are promising as a thermal interface material for heat dissipation. In addition, understanding the behavior of  $T_g$  is vital for high temperature applications and for polymer processing.

The key aspects in mechanical properties of polymer/graphene nanocomposites depend on how graphene layers are dispersed in polymer matrix, and nature of polymer/graphene interfacial bonding. For example, recent experimental investigations of graphene filled polymers have indicated an increase in modulus as a function of graphene

loading fraction [24, 99-103]. Improved values in modulus vary from 31% for 0.05wt% thermally exfoliated graphene/epoxy[100], 62% achieved by 0.7wt.% chemically reduced graphene/poly(vinyl alcohol)[101], 128% for 3wt% chemically reduced graphene/poly(vinyl alcohol)[99], to 200% increase for 5wt% thermally exfoliated graphene/polyurethane[104]. While these studies show an increase in modulus in PGNs, larger improvements are observed in elastomers. This has been attributed to the low intrinsic modulus in elastomers, and the great stiffness contrast between graphene nanofiller and polymer matrix. Even though most of the studies have reported increase in modulus in PGNs, few studies have reported increases of up to 75% in tensile strength with 0.7 wt.% unreduced graphite oxide in poly (vinyl alcohol).

Table 2: Mechanical, thermal and electrical properties of graphene, CNT, and polymeric materials

<b>Materials</b>	<b>Young Modulus (GPA)</b>	<b>Thermal Conductivity (W/mk)</b>	<b>Electrical Conductivity (S/m)</b>	<b>Ref</b>
<b>Graphene</b>	1060	4800-5000	7200	[54, 55, 67, 105]
<b>CNT</b>	60-50	3500	3000-4000	[17, 58, 105]
<b>Nano -size steel</b>	1.769	5-6	$1.36 \times 10^6$	[106]
<b>Kevlar</b>	3.62	0.04	insulator	[2, 107]
<b>Polyurethane</b>	1.69	0.24	insulator	[27, 108]
<b>Polyethylene (HDPE)</b>	0.018-0.020	0.46-0.52	insulator	[108, 109]

Ultimately, strong effect of graphene nanofiller on properties of polymer matrix, may allow properties of polymer/graphene nanocomposites to be tailored at atomic level for a specific application. However, the phenomenon of interfacial interactions between polymer matrix and nanofiller, and effect of dispersion of nanofiller on polymer properties is yet to be fully understood. This phenomenon, if fully understood, would make it possible to design novel nanostructure materials for use in a wide range of mechanical, electrical, chemical, optical and biological applications. The feasibility of these applications will depend to a

certain extent upon thermal-mechanical properties of the polymer/graphene nanocomposite that determine their processibility and mechanical integrity.

The incorporation of graphene layer into polyurethanes can produce a new type of material by combining special mechanical properties of graphene with structural properties of polyurethane. In order to fully utilize this type of multifunctional nanocomposite that is light weight, enhanced thermal and mechanical properties are important in design and development of novel structures for use in both civilian and defense applications. Our research indicates graphene fillers show great potential for development of next-generation composite materials for use not only in ballistic application, but also in other structural applications.

### 3. COMPUTATIONAL METHODS FOR MATERIAL SIMULATIONS

The current trend in nanotechnology requires scientist and engineers to develop hierarchical material structures with key characteristics in the 0.1-300nm lengths scale, to benefit from the unique mechanical, electrical, magnetic or optical properties that emerge at this scale. At nanoscale, devices have significantly enhanced performance; reliability and sensitivity with significant decrease in size, weight and cost. However, nanoscale region is characterized by small units too small to visualize and manipulate, making it a challenge from an experiment perspective. Thus it becomes essential to utilize computational and theoretical approaches to develop accurate structures to understand how the properties of materials change in response to various conditions of temperature, pressure, stress or strain, and concentration as a function of time.

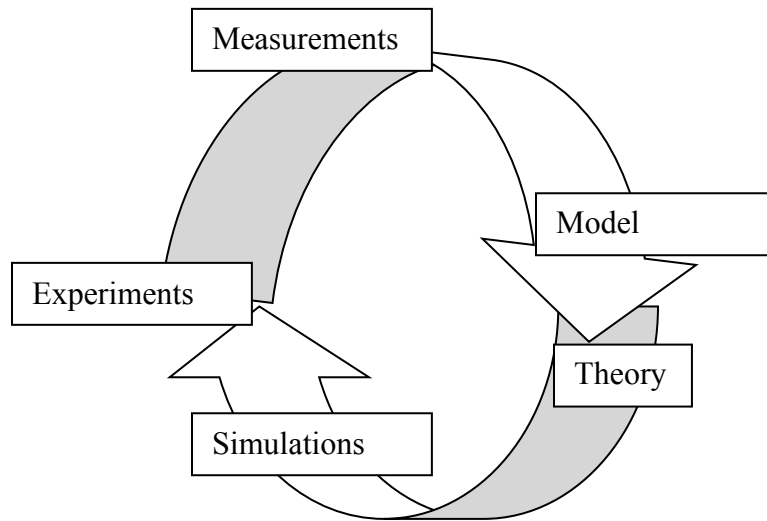


Figure 9: Illustration of the interdependence of methods and the nature of experiment, theory and simulations.

The importance of modeling is depicted in Figure 8. Observations via experiments techniques were the earliest method used to understand material behavior. Data obtain in experiments are carefully observed via measurements and then used for development of models. Models are essential to develop theory. Consequently, theory is used for comparison between simulations and experimental techniques. This comparison is necessary to validate theory. In addition, theory is used to predict properties of new materials in advance of



experiments. Thus, development of a realistic theory of describing structure properties relationship of material behaviors is dependent on accurate simulation and modeling techniques

In many problems in all fields of science, material behavior is governed by physical phenomena, which act over several different lengths, and time scales as shown in Figure 1. The essential microscopic constituents of materials are atoms[6]. Interactions of atoms at micro-scale level govern material behavior at macro-scale level. Micro-scale level includes order of nanometers and femto-seconds, and macro-scale level is on the order of centimeters, milliseconds, and beyond. In many technology applications, macro-scale level is of industrial interest. Consequently, material behavior at this level is studied using laboratory techniques and test methods. However, these methods face many challenges due to complicated breadth in length and time scale in material phenomena. Thus, availability of theory and computational tools for predicting materials behavior, and understanding underlying chemistry and physics at different length and time scale is complimentary to laboratory techniques. Hence, performing material simulations across different lengths and time scales has an obvious interest as a tool of potentially great effect on technology innovation. In particular, understanding the integrity of operations at the micro-scale level under high impact velocity is critical to the design of innovative materials for both civilian and defense applications.

In computational approaches, a model is developed to mimic a real system. In many practical research problems basic question arises from, figuring out which model to use for answering a specific question. The model is then used to study mechanisms in addition to physics and chemistry's of molecular interactions of system. Computational approach has several advantages, first, development of a robust molecular model minimizes labor, cost, and time required to prepare real material samples. Second, ability to simulate chemistry and physical phenomena at atomic and sub-atomic level provides knowledge on the atomistic and molecular behaviors, which is hardly obtained from classical experimental methods. Third, allows one to understand the material phenomena more meticulously. However, one disadvantage of molecular simulations is results are never totally reliable, and results are normally validated with experimental data.

The current trend in nanotechnology requires scientist and engineers to develop hierarchical material structures with key characteristics in the 0.1-300nm lengths scale, to benefit from the unique mechanical, electrical, magnetic or optical properties that emerge at this scale. While laboratory methods may present the phenomena, computational techniques are complimentary in explaining mechanism behind the phenomena. For example, at micro-scale macromolecules are stabilized by physical interactions arising from covalent, ionic, hydrogen or Van der Waals interactions. Inorganic crystalline materials create atomic level imperfections such as point, line or surface defects. Such defects play a major role in influencing the properties of engineered materials. For example, strength of metallic material is controlled by number and type of imperfections, hence, one needs to understand material behavior from a hierarchical perspective[110].

Ideally, all problems in molecular-level would be tackled by using quantum mechanics to calculate the wave function and the energy of the system [11]. Quantum mechanics is the mathematical theory that describes the dynamic nature of matter at the microscopic scale. It is based on a number of postulates, such as dual particle and wave like behavior, and interactions of energy and matter. These postulates are based on a wide range of experimental observations, and widely described in many quantum mechanics textbooks. Quantum mechanics methods solve Schrödinger equation directly to obtain the energy of the molecule or periodic system with no recourse to inter-atomic potentials; but they are *much* more computationally expensive[111, 112], due to limitations of computer time and memory [113]. This presents a problem for material such as polymers with large number of molecule or atoms. As an alternative, potential based method that are computationally cheaper are used in systems with large number of molecules or atoms, such as glass or amorphous polymers, where large simulation cells are required to represent long range order [114].

In this work we have utilized quantum-based calculation to perform first principle calculations on graphene (nanofiller), using density functional theory (DFT). These calculations enable us to develop a model for designing the nanocomposite system. In addition, we have employed use of empirical or semi-empirical methods to study the thermal-mechanical properties of the polyurethane and its graphene nanocomposite. Additionally, since most ballistic applications are exposed to the shock effects, we will look at the dynamic response of these materials under shock-wave loading. Since the properties of materials or

their interactions are described by the inter-atomic potentials, we briefly outline the theoretical background of both methods as it pertains to this work in the following section.

### 3.1. Quantum Mechanics and Density Functional Theory

Quantum mechanics (QM), theory is commonly used as a basis of modern physics. It was developed as a result of limitations of classical theories of mechanism and electromagnetism, to provide satisfying explanations on properties of electromagnetic radiation and of atomic structure[115]. In classical theories, particles in motion have a well-defined position and momenta and follow defined trajectories. Conversely, on atomic and sub-atomic scales position and momenta are not precisely determined; however they are estimated to a certain degree of precision as stated by Weiner Heisenberg in 1927: the uncertainty principle:

$$\Delta x \Delta p \geq \frac{\hbar}{2} \quad (3.1)$$

where  $\hbar$  is the reduce planks constant;  $x$  and  $p$  are position and momentum of the microscopic particle.

As demonstrated by De Brogil's work, quantum state of electrons and nuclei has wave like properties. These properties are described by wave function as a function of coordinates and time  $\psi(x,t)$ . However, since uncertainty principle shows that detailed trajectories of electrons cannot be defined, wave function is described in terms of the probability of electrons having certain positions and momenta. These ideas are combined in the Schrödinger equation. The Schrödinger equation is the fundamental equation of quantum mechanics. It describes any changes in a physical system from a quantum state at each time, by a state vector. [116]. Electronic properties and energy of atomic systems are solved by time independent Schrödinger equation, which in its general form

$$\hat{H}\psi(x) = E\psi(x) \quad (3.2)$$

where  $\hat{H}$  is the Hamiltonian operator acting on the wave function  $\psi$ , and the proportionality constant,  $E$ , is the energy of the state  $\psi$ .

The Schrödinger equation, and its solutions, introduced a breakthrough in thinking about physics. For example, basic simulation methods, such as *ab initio methods*, were developed to solve the Schrödinger equation approximately. However, the overall form is not unusual or unexpected. For non-relativistic Schrödinger equation, Hamiltonian of a system is interpreted as

$$\hat{H} = \text{Kinetic energy (KE)} + \text{Potential Energy (V)} \quad (3.3)$$

Since nuclei are much heavier, and their motions are much larger in time-scale, compared to electrons, their dynamic can be described by classical Newtonian physics, instead of Schrödinger equation, and electronic configuration is assumed to be at ground state. Therefore the Born Oppenheimer approximation simplifies this equation by decoupling the electronic and nuclear dynamics and the Hamiltonian can be broken down to the form

$$\hat{H} = \sum_I^{nuclei} \frac{p_I^2}{2M_I} + \sum_i^{electrons} \frac{p_i^2}{2m_i} + \sum_{i,j}^{electrons} \frac{e}{r_{ij}} + \sum_{I,J}^{nuclei} \frac{Z_I Z_J}{R_{IJ}} - \sum_I^{nuclei} \sum_j^{electrons} \frac{Z_I}{R_{Ij}} \quad (3.4)$$

$$= T_N + T_e + V_{ee} + V_{NN} + V_{Ne} \quad (3.5)$$

where, first two terms represent kinetic energies of nuclei and electrons, respectively. The latter are contributions from electron-electron, nuclear-nuclear and nuclear electron interactions. Still, the exact solutions of quantum mechanics equation cannot be obtained for system with more than one electron. In practice, there are different theories proposed to approximate the energy and properties of multiple electrons systems. Each approach in turn is accurate and valid for only a selective set of problems and materials and requires sophisticated manipulations.

Recently, Density Functional Theory (DFT) has become one of the most important and reliable methods for predicting ground-state properties at electronic level[117, 118]. This is due to high accuracy and computational efficiency. DFT started to become popular in the 1970's[119] and in 1998, Walter Kohn, one of its creators was honored by receiving the Nobel Prize in chemistry. DFT describes electrons of interacting system onto a non-interacting electronic system moving in an effective potential as represented by Kohn-Sham

equations[119]. This is done in order to accurately calculate the contributions to the ground state energy. Other information obtained for a particular system using DFT includes the dynamical, electronic, and structural properties. Therefore, in DFT, the electron density is given as a scalar function by:

$$\rho(r) = \sum_i n_i |\psi(r)|^2 \quad (3.6)$$

where  $n_i$ , represents the occupations number of the eigenstate  $i$ , while  $r$  is any point in real space. The electron density  $\rho(r)$  is varied by changing the wave function  $\psi(r)$  of the system, if electron density  $\rho(r)$  corresponds to the given wave functions, then its total energy is equal to the minimized energy, and the whole system is in a ground state.

The total energy of the system depends on the position of the atoms. It is divided into three terms; kinetic energy term, the columbic energy term and the exchange-correlation terms written as follows

$$E(\rho) = T[\rho] + V_{ee}[\rho] + V_{Ne}[\rho] + E^{xc}[\rho] \quad (3.7)$$

in which  $T[\rho]$  is the ground state kinetic energy term, given by the sum of all contributing electrons in the system.  $V_{ee}[\rho]$  and  $V_{Ne}[\rho]$ , are the columbic energy terms.  $V_{ee}[\rho]$ , describes electron-electron repulsion, while  $V_{Ne}[\rho]$  is the electron-nuclei attraction.  $E^{xc}[\rho]$  is the exchange-correlation energy.

Since the explicit forms of  $T[\rho]$  and  $E^{xc}[\rho]$  are unknown, further approximations are required. Firstly approximation is the local density approximations (LDA). In LDA, the functional  $T[\rho]$  and  $E^{xc}[\rho]$  for a single electron is approximated by the exchange-correlation energy in a homogeneous electron gas at the same local density. This method tends to favor more homogenous systems over binds molecules and solids[117, 119]. In addition, many experimental physical properties can be predicted to a good level of precision. However this approximation has tendency to underestimate lattice parameter due to its overestimation of

cohesive binding. In addition, the energies of the state and Van der Waals interaction may not be appropriately estimated[120].

The LDA is limited in systems where the density undergoes rapid changes such as in molecules. This limitation is due to its approximation of energy of true density by energy of a local constant density. To correct the limitation in LDA, an improvement is made by using the gradient of density of electrons, namely, generalized-gradient approximation (GGA)[121]. GGA is successful for small molecules but fails for delocalized electrons in simple metal. GGA improves upon the LDA in description of atoms and solids, and it also tends to improve the total energies and atomization energies. This approximation tends to improve energy gap between valence and conduction bands in the cases of semiconductor and insulator material. Therefore, GGA is efficient in computational cost and is numerically accurate and reliable. Thus GGA tends to satisfy the demands of quantum mechanics and solid state physics[116, 118].

In order to calculate the wavefunctions  $\psi(r)$ , the Hamiltonian in equation 3.5 ought to be calculated. This is done by an appropriate choice of basis sets. Most of the basis sets are well developed and proven effective, such as linear combinations of atomic orbital (LCAOs), linearized augmented plane waves (LAPWs) and plane-wave/pseudopotential approaches[116].

DFT is one of the most precise methods to study many physics and chemistry phenomena at electron level. However, since it deals with ground state energy and neglect thermal contributions, all properties and calculations from DFT correspond to those at absolute zero temperature.

### 3.2. Molecular Mechanics and Molecular Dynamics

Macromolecules, such as polymers and their composites contain a large number of atoms. Consequently, potential based methods that are computationally cheaper are utilized for these systems. A large simulation cells is required to effectively represent long range order [114] in such large systems. In this work, we aim to utilize classical molecular dynamics (MD)[6, 112, 122, 123] to simulate polyurethane and its graphene-polyurethane nanocomposite at atomic level. The following section discusses brief description of MD method including force field used to describe various interactions in a molecular system. The

purpose of this review is not to present a full treatise of this method, but simply to introduce basic concepts involved in MD technique.

### 3.2.1. Molecular Mechanics

Molecular mechanics or force field [122], rely on laws of classical Newtonian mechanics, and experimentally derived parameters, to calculate optimum geometry of a molecule as a function of potential energy [111]. The potential energy function  $E(r_1, r_2, \dots, r_N)$  is a function of the positions of nuclei. It is calculated from relative positions of the atoms with respect to a give conformation of a molecule. Forces are derived as gradients of the potential energy functions with respect to atomic positions. Some of the most commonly used potential energy functions are the CHARMM, AMBER, CFF, PVFF, Dreiding, universal and CVFF. In general, choice of a particular force field depends on a systems property of interest. Some applications, for example, polymers where computational of energy is required at every time step may require more refined force field than others. Therefore it is important to keep potential energy function as simple as possible, and sacrifice as less as possible in terms of accuracy.

Force fields differ in their parameters, cross terms and method of development and are classified in different classes. First generation force fields like CHARMM, AMBER and CVFF are based on parameterization with experimental data, and have a simpler functional form. Second generation forced field is developed by high parameterization such as CFF, PCFF, COMPASS etc. The new generation force fields incorporate polarizability. Rule based force fields like Universal and Dreiding where parameters are decided by rules such as hybridization. The force field used for this study is the Dreiding force field[124]. Dreiding force field was chosen because property predicted for polymer systems using this force field has given good agreement with experimental values in the past[125, 126].

#### 3.2.1.1. Dreiding Force-field

Dreiding force field is useful for predicting structures and dynamics of organic, biological, and main-group inorganic molecules. Dreiding uses general force constants and geometry parameters based on simple hybridization considerations, instead of individual force constants, and geometric parameters that depend on particular combination of atoms involved

in bond, angle, or torsion terms. Consequently, all bond distances are derived from atomic radii, and there is only one force constant each for bonds, angles, and inversions and only six different values for torsional barriers [112]. It makes it possible to define parameters for all possible combinations of atoms, and new atoms are added to the force field without difficulty. The total energy in Dreiding force field is expressed as sum of bond ( $E_{\text{bond}}$ ) and non-bonded interactions ( $E_{\text{non-bond}}$ ); Each of these terms is described below and summarized in Table 3.

$$E_{\text{total}} = E_{\text{bond}} + E_{\text{non-bond}} \quad (3.7)$$

$$E_{\text{bond}} = E_{\text{bond-stretching}} + E_{\text{angle-bending}} + E_{\text{torsion}} \quad (3.8)$$

$$E_{\text{non-bond}} = E_{\text{vdw}} + E_{\text{coulomb}} + E_{\text{hydrogen-bonding}} \quad (3.9)$$


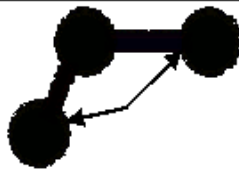

**Bond Stretching Energy (two-body):** When a bond is compressed or stretched energy goes up. The energy potential for bond stretching is described by Dreiding force-field as either a simple harmonic oscillator or as a Morse function[124]. The harmonic equation in Table 3 estimates the energy associated with vibration about the equilibrium bond length,  $R_e$ , while Morse functions described energy using anharmonic term near equilibrium. The Morse function gives a better description of the energy, since it includes the anharmonic term near equilibrium. This leads to a finite energy ( $D_e$ ) for breaking the bond[124]. Moreover if starting structure of a system is far from equilibrium than from the energy derivative of Morse function, the calculated restoring force will be very less and hence harmonic function perform better in quickly equilibrating the structure[124]. The  $k_e$  parameter controls the stiffness of the bond spring, while  $R_e$  defines its equilibrium length. Unique  $k_e$  and  $R_e$  parameters are assigned to each pair of bonded atoms based on their types (e.g. C-C, C-H, O-C, etc.). The Morse scale parameter  $\alpha$  is related to harmonic force constant by comparing the second derivative of energy [124]. The values of these parameters are set in the force-field file, which is used for MD simulation.

**Angle Bending Energy (three-body):** As angles are bent from their initial position, the energy increases due to bending of the harmonic cosine form or the harmonic angle form [124]. The harmonic cosine form is preferred over harmonic angle form (Table 3). This is because it does not lead to a zero slope as the angle approaches  $180^\circ$  [124]. These equations



estimate the energy associated with vibration about the equilibrium bond angle. The  $k_\theta$  parameter controls the stiffness of the angle spring,  $\theta_0$  while defines its equilibrium angle.

Table 3: Different type of interactions for that define a force-field

Bond stretching/compression (2-body)		
$\frac{1}{2}k_r(R-R_0)^2$	Harmonic	
$D_e(e^{-a(R-R_0)} - e^{-aR_0})^2$	Morse function	
Bond angle bending (3-body)		
$\frac{1}{2}k_\theta(\theta - \theta_0)^2$	Harmonic in $\theta$	
$\frac{1}{2}k_\theta(\cos\theta - \cos\theta_0)^2$	Harmonic in $\cos\theta$	
Torsions/dihedral (4 -body)		
$\frac{1}{2}V_n \{1 - \cos [n_\phi(\phi - \phi_0^0)]\}$		
Non-bonded interactions		
$E_{LJ}^{ij} = AR^{-12} - BR^{-6}$	Leonard-Jones 12-6 potential	
$E_{Exp}^{ij} = AR^{-C_2} - BR^{-6}$	Exponential-6 potential	
$E = k \frac{q_i q_j}{r_{ij}}$	Coulomb interaction with dielectric constant $k$	

**Torsion energy (four-body):** The torsion is as a result of interaction of two bodies. The two bodies are connected via a common bond, and energy the torsion energy is zero at equilibrium angle and never negative [113]. The dihedral angle  $\phi$ , is angle between IJK and JKL plane,  $n_{jk}$  is the periodicity,  $V_{jk}$  is the barrier to rotation, and  $\phi_{jk}^0$  is the equilibrium angle. The torsion energy in MM is used to correct the remaining energy terms rather than to represent a physical process. The torsion energy represents amount of energy added to or subtracted from the bond, angle bend, and non-bonded interaction energy terms to make total energy agree with experiment or rigorous quantum mechanical calculation [113].

**Van der Waals interaction:** Van der Waals interaction between two atoms arises from a balance between repulsive and attractive forces and is expressed in two ways, as Leonard-Jones 12-6 (LJ) expression and as exponential 6 form (X6) [124]. The difference between the two forms is the way of describing the repulsive part. The repulsive forces in the LJ potential arise at short distances where the electron-electron interaction is strong, hence throws atoms away[113]. The LJ potential requires only two parameters for the evaluation of the potential and is faster to compute, than the exponential 6 form which shows a better agreement for short range interactions. The default form used in the Dreiding force-field is LJ[124].The parameter values are calculated differently if the interaction concerned is between two different types of atoms. The way it is calculated can be based on arithmetic or geometric combination of the parameters of the pure system.

**Electrostatic interaction:** The electrostatic interaction between pair of atoms is represented by Coulomb potential  $K$ , is the effective dielectric function for the medium and  $r$  is the distance between two atoms having charges  $q_i$  and  $q_k$ . Interactions are not calculated for atoms bonded to each other (1, 2 interaction) and those involved in angle terms (1, 2, 3 interactions) as these are taken care by bond and angle stretching interactions[113].

**Hydrogen Bonding:** Hydrogen bonding occurs when an atom of hydrogen is attracted by strong forces to two atoms instead of only one, so that it may be considered to be acting as a bond between. Dreiding uses a separate term to account for hydrogen bonding to describe interaction involving hydrogen atom with that of very electronegative atoms (e.g. N, O, F) associated with hydrogen bond.

### 3.2.2. Molecular Dynamics

Molecular dynamics (MD) simulations are used for molecular scale analysis of various materials phenomena [55], including thermal, mechanical, surface and optical properties. The MD method calculates time-dependent behavior of a molecular system described by point charges and point masses in the classical regime. The basic idea in molecular dynamics is to follow motion of all atoms in a system by solving the Newton's equations of motion given by;

$$F_i = m_i a_i \quad (3.9)$$

where  $F_i$  is the force exerted on a particle  $i$ ,  $m_i$  is the mass and  $a_i$  is the acceleration of particle. Integration of these equations gives a trajectory, which describes position, velocities and acceleration of particles as they vary with time. The generated trajectories are connected to obtain macroscopic thermodynamic quantities using the principles of statistical mechanics. The thermodynamic properties can be calculated by averaging the trajectories using

$$A_\tau = \frac{1}{\tau} \int_0^\tau dt A(t) \quad (3.10)$$

where  $A$  is the property of interest and  $\tau$  is the time.

MD simulation is inevitably restricted by computational power. Since the typical time scale for atomic motions is of the order of a picosecond ( $10^{-12}$ ) or less, we should use values of the order of a femtosecond ( $10^{-15}$ ) for the time step  $\Delta t$  to keep the numerical errors small. Therefore, it takes many more than a million iterations to follow motion of a single atom for just a microsecond. Moreover, number of calculations required grows rapidly as number of atoms  $N$  in the system increases. Under these circumstances, we should satisfy ourselves with the calculation of a small system with fewer than a million atoms and a short physical process over less than a few microseconds.

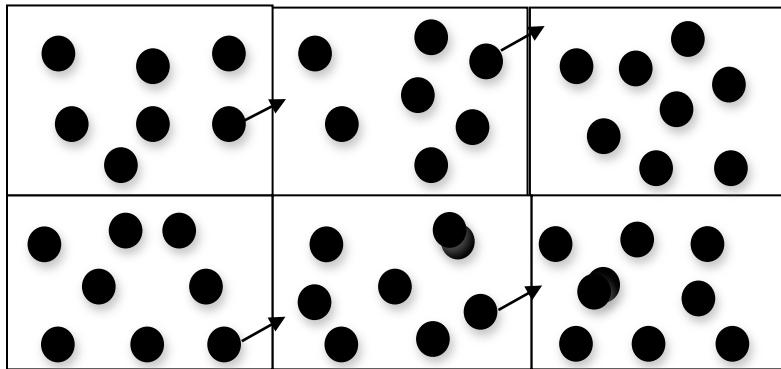


Figure 10: An illustrative view of periodic boundary conditions.

Thus there is always a large discrepancy in both length and time scale between the macroscopic system and simulation system we can handle. For example, the typical size of a million atom system is as small as a few tens of nanometers, which means that simulation system is far from macroscopic. There are numerous examples in literature where MD

simulations of amorphous polymers or polymer-nanocomposite systems. It is not possible to discuss all examples here. For reviews, the reader is referred to [55-59].

The thermo physical properties, chain dynamics and mechanisms in polymeric materials and their nanocomposites can all be accurately quantified in a typical MD simulation. Furthermore, MD simulations allow monitoring of the dynamics of the polymer and nanocomposite system, provide detailed molecular descriptions of the events involved, and can predict the relative position and orientation of the graphene in the polymer. In the following section, the MD method is described in detail, followed by a critical inspection of the current models used for simulating polymer-nanocomposite systems.

### 3.2.2.1. Periodic Boundary Conditions

In MD simulations periodic boundary conditions (PBCs) are used to avoid problems with boundary effects. All atoms are confined in a simulation box and the boundaries are obtained by extending the lattice, as shown schematically in Figure 10. By repeating this procedure, we can fill the whole space with the original configuration and its replicas. Consequently, an atom leaving the box to the right through one boundary can be identified with an atom entering from the left at the opposite boundary.

A system constructed in this way is taken as having infinite size and an infinite number of atoms. Of course the periodic system cannot be identical to an infinitely large bulk system. The drawback of this approach is that in many situations, structures grow rather quickly and the simulation area can get too big quite rapidly.

### 3.2.2.2. Integration Algorithm of Equations of Motion

The potential energy is a function of the atomic positions ( $3N$ ) of all atoms in a system. The complexity of this function to solve the equation of motion at each time step is solved numerically. Numerous numerical algorithms used to integrate the equations of motion are, Verlet algorithm, Leap-frog algorithm and Velocity Verlet. In choosing which algorithm to use, one should consider the following criteria: The algorithm should conserve energy and momentum. It should be computationally efficient and in addition to allowing a

long time step for integration. The chosen technique also plays a key role in the accuracy of the simulation.

*Verlet Algorithm:* The solution of Newton's equation using Verlet algorithm is based on a Taylor series expansion. Expanding the position of the  $i$ th particle  $r_i$  at time  $t+h$  and  $t-h$  in Taylor series yields

$$r_i(t+h) = r_i(t) + hr'_i(t) + \frac{h^2}{2!} r''_i(t) + \frac{h^3}{3!} r'''_i(t) + O(h^4) \quad (3.11)$$

$$r_i(t-h) = r_i(t) - hr'_i(t) + \frac{h^2}{2!} r''_i(t) - \frac{h^3}{3!} r'''_i(t) + O(h^4) \quad (3.12)$$

Adding the two equations leads to the results

$$r_i(t+h) + r_i(t-h) = 2r_i(t) - h^2 r''_i(t) + O(h^4) \quad (3.14)$$

Solving for  $r_i(t+h)$  and using Newton's equations for the acceleration ( $\vec{a}_i = \vec{F}_i/m_i$ ) leads to

$$r_i(t+h) = 2r_i(t) - r_i(t-h) + \frac{h^2}{m_i} F_i(t_n) + O(h^4) \quad (3.15)$$

Discrediting time in this equation leads to the Verlet algorithm (1967), the most widely used integration technique for its simplicity and accuracy;

$$r_i(t_{n+1}) = 2r_i(t_n) - r_i(t_{n-1}) + \frac{h^2}{m_i} F_i(t_n) + O(h^4) \quad (3.16)$$

The Verlet Algorithm relies on two previous time steps,  $t_n$  and  $t_{n-1}$ , and it is a fourth-order method. There are sometimes problems associated with Verlet algorithm due to a potential loss of accuracy when Eq. (6) is implemented. The final term in this equation tends to be small compared to the others, since this term can get lost in the round-off error. As a result if the position of an atom is known, the position of the same can be calculated from this simple equation without even having the knowledge of the velocity of the atom. The Verlet algorithm uses no explicit velocities. The advantages of the Verlet algorithm are, i) it is

straightforward, and ii) the storage requirements are modest. The disadvantage is that the algorithm is of moderate precision.

*Leap frog algorithm:* In an attempt to correct some of the problems associated with the original Verlet algorithm, the Verlet Leapfrog algorithm was developed. Using an approximation for the derivative, the velocity at the midpoint between times  $t_n + t_{n+1}$  can be defined

$$v_i(t_{n+1/2}) = \frac{r_i(t_{n+1}) - r_i(t_n)}{h} \quad (3.17)$$

Solving for  $r_i(t_{n+1})$  yields,

$$r_i(t_{n+1}) = r_i(t_n) + hv_i(t_{n+1/2}) \quad (3.18)$$

Similarly defining the velocity at midpoint between  $t_n + t_{n-1}$  gives

$$v_i(t_{n-1/2}) = \frac{r_i(t_n) - r_i(t_{n-1})}{h} \quad (3.19)$$

The acceleration at time  $t_n$  can be defined using another approximate formula for the derivative,

$$a_i(t_n) = \frac{v_i(t_{n+1/2}) - v_i(t_{n-1/2})}{h} \quad (3.20)$$

Using Newton's equation of the acceleration  $a_i(t_n) = (F_i(t_n)/m_i)$  and equating the acceleration equation about yields

$$\frac{v_i(t_{n+1/2}) - v_i(t_{n-1/2})}{h} = F_i(t_n)/m_i \quad (3.21)$$

Which can be solved for  $v_i(t_{n+1/2})$ ,

$$v_i(t_{n+1/2}) = v_i(t_{n-1/2}) + \frac{h}{m_i} F_i(t_n) \quad (3.22)$$

Equations (3.17) and (3.22)) constitute equations of Verlet Leapfrog algorithm. The Leapfrog algorithm has some advantages over the original Verlet algorithm, Eq. (3.16). First, the loss of accuracy due to round-off error in the original Verlet algorithm because of vastly different magnitudes of terms in the equation is corrected. Second, the velocities are included explicitly in the method, unlike the original Verlet algorithm. There are still a few problems associated with the Leapfrog algorithm, however. First, it is still not self-starting. This can be overcome as in the original Verlet method by completing one step of the Euler method first, and then switching to the Leapfrog algorithm for subsequent steps.

*Velocity Verlet:* Another variant is the Velocity Verlet, which used the equations (3.23) and (3.24) to integrate the equation of motion.

$$r(t + t\Delta) = r(t) + v(t)\Delta t + \frac{f(t)}{2m}\Delta t^2 + \dots \quad (3.23)$$

$$v(t + t\Delta) = v(t) + \frac{f(t+t\Delta)+f(t)}{2m}\Delta t + \dots \quad (3.24)$$

In this algorithm the new positions are calculated, based on which the new velocities and from those the new forces on atoms.

### 3.2.2.3. Ensemble Details

A statistical ensemble is an assembly consisting of a very large number of similarly prepared systems. The collection of these systems may be under the same macroscopic or thermodynamic conditions, but with different microscopic details. Ensembles are differentiated by three different thermodynamic variables kept constant, as summarized below

NVE – indicate that the number of particle (N), volume (V), and Energy (E) are kept constant in MD simulations. This ensemble is used to check the connections of an algorithm. Correspondingly it tests the adequacy of a time step by checking conservation of total energy. It is known as microcanonical ensemble.

In NVT, the energy of the system is allowed to fluctuate as if the system was in thermodynamic equilibrium with a bath at fixed temperature (T) by using thermostat. The temperature is maintained at a specified average macroscopic value through the use of

thermostat algorithms, while the total energy ( $E$ ) of the system can fluctuate. The extended system method has been widely used because it produces a canonical distribution of microstates[123]. It is also referred to as canonical ensemble (NVT),

In NPT, or isobaric-isothermal statistical ensemble, the volume of the system is allowed to fluctuate in the same way as it would for a system in thermodynamic equilibrium with pressure ( $P$ ) bath at fixed pressure (usually 1 atm). The ensemble is important in systems where chemical reactions are carried out under constant pressure conditions.

In  $\mu$ VT or the grand canonical ensemble ( $\mu$ VT) has a constant volume ( $V$ ) and temperature ( $T$ ), but exchanges particles with a surrounding bath. In this case, the chemical potential ( $\mu$ ) of the different species is maintained at a specified value, but the instantaneous particle number ( $N$ ) can fluctuate. To construct the grand canonical ensemble, the system is enclosed in a container that is permeable both to heat and to the passage of particles. The number of particles in the system can range over all possible values. Other ensembles are possible, but of more limited practical application.

#### 3.2.2.4. Temperature and pressure control methods

To compare the simulation results with the experimental results, one needs to control the thermodynamic conditions of the system, such as the temperature and the pressure of the simulation system. The techniques for controlling the temperature are velocity scale, Nose-hoover, Andersen, and Berendsen[6]. Velocity scale controls the kinetic temperature of a system and brings it to equilibrium by maintaining the temperature within a given range of the target temperature. When the temperature drifts outside of the specified range the atomic velocities are simply scaled back into range. Velocity rescaling method is physically unrealistic and should not be used for true temperature control. For Nose, Andersen, and Berendsen control the thermodynamic temperature and generate the correct statistical ensemble, by allowing the system to exchange energy with a heat bath.

Pressure in a MD simulation is controlled using Parinello, Andersen, Nose and Berendsen approaches[6]. The Parinello method is useful for studying the stress-strain relationship in materials. Both the shape and the volume of the cell can change, which allows the internal stress of the system to match the externally applied stress. The Andersen and Nose method allows changing of the volume of the cell but keeps the shape fixed by allowing



the cell to change isotropically. The Berendsen method involves changing the pressure by altering the coordinates of the particles and the size of the cell, the shape is also kept fixed [123].

## 4. NONELASTIC BEHAVIOR OF GRAPHENE: FIRST PRINCIPLE AND MOLECULAR MECHANICS CALCULATIONS

### 4.1. Motivation

The discovery of graphene has attracted a growing research interest in basic science to cutting edge nanotechnology [42, 43, 48, 127]. Even though most explored property of graphene is in unconventional physics behind its electronic behavior[80], extensive studies have also been devoted to exploit the mechanical properties of graphene [68, 128-130]. Mechanical properties of graphene are critical for practical applications that require deformation and mechanical interactions. Applying compressive strain and measuring critical stress is used to estimate these properties. Critical strain is the amount of strain that graphene can withstand without failure. Nonetheless at temperature of 0K, both linear and quadratic terms in the dispersion of flexural modes are responsible for material failure. Quantitatively thermal fluctuations are a measure for failure mode at finite temperature. Various researchers have investigated graphene subjected to the tensile uni-axial strain to understand the underlying microscopic behavior [69, 129, 131], not only theoretically, but also with the support from properties observed experimentally [67, 69, 132].

The first experimental measurements of mechanical properties of single layer graphene was achieved by Lee et al.[67]. They measured the deflection at the center point of circular graphene sheets in nano-indentation experiments, and obtained strikingly consistent results that indicated defects were almost entirely absent. They calculated the elastic modulus and intrinsic strength of defect free monolayer graphene sheet to be 1.0 +/-TPa and 130 GPa, respectively[67], assuming a graphene sheet thickness of 0.335nm. They used a second order polynomial in the Green strain to the uniaxial stress-strain behavior of their graphene sheets, but it was calibrated for only uniaxial tension. These tests made graphene the strongest material ever measured. The elastic modulus of monolayer graphene sheet performed via chemical reduction in graphene oxide has been determined to be about 0.25 TPa by indentation of an atomic force microscopy tip at the center of a suspended graphene sheet[133]. Poot et al. [134]measured bending rigidity and tension of circular graphene sheets and predicted their fundamental resonance frequencies. Lee et al. [132] measured the friction characteristics of graphene using atomic force microscopy. These important

experimental studies have made it possible to assess the adequacy of various mechanical models for graphene.

Theoretically, graphene was first explored in 1947, by Wallace P.R reported the band structure of graphene [50]. However, it was presumed thermodynamically unstable and could not exist in a free state. This was attributed to the melting temperatures of thin films. Later, Sanchez-Portal et al[70], and Van Lier et al.[69] calculated the Young modulus of graphene sheets using DFT, in both studies, they used the results to estimate the elastic properties of open and close carbon-nanotubes. Kudin and Scuseria[135] evaluated to the flexural rigidity of carbon nanotubes by bending graphene using DFT. Liu *et al.*[136] employed *ab initio* simulation to investigate the ideal strength and phonon instability of graphene using nonlinear elastic response. From their results, they determined the strength of a perfect graphene lattice as 110GPa and 121GPa, along zigzag and armchair directions, respectively. Wei et al[137] calculated the nonlinear in-plane elastic properties of graphene using DFT. Huang et al. used a Taylor series approach closely related to the Cauchy-Born rule to study the elastic properties of graphene made an extensive study of previously published values for Young's modulus and the role of the thickness" of the carbon sheet on the elastic modulus. Scarpa et al. [131] proposed a truss-type analytical model to describe the in-plane linear elastic properties of graphene. Zhao et al. [138]probed the dependence between the size and chirality of graphene nanoribbons and their elastic properties.

While theoreticians depend on experiments to develop constitutive equations, this approach is often limited, particularly for very small crystals. By means of quantum mechanics, response of a crystal to various loadings can easily be obtained, and a reliable. First principles-based studies on large systems require tremendous computing power. It is expensive to simulate graphene sheets composed of more than 10,000 atoms on any current computing system with DFT calculations. Force-field-based molecular mechanics (FF-MM) simulations of this size and larger are computationally feasible, however the elastic properties arising from commonly used empirical potentials for carbon, such as the Tersoff [152]and Brenner potential [139], show spurious anisotropy at small strains, and are generally inconsistent with DFT results. For example, Liu et al. [136] showed that the tensile stress-strain behavior for different chirality's are nearly identical until 15% strain; whereas the stress-strain behavior are distinctly different using the Tersoff and Brenner

potential[140]. This is often problematic in coupled quantum/atomistic computations as discussed in Khare et al. [141]. An energy scaling scheme was presented by Khare et al. [142] that matches the strength obtained from FF-MM simulations to the DFT results, but this approach lacks generality. It remains unclear how to develop a generalized scaling function that is applicable for arbitrary strain states, such as the strain yields surrounding defects.

Since the future objective in the field of nanotechnology is to design graphene for nanodevice applications, such as nanorobots, nanosensor and nanocomposites. As such research on graphene as reinforcing nanofiller in polymer nanocomposites, continues to gain immense attention for structural applications due to superior mechanical, thermal and electronic properties. Therefore, in order to understand the effect of graphene on the mechanical properties of polyurethane polymer matrix, it is essential to understand the mechanical behavior of graphene under finite or infinitesimal strains. Particularly, studying the elasticity of graphene is critical in explaining the ideal strength of a defect free graphene at 0K. The ideal strength is a crucial theoretical parameter because it fundamentally characterizes the nature of chemical bonding[143]. In addition, understanding the mechanical properties of each component in the nanocomposite (i.e polymer matrix and nanofiller) is important in designing a desirable nanocomposite.

This section focuses on modeling and simulations of mechanical behavior of graphene. Both *ab initio* and molecular mechanics (MM) methods are used to predict mechanical behavior of graphene. These two methods complement each other so that the quantitative values of the elastic properties are determined in quantum scale, and from discrete models at the atomistic scale using continuum theory of elasticity. Firstly, *ab initio* calculations were performed using DFT modeling to study mechanical properties of 2-D graphene crystal. Second, while DFT modeling is restricted to a few atoms, we used MM based on empirical potentials to predict mechanical properties of graphene monolayer. In both simulation approaches, elastic constants were calculated from the relationship between strain energy and strain tensors. The two approaches complement each other so that effective mechanical properties are properly defined in the first principle calculations, while quantitative values are determined from discrete models at atomistic scale. Understanding the mechanical properties of the nanofiller is essential in designing polymer nanocomposite.

## 4.2. Theoretical Framework

An accurate determination of material mechanical properties is a complicated issue involving meticulous analysis of elastic constants and bulk modulus. In this section, we present the theoretical framework and computational details used to describe (1) equation of state used to investigate the 2-D graphene system, (2) elasticity theory to determine second order elastic constants (SOEC) and third order elastic constant (TOEC) of graphene from strain energy and applied strain relationship.

### 4.2.1. Equation of State

The equation of state (EOS) describes bulk properties, such as lattice constant, atomic positions, bond lengths, and bulk modulus for solids under high hydrostatic pressure. EOS is obtained by postulating approximate relationships between elastic free energy stored in solid and finite volumetric strain to which it is submitted. In two-dimensional systems such as graphene, the EOS can be deduced using an approximate relationship between *elastic* free energy stored in the solid and finite strain over the surface area. Thus, EOS is found by using thermodynamics definition of pressure;

$$P = -A_0 \frac{\delta F}{\delta A} \quad (4.1)$$

The resulting curve  $V/V_0 = P$  of relative compression vs. pressure  $P$  (where  $V$  is the volume at given pressure  $P$  and  $V_0$  is the volume at atmospheric pressure  $P_0 \approx 0$ ) is fitted by a theoretical or empirical equation of state.

In our work we performed a series of total energy calculations as a function of volume, and used second order Birch-Murnaghan (BM) equation of state[144] to fit the data. BM equation is obtained by assuming that the free energy can be expanded into a series of powers of the Eulerian strain (using the final deformed state as the reference configuration). According to BM equation, convergence is better when free energy is expanded in terms of Eulerian strain rather than in terms of Lagrangian strain (where the initial un-deformed state is the reference configuration). This is essentially due to the coefficient term of the third

order in the expansion can be neglected in many cases (corresponding to  $B_0' \approx 4$ ), so that the equation of state at second order is good enough. The BM equation is written as:

$$E(V) = E_o + \frac{9}{16} V_o B_o \left[ \left( \frac{V_o}{V} \right)^{2/3} - 1 \right]^3 B_0' + \left[ \left( \frac{V_o}{V} \right)^{2/3} - 1 \right]^2 \left[ 6 - 4 \left( \frac{V_o}{V} \right)^{2/3} \right] \quad (4.2)$$

Where  $E_o$  is the equilibrium energy,  $V_o$  is the equilibrium volume,  $B_o$  is the bulk modulus and  $B_0'$  is the first bulk modulus derivative of the stress–strain response curves over to a maximum point that defines the intrinsic breaking stress[67]. To obtain the volume of the 2D graphene system, we assumed 0.335nm lattice spacing.

#### 4.2.2. Nonlinear Elastic Theory

In finite-strain continuum elasticity theory of elastic deformation, calculations of elastic constants provide a complete description of the elastic response of a solid material [115, 127, 144-146]. For a single crystal, elastic behavior arising from small infinitesimal deformation results in lowest-order (quadratic) term, i.e, the second-order elastic constants (SOECs). SOECs are sufficient to describe stress-strain response of materials to linear deformation, including wave propagation in solids. Conversely, in finite strains, non-linear elasticity is required and higher-order elastic constants, such as third-order elastic constants (TOECs), is used to describe the nonlinear elastic behavior of a material. Knowledge of TOECs is used to determine changes in acoustic velocities due to elastic strain[115, 146], equation of state and thermal properties of a solid[146, 147]. Therefore, both SOECs and TOECs are important parameters not only for modeling mechanical effect of crystals, but also to interpret amplitude stress wave propagation in single crystals[127]. Moreover, SOEC and TOEC values are also utilized in development of ion-electron pseudopotentials [148] or empirical interatomic potentials[149]. The elasticity of graphene is considered nonlinear because the stress–strain response curves over to a maximum point that defines the intrinsic breaking stress[67].

Within the theoretical framework of nonlinear elasticity, the mechanical properties can be derived from a strain energy density function. This function depends on the

deformation gradient tensor under homogenous deformations. Hence, we will review some fundamental facts from nonlinear theory of elasticity and apply it on 2D graphene. Given the graphene atomic unit cell with lattice vectors  $a_1$  and  $a_2$  (Fig 11) in an un-deformed state, after applying a homogeneous deformation, lattice vectors of the deformed state move by a displacement  $u$ , from its original position to a new one  $x$ . Such that  $x=a+u$ . This changes is depicted by a deformation gradient  $F$

$$F_{ij} = \frac{\partial x_i}{\partial a_j} \quad (4.3)$$

The finite strain or Langragian strain  $\eta$  matrix is then derived according to the relation given by

$$\eta_{ij} = \sum_K \frac{1}{2} (F_{ki} F_{kj} - \delta_{ij}) \quad (4.4)$$

where  $\delta_{ij}$  is the Kronecker delta. The Langragian strains are symmetric in nature,

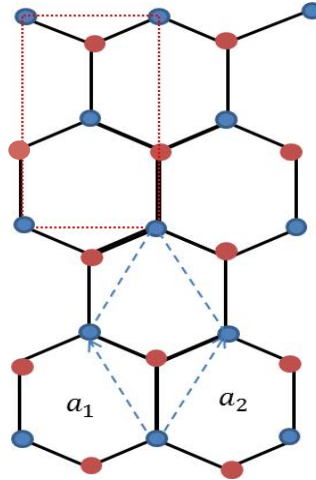


Figure 11: Undeformed graphene lattice; four-atom unit cell enclosed by rectangular red-dashed line in sub-lattice A. Two atom unit cell enclosed by rhombhedron red-dashed line in sub-lattice B.

thus contain no information on rigid rotation on a material, however, they are convenient measure of deformation for an elastic body.

From a continuum perspective, the elastic properties for nonlinear behavior, it is determined by expanding the internal energy  $U$  as a Taylor series in the Lagrangian strain  $\eta$  and has a functional form of

$$U(A_0, \eta_{ij}) = U(A_0, 0) + \frac{1}{2} \sum_{ijkl} C_{ijkl} \eta_{ij} \eta_{kl} + \frac{1}{6} \sum_{ijklmn} C_{ijklmn} \eta_{ij} \eta_{kl} \eta_{mn} + \dots, \quad (4.5)$$

Where  $U(A_0, 0)$  and  $A_0$  are the initial internal energy and the area of unreformed graphene, respectively. Using the Voigt notation to reduce the number of indexes for convenience  $(xx) \rightarrow 1, (yy) \rightarrow 2, (xy) \rightarrow 3$ , then, the energy equation can be written as

$$U(A_0, \eta_{ij}) = U(A_0, 0) + \frac{1}{2} \sum_{ij=1,3} C_{ij} \eta_i \eta_j + \frac{1}{6} \sum_{ijk=1,3} C_{ijk} \eta_i \eta_j \eta_k + \dots, \quad (4.6)$$

Herein  $C$  denotes each higher-order elastic modulus tensor, where  $C_{ij}$  and  $C_{ijk}$  are SOEC and TOEC respectively. By setting the initial energy  $U(A_0, 0)$  to 0, and using the internal energy per unit area one can write

$$C_{ij} = \frac{1}{A_0} \left. \frac{\delta^2 U}{\delta \eta_i \delta \eta_j} \right|_{\eta=0} \quad (\text{SOEC}) \quad (4.7)$$

$$C_{ijk} = \frac{1}{A_0} \left. \frac{\delta^3 U}{\delta \eta_i \delta \eta_j \delta \eta_k} \right|_{\eta=0} \quad (\text{TOEC}) \quad (4.8)$$

Noting the symmetry in the stress and strain tensors of a 2D hexagonal, a fourth SOEC tensor can be reduced to a 3x3 symmetric matrix with only 4 non-zero SOEC terms, and two of them are independent ( $C_{11}$  and  $C_{12}$ ). Upon accounting or the symmetry of the atomic lattice of grapheme, the linear elastic constitutive relationship for the 2D grapheme is simplified to

$$C_{ij} = \begin{pmatrix} C_{11} & C_{12} & 0 \\ C_{21} & C_{22} & 0 \\ 0 & 0 & C_{33} \end{pmatrix} \quad (4.9)$$



where  $C_{11}=C_{22}$  and the isotropy dictates that  $C_{33} = \frac{1}{2}(C_{11} - C_{12})$ . The 2D components correspond to the in-plane isotropic linear elasticity of which Young's modulus (E) and Poisson's ratio ( $\nu$ ) is obtained by

$$E = \frac{C_{11}^2 - C_{12}^2}{C_{11}} \quad (4.10)$$

$$\nu = \frac{C_{11}}{C_{12}} \quad (4.11)$$

Similarly, the components of TOEC can be determined from symmetry of grapheme atomic lattice. Previous studies have shown that there are three independent non-zero in plane components of the TOEC tensor. The five independent SOEC and TOEC of graphene are determined by a least-squares fit of stress-strain results from first principle calculations.

$$\sum_{I,J} IJ = C_{IJ} \eta_I \eta_J = (\eta_1, \eta_2, \eta_6) = \begin{pmatrix} C_{11} & C_{12} & 0 \\ C_{12} & C_{11} & 0 \\ 0 & 0 & C_{11} - C_{12} / 2 \end{pmatrix} \begin{pmatrix} \eta_1 \\ \eta_2 \\ \eta_6 \end{pmatrix} \quad (4.12)$$

From in plane SOEC and TOEC components  $\sum_1, \sum_2, \text{and } \sum_6$  for arbitrary in-plane deformation  $\eta_1, \eta_2, \text{ and } \eta_6$  are:

$$\sum_I = (C_{11}\eta_1 + C_{12}\eta_2) + \frac{1}{2} \left\{ C_{111}\eta_1^2 + (C_{111} - C_{222} + C_{112})\eta_2^2 + \left( \frac{3}{4}C_{222} - \frac{1}{2}C_{111} - \frac{1}{4}C_{112} \right)\eta_6^2 + 2C_{112}\eta_1\eta_2 \right\}$$

$$\begin{aligned} \sum_2 &= (C_{12}\eta_1 + C_{11}\eta_2) + \frac{1}{2} \left\{ C_{112}\eta_1^2 + C_{222}\eta_2^2 \left( \frac{1}{2}C_{111} - \frac{1}{4}C_{222} + \frac{1}{4}C_{112} \right) \eta_6^2 + 2(C_{111} - C_{222} + C_{112})\eta_1\eta_2 \right\} \\ \sum_6 &= \frac{C_{11} - C_{12}}{2} \eta_6 + \frac{1}{2} \left\{ \left( \frac{3}{2}C_{222} - C_{111} - \frac{1}{2}C_{112} \right) \eta_1\eta_6 + \left( C_{111} - \frac{1}{2}C_{222} - \frac{1}{2}C_{112} \right) \eta_2\eta_6 \right\} \end{aligned} \quad (4.13-4.15)$$

As a first step, we carried out three different deformations, uniaxial strain in the zigzag directions, uniaxial strain in the armchair directions and equibiaxial strain in the zigzag direction. The strain tensor in the zigzag direction is given by:

$$\eta_{ij} = \begin{bmatrix} 0 & 0 & 0 \\ 0 & \xi & 0 \\ 0 & 0 & 0 \end{bmatrix} \quad (4.16)$$

The deformation gradient then becomes:

$$\eta_{ij} = \begin{bmatrix} 1 & 0 & 0 \\ 0 & \varepsilon & 0 \\ 0 & 0 & 1 \end{bmatrix} \quad (4.17)$$

Where  $\varepsilon$  is the stretch rotation in zigzag directions determined by the Lagrangian elastic strain through equation;

$$\frac{1}{2}\varepsilon^2 + \varepsilon - \eta = 0 \quad (4.18)$$

Thus, the stress-strain relationships of the uniaxial strain in the zigzag the equations 4.19-4.21 are reduced to,

$$\sum_1 = C_{11}\eta_1 + \frac{1}{2}C_{112}\eta_1^2 + \frac{1}{6}C_{1111}\eta_1^3 + \Theta(\eta^4) \quad (4.19)$$

$$\sum_2 = C_{12}\eta_1 + \frac{1}{2}C_{111}\eta_1^2 + \frac{1}{6}C_{1112}\eta_1^3 + \Theta(\eta^4) \quad (4.20)$$

$$\sum_6 = 0 \quad (4.21)$$

For un-axial strain in the armchair directions, the strain tensors are ( $\eta_1 = 0, \eta_2 \geq 0, \text{ and } \eta_6 = 0$ )

$$\eta_{ij} = \begin{bmatrix} \xi & 0 & 0 \\ 0 & 0 & 0 \\ 0 & 0 & 0 \end{bmatrix} \quad (4.22)$$

The deformation gradient then becomes:

$$\eta_{ij} = \begin{bmatrix} \varepsilon & 0 & 0 \\ 0 & 1 & 0 \\ 0 & 0 & 1 \end{bmatrix} \quad (4.23)$$

Where  $\varepsilon$  is the stretch rotation in zigzag directions determined by the Langragian elastic strain through equation x, Thus, the stress-strain relationships of the uniaxial strain in the zigzag and armchair directions in equations 4.17 and 4.23 are reduced to

$$\sum_1 = C_{11}\eta_2 + \frac{1}{2}C_{222}\eta_2^2 + \frac{1}{6}C_{1112} + \eta_2^3 + \Theta(\eta^4) \quad (4.24)$$

$$\sum_2 = C_{12}\eta_2 + \frac{1}{2}(C_{111} - C_{222} + C_{112})C_{222}\eta_2^2 + \frac{1}{12}(C_{1111} + 2C_{1112} - C_{2222})\eta_2^3 + \Theta(\eta^4) \quad (4.25)$$

$$\sum_6 = 0 \quad (4.26)$$

Finally for the equi-biaxial strain in-plane ( $\eta_1 = \eta_2 \geq 0, \text{ and } \eta_6 = 0$ )

$$\eta_{ij} = \begin{bmatrix} \xi & 0 & 0 \\ 0 & \xi & 0 \\ 0 & 0 & 0 \end{bmatrix} \quad (4.27)$$

The deformation gradient then becomes:

$$\eta_{ij} = \begin{bmatrix} \varepsilon & 0 & 0 \\ 0 & \varepsilon & 0 \\ 0 & 0 & 1 \end{bmatrix} \quad (4.28)$$

The stress-strain relationship for is expressed as:

$$\sum_i = (C_{11} + C_{12})\eta + \frac{1}{2} \left\{ 2(C_{111} - C_{222} + 3C_{112})\eta^2 + \frac{1}{6} \left( \frac{3}{2}C_{1111} + 4C_{1112} - \frac{1}{2}C_{2222} + 3C_{1122} \right)\eta \right\} + \Theta(\eta^4) \quad (4.29)$$

$$\sum_6 = 0 \quad (4.30)$$

All five elastic constant contribute to the expression for stress-strain response for these three deformation states.

### 4.3. Computational Details

We have used both the first principle and atomic-scale calculations of SOEC and TOEC of graphene using density functional theory (DFT) and inter-atomic potential energy functions respectively. The details of DFT and molecular mechanics simulations are discussed in the previous section. The following section describes the brief overview of the computational details for the density functional and MM as it pertains to the calculations of EOS and elastic constants of graphene.

Density Functional Theory method: DFT [119] calculations were carried out with the Vienna Ab-initio Simulation Package (VASP) [150] with the projector augmented wave (PAW) methods to simulate mechanical properties of graphene. The calculations are performed at zero temperature. A vacuum space of 20 Å normal to graphene plane is used to account for van der Waal interactions between the two layers. Reciprocal space was represented by Monkhorst-Pack special k-points scheme with 14x14x1 grid meshes with 2 and 4 atoms unit cells, respectively. The structures are relaxed without symmetry constraints with cut-off energy of 700ev. To avoid any wrap around errors a sufficiently larger Fourier grid is used, including all wave vectors up to twice the cut-off number. The equilibrium

theoretical crystal structure for graphene is determined by minimizing the Hellman – Feynman force on the atoms and stress on the unit cell. The convergent of energy and force were set to 0.000eV and 0.0011 eV/Å respectively.

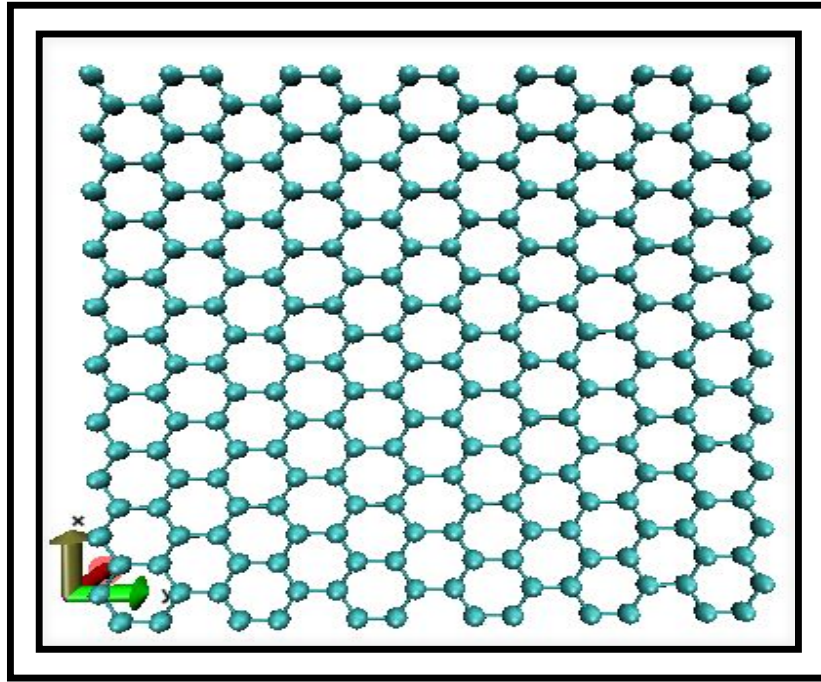


Figure 12: Orthonormal structure of graphene used for molecular mechanics simulations, with 4 graphene per unit cell and 240 atoms per simulations box.

When performing *ab initio* calculation such as elastic constant, geometry optimization, etc, it is good practice to check the convergence of the system by calculating the total energy vs cut-off energy and total energy versus number of momentum k-points for the plane wave expansion of the wave functions. We tested different cut-off energies for graphene and found the cut-off energy for 700eV to be suitable for the graphene system. Higher cut-off energies give minimum energies lower than 700eV; nevertheless the differences are very small (less than 1eV) and have no effect on the accuracy of results. In addition, we chose these cut-off energies to reduce computational cost. For both 2 and 4 graphene crystal structures the unit-cell height was set to  $c = 10 \text{ \AA}$  in order to prevent interactions between unit cells.

Molecular Mechanics Simulations method: While DFT modeling is restricted to a few hundred atoms, several empirical potentials have been developed for C-C interatomic

interactions such as Tersoff[151], and AIREBO[139], have enabled both large scale atomistic simulations and analytical predictions of elastic properties of graphene. In this study, we used two types of interatomic potentials: Tersoff[151] and a modified version of Tersoff[151]. The complete details of these potentials can be found in literature [151, 152]

The crystal structure of monolayer graphene sheet was placed in the x-y plane of a periodic box with dimensions  $a = 24.68 \text{ \AA}$ ,  $b = 25.64 \text{ \AA}$  and  $c = 20.00 \text{ \AA}$ . The monolayer graphene sheet consists 4 atoms per unit cell with a total of 240 atoms in the simulations box (Figure 12). Periodic boundary conditions were imposed in all directions. The simulation was performed using the Large-scale Atomic/Molecular Massively Parallel Simulator (LAMMPS) [163] molecular dynamics simulation package at zero temperature ( $T=0 \text{ K}$ ). We considered an infinite monolayer of graphene under conditions of hydrostatic pressure and used the Birch-Murnaghan equation of state to obtain the equilibrium parameters. In addition, the elastic constant was also calculated from the different potential and compared with DFT calculations. The MM simulation is carried out to determine the static equilibrium state of graphene by minimizing the potential energy with respect to lattice parameter. MM approach gives deterministic results based on energy minimization, and is limited to simulations of static equilibrium behavior at zero temperature ( $T=0 \text{ K}$ ). These interatomic interactions are discussed extensively in various computational reviews [152-157].

#### 4.4. Results and Discussion

In this work, calculation of mechanical properties of 2-D graphene structure was considered using two different approaches; the ab-initio calculation using density functional theory and atomistic simulation using the molecular mechanics approach. We first discuss bulk properties obtained from the equation of state followed by the elastic constants using the two approaches.

##### 4.4.1. Equation of State

We first optimized the equilibrium lattice constant for graphene. The total energy as a function of lattice parameter is obtained by specifying several lattices varying between  $2.40 \text{ \AA}$  and  $2.45 \text{ \AA}$ . A least square fit of energy vs lattice parameter with a second order polynomial functions yields equilibrium lattice parameters of  $a = 2.45 \text{ \AA}$ , which corresponds to the

minimum total energy. The theoretical lattice parameter calculated using DFT yields a value of 0.4% different from experimental value for graphite [90].

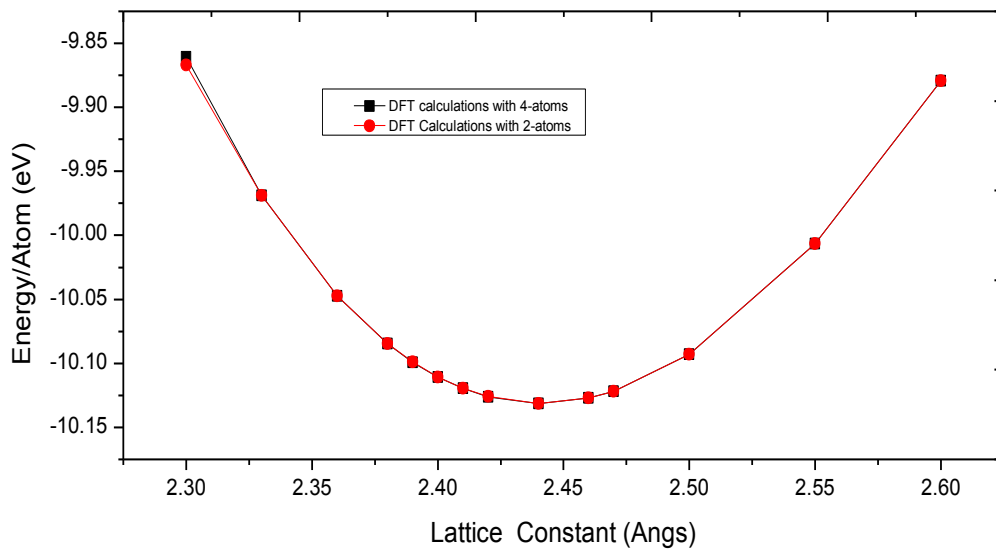


Figure 13: EOS fit for graphene under hydrostatic pressure showing a variation of atomic energy as a function of lattice constant in orthogonal graphene with 2 atoms and 4 atoms using DFT calculations.

Bulk equations of state such as Birch-Murnaghan equation are valid for expansion and compression in a range of  $\pm 10\%$  about the equilibrium volume. To determine bulk modulus, the range of our validity for energy EOS was found by fitting energy versus lattice constant points for graphene in both first principle and atomic simulations. Figure 13 shows the plot from first principle calculations for graphene from two sets of EOS fit parameters of two-atom and four-atom graphene structures. Based on the plot, the EOS fit parameters gave an equilibrium lattice constant  $a = 2.45 \text{ \AA}$ , bulk modulus  $B_o = 322.43 \text{ Gpa}$  force per unit volume and bulk modulus derivative  $B'_o = 4.308$  and a cohesive energy per atom of  $10.131 \text{ eV}$ . The equilibrium volume of  $V_o = 17.40 \text{ \AA}^3$  is obtained using an inter-layer spacing of  $3.35 \text{ \AA}$ , with an equilibrium surface area calculated as  $A_o = 5.194 \text{ \AA}^2$ .

The EOS results in Table 4 show good agreement with experimental and previous theoretical calculations. Although 2 D bulk modulus is commonly computed from uni-axial deformation, there is limited literature on the EOS, as in the case of bulk materials, where this property can be deduced from the relationship between hydrostatic change in surface

area[129]. The bulk modulus is in agreement with the estimated average value for graphite measure by Hanflad et al[153] with their linear Murnaghan EOS.

Table 4: EOS parameters for graphene using first principle and molecular mechanics atomistic simulations

Method	Lattice parameter ( $a_0$ ) Å	Area $A_0(\text{Å}^2)$	Energy (eV)/atom	Bulk Modulus $B_0(\text{nm}^{-1})$	Bulk Modulus derivative $B'_0(\text{dimensionless})$
<b>First Principle Calculation</b>					
Graphene-4atoms	2.449	5.16	-10.13	362.29	4.30
Graphene-2atoms	2.448	5.16	-10.13	358.54	4.30
DFT[129]	2.470	5.27	-15.20	206.6	4.33
Graphite[153]	2.460	5.24			
<b>MM using Inter-atomic potential</b>					
Tersoff	2.529	5.55	-7.39	294.60	4.72
New_Tersoff	2.492	5.37	-7.99	317.61	4.82

Similar to DFT calculated by performing single point energy calculations to understand the effect of hydrostatic change on monolayer graphene. Figure 14 shows the EOS plot from atomistic simulations for graphene using Tersoff, and new-Tersoff. Based on the plots, the equilibrium lattice parameters gives values of approximately 2.52 Å, and 2.49 Å, for Tersoff and New\_Tersoff respectively. These values are within 3%-5% higher than the values obtained from first principle calculations. The bulk modulus determined from the Birch-Murnaghan EOS using New\_Tersoff potential yields a 12% difference from the average value ( $B_0=358.42 \text{ Å}$ ) of DFT calculations for the 4 and 2 atoms graphene structure. Tersoff potential yields a 17% difference compared to the DFT calculations (Table 4). The cohesive energy per atom yields a difference of approximately 20% difference for MM based simulations compared to the DFT calculations 10.131eV.



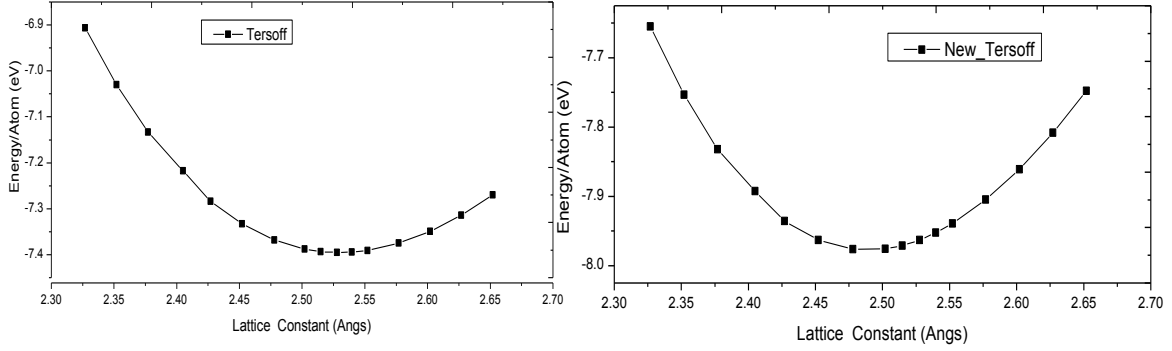


Figure 14: EOS fit for graphene under hydrostatic pressure showing a variation of atomic energy as a function of lattice constant in orthogonal graphene monolayer structure with 128 atoms using molecular mechanics (MM) calculations.

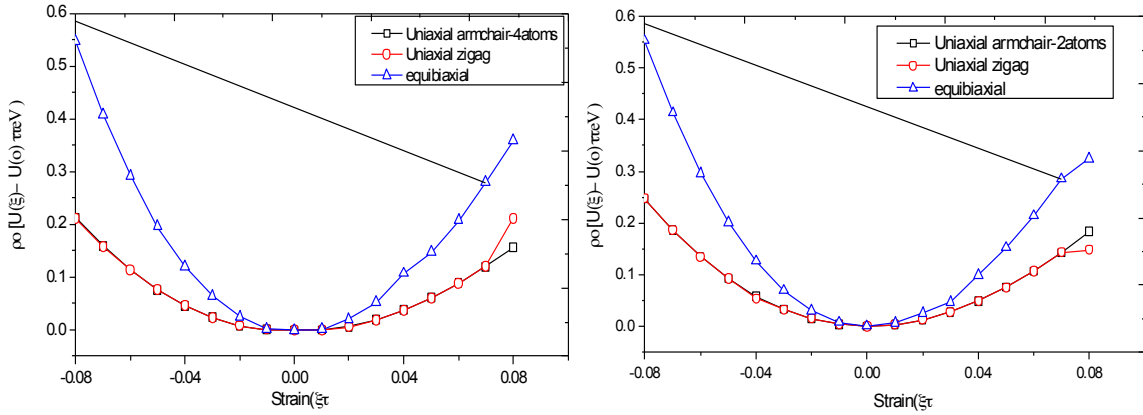


Figure 15: Energy-strain response for uniaxial strain in armchair, zigzag and equibiaxial strain for graphene with (a) 4atoms per unit cell and (b) 2 atoms per unit cell.

#### 4.4.2. Elastic Constants: Second and Third Order

##### 4.4.2.1. DFT Calculations

To obtain the elastic constants of graphene DFT calculations were performed on both the four-atom graphene unit cell and two-atom graphene unit cell. Both the SOEC and TOEC of graphene were obtained by fitting the strain energy to equations 4.19, 4.20 and 4.29. Figure 15, shows the results of first principle calculations of strain energy as a function of strain in the uniaxial armchair, zigzag and equibiaxial deformation. Here we define the strain-energy on a per atom basis. The system energy increases with application of strain, and responds differently at different strain directions.

The calculated results are listed in Table 5, which also list previous calculations for comparison purposes. [129, 154, 155].  $C_{11}$  value is obtained within a 5% difference of comparative studies [154]. The difference may arise from different fits from different coefficients, resulting to an average value being reported. In addition, the VASP package calculates the strain-stress relation for 3D materials, so the elastic constants for 2D graphene, must be multiplied by interlayer spacing of  $10\text{\AA}$ . The strain energy with negative strains are larger compared with the positive strains (Figure 15), as such the values of TOEC are negative. TOEC in strain-energy lessen the stiffness at high tensile strain and lead to an increase in stiffness response at high compressive strains. This behavior is consistent with the non-isotropic structure of monolayer graphene. In all three deformation cases, i.e. armchair, zigzag and equibiaxial, the strain-energies are non-symmetric for compression ( $\xi < 0$ ) and tension ( $\xi > 0$ ).

#### 4.4.2.2. Molecular Mechanics (MM) Simulations

We also calculated the SOEC and TOEC using atomistic simulations, by performing energy minimization with three different inter-atomic potentials, i.e. Tersoff[156], and New\_Tersoff, and force fields. In both uniaxial tensions and compression, a computational cell of graphene lattice is used. Figure 16, shows a plot of strain-energy versus strain for the different potentials. Tersoff and New\_Tersoff potential, in comparison with the first principle calculations, the MM simulations with both Tersoff and New\_Tersoff potential underestimate the stiffness of graphene in the  $C_{11}$  direction by 10%. The accuracy of mechanical properties of graphene using atomistic simulations is limited by empirical potentials.

Table 5: Elastic constants calculated from (a) first principle approach based on density functional theory (DFT) (b) molecular mechanics approach based on inter-atomic potential and (c) experimental values for comparison.

	$C_{11}$	$C_{22}$	$C_{12}$	$C_{33}$	$C_{111}$	$C_{222}$	$C_{112}$	$B_0$ (N/m)	$\nu$
<b>First Principle Calculation</b>									
Graphene-4atoms	323.9	323.9	61.9	131.9	-2571.6	-2543.3	-339	312.06	0.19
Graphene-2atoms	324.6	324.6	61.8	131.1	-2528.7	-2496.1	-340	312.81	0.19
Wei <i>et al</i> [137]	358.1	358.1	60.4	148.9	-2817	-2693	-337	347.9	0.18
Andrew <i>et al</i> [129]	364.6	364.6	67.3	148.7	-	-	-	352.2	0.19
<b>Wang <i>et al</i>[154]</b>	342.0	343.0	64.0	139.5	-2382.0	-2684	-390	330.4	0.19
Bulk graphite[153]	352.7	352.7	58.2	145.9	-	-	-	342.2	0.17
<b>MM using Inter-atomic potential</b>									
Tersoff	287.7	321.4	69.1	109.3	-2379.75	-3057.7	-	272.80	0.22
New_Tersoff	299.20	335.9	61.7	118.8	-2665.26	-3672.7	-	287.80	0.18
Zhou <i>et al</i> (MD)[155]	345.25	-	54.9	144	-	-	-	338.5	0.16
Reddy <i>et al</i> (Brenner)	-	-	-	-	-	-	-	224.12	0.42
Ref MM	-	-	-	-	-	-	-	232.49	0.42
<b>Experimental Values</b>									
<b>Lee [67]</b>	340 ± 40	690	-	-	1.0Tpa	-	-	340	

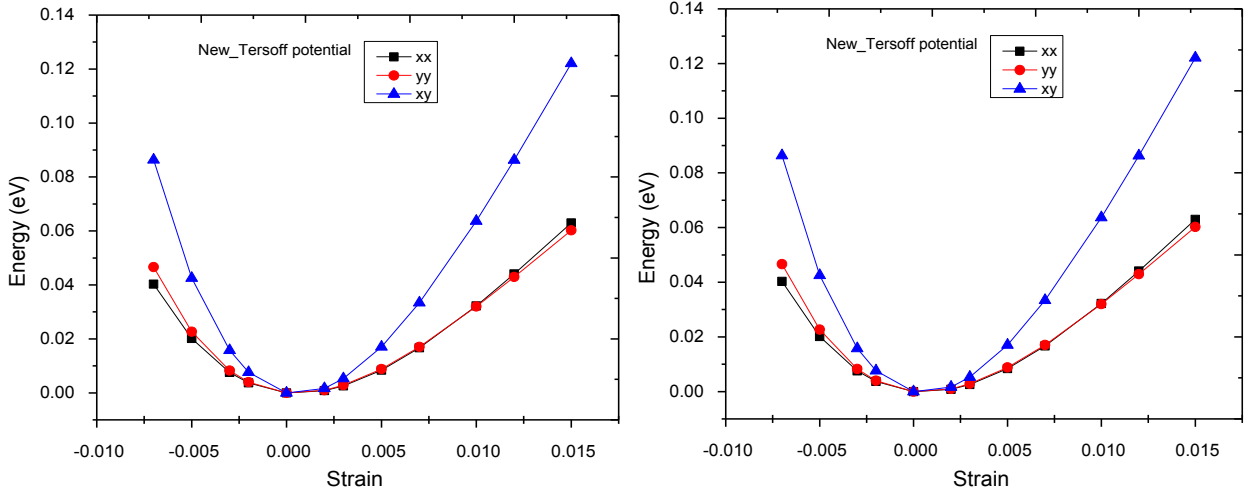


Figure 16: Energy per atom versus strain of graphene monolayer under uniaxial stretch using molecular mechanics approach using (a) New\_Tersoff and (b) Tersoff, potential functions.

#### 4.5. Concluding Remarks

In this work, we have calculated the mechanical properties of 2-D graphene structure using two different approaches; the *ab-initio* calculation using density functional theory and atomistic simulation using molecular mechanics approach. Firstly, we employed the *ab-initio* approach within density functional theory (DFT) to perform total energy calculations on elastic constants on graphene. In order to obtain accurate and comparable results to previously published work we initially determined the total energy convergence of graphene with respect to the energy cutoff and k-point sampling of the Brillouin zone. The energy cutoff was found to be comparable with other studies. Once convergence was successfully achieved, we then proceeded to calculate the elastic properties of monolayer graphene. We compared our results with previous theoretical and experimental results available. Interesting our calculated results is very close to the theoretical and experimental data, leading us to conclude that our structure is plausible.

In addition to *ab-initio* calculation, we calculated elastic constant of monolayer graphene using MM simulations. The general anisotropic, non-linear mechanical behavior of graphene is evident on both approaches. However, the accuracy of the mechanical properties

predicted by this approach is limited by empirical potentials. Both the Tersoff and New\_Tersoff potential used in this study do predict a reasonable value of elastic modulus of graphene.

## 5. THERMAL- MECHANICAL PROPERTIES OF AMORPHOUS POLYURETHANE AND ITS GRAPHENE NANOCOMPOSITE

### 5.1. Motivation

Traditionally, polymeric material have been reinforced with micro-scale fillers such as carbon black, talc and silica carbon fibers[28, 157]. However, as new threats and technologies continue to place stringent demands on the performance of polymeric materials, traditional polymer composites cannot meet these requirements. As a result, new composite materials are being developed using nanoscale materials. At the nanoscale materials synthesis leads to novel insights on the physical properties of materials and present new opportunities for nanocomposite applications. For example, extensive research[11, 16, 20] show effective improvements in material properties obtained at low volume fractions nanofiller compared to micro-scale fillers[158]. The low volume fractions allow composite to retain the tensile strength, ductility, and fracture toughness required in most ballistic applications. Moreover, stiffness and toughness are opposing performance parameters, and a proper balance is required to develop an efficient composite system using nanoscale materials such as graphene[81, 82] and carbon nanotubes[14, 20, 113]. PUR elastomers have intrinsic large strain ability[40], and when reinforced with nanoscale materials, the resulting nanocomposite may be utilized in both civilian and military application[39, 159]. Furthermore, polyurethane exhibits good corrosion resistance and toughness, and imparts fire retardancy which is of significant concern in both civilian and defense applications[29].

Thermal-mechanical properties of materials are studied for the prediction of material behavior in a wide range of parameters, characterizing their internal state, for example temperature and deformations. Changes of state parameters and structural characteristics of a material are due to dissipation of and mechanical interactions of materials with the environment. In polymer the mechanical interactions in a short timescale can cause softening of temperature, additionally this effect is more pronounced at high-strain rates[108]. In order to understand the effect of mechanical interactions under thermal-mechanical behavior, one needs to look at of physical characteristics including density, coefficient of thermal expansion, elastic modulus, yield constants etc. However, with polymer an important challenge is prevalent with the structure and dynamics of these systems, since they are

governed by large spread of length and times scales. The length scale extent from atomic diameter of  $\sim 10^{10}$  m to chain dimensions of approximately  $10^{-7}$  for  $N \sim 10^4$ , additionally, the different is time scale is even larger, ranging from bond vibrations of  $\sim 10^{-13}$  s to slow structural relaxations close to  $\sim 10^2$  s [160].

MD modeling offers a new potential in composite and recent years have seen an increased interest in its use for the study of the structure of graphene [68], and the effect it has as a reinforcement material on polymer matrices [24]. In this work, major emphasis was placed on structural, and dynamic properties of first, the polyurethane matrix and secondly grapheme-polyurethane nanocomposites. Five different polyurethane structures were investigated, varying the number of repeat units (n) ( $[\text{R}'\text{-NH-COO-R}'' ]_n$ ). By varying the number of chain length and number of atoms allows us to streamline the method of producing a feasible modeling polyurethane sample. For the nanocomposite, three types of carbon surface structures were investigated: a pristine graphene sheet plane and graphene plane functionalized with hydrogen and graphene flakes. The approach outlined may find broad applications in understanding thermal-mechanical properties of carbon nanostructures in other hybrid composite systems, including bio-nano-systems, organic polymer composites, and ceramic matrices.

## 5.2. Calculation of Properties

Density of the equilibrated pristine polymer structure is one of the main factors in determining reliability of the molecular dynamics study of any material. Calculation of the equilibrium density gives us confidence over simulations, since they predict properties with the same order of magnitudes.

$$g(r) = \frac{V}{N^2} \langle \sum_i \sum_{i \neq j} \delta(\vec{r} - \vec{r}_{ij}) \rangle \quad (5.1)$$

Radial distribution function (RDF) or pair correlation function ( $g(r)$ ) gives insight into the structure and phase of material i.e. whether the material is in a solid or liquid state. It describes how the atomic density varies as a function of the distance  $r$  from one particular atom in three-dimensional space due to Van der Waal interactions. It is computed using equation 5.1 where  $V$  is the system volume and  $N$  is the number of atoms in the system. The

radial distribution functions between a specific pair of atom types in a structure reveal the correlations between the specific atom types in the structure. In molecular dynamics, the average radial distribution functions over all atom types can be used to determine if the system is amorphous.

The mechanical properties of polymers, mostly the stiffness matrix are an interesting topic for atomic simulations studies [160-162]. This type of simulations studies has been encouraged by theoretical results agreement with the available experimental data. Calculation of mechanical properties requires an evaluation of the second derivative of the potential energy with respect to atom coordinates. This is done analytically because the relationship between atomic coordinates and potential energy is defined by the potential energy function of the force field.

Polymers are considered isotropic, thus we assumed both the polyurethane and nanocomposite models have isotropic material symmetry, hence linear elastic stress-strain relation is applied. Such materials have only 2 independent variables (i.e. elastic constants) in their stiffness and compliance matrices, as opposed to the 21 elastic constants in the general anisotropic case. Thus, under this assumption, the generalized constitutive relation of the equivalent continuum for isotropic material is reduced,

$$\begin{pmatrix} C_{11} & C_{12} & C_{13} & 0 & 0 & 0 \\ C_{12} & C_{22} & C_{23} & 0 & 0 & 0 \\ C_{13} & C_{23} & C_{33} & 0 & 0 & 0 \\ 0 & 0 & 0 & C_{44} & 0 & 0 \\ 0 & 0 & 0 & 0 & C_{55} & 0 \\ 0 & 0 & 0 & 0 & 0 & C_{66} \end{pmatrix}$$

For an isotropic material, the stiffness matrix may be expressed by specifying only two independent coefficients, i.e. the Lamé coefficients,  $\lambda$  and  $\mu$ , and the resulting stiffness matrix can be written as:



$$\begin{pmatrix} \lambda + 2\mu & \lambda & \lambda & 0 & 0 & 0 \\ \lambda & \lambda + 2\mu & C_{23} & 0 & 0 & 0 \\ \lambda & \lambda & \lambda + 2\mu & 0 & 0 & 0 \\ 0 & 0 & 0 & \mu & 0 & 0 \\ 0 & 0 & 0 & 0 & \mu & 0 \\ 0 & 0 & 0 & 0 & 0 & \mu \end{pmatrix}$$

The coefficients of the stiffness matrix are denoted by  $C_{ij}$  and can be related to the Lamé coefficients as:

$$\begin{aligned} C_{11} &= C_{22} = C_{33} = \lambda + 2\mu, \\ C_{44} &= C_{55} = C_{66} = \mu, \\ C_{11} - C_{12} &= 2C_{44}, \end{aligned} \tag{5.2-5.4}$$

The lamé coefficients are required to specify the elastic behavior. Thus, for the isotropic case, the elastic moduli can be written in terms of the Lamé coefficients as follows:

$$E = \mu \left( \frac{3\lambda + 2\mu}{\lambda + \mu} \right), \tag{5.5}$$

$$K = \lambda + \frac{2}{3}\mu, \tag{5.6}$$

$$G = \mu, \tag{5.7}$$

$$\nu = \frac{\lambda}{2(\lambda + \mu)}, \tag{5.8}$$

Where, E is Young's modulus, K the bulk modulus, G shear module and  $\nu$  the Poisson's ratio.

### 5.2.1. Elastic Constants by Molecular Mechanics

When an ensemble of microscopic structures is constructed and mechanical equilibrium achieved, calculation of the elastic constants associated with an amorphous polymer can be performed utilizing several methods[160, 163]. In order to calculate the mechanical properties of the pristine amorphous system for this work, the method of Chen et al. [126] was applied. In this method a unidirectional external load is applied to the cell and the energy of the structure is minimized under constant stress. When a material undergoes deformation, increment in strain is energy. Thus potential energy with respect to strain is calculated as:

$$U(\boldsymbol{\varepsilon}) - U_0(\boldsymbol{\varepsilon}_0) = V_0 \frac{\partial U}{\partial \boldsymbol{\varepsilon}} \boldsymbol{\varepsilon} + \frac{V_0}{2} \frac{\delta^2 U}{\partial \boldsymbol{\varepsilon}^2} \boldsymbol{\varepsilon} + \dots \quad (5.9)$$

Where  $V_0$ , is the initial unreformed cell volume and  $\boldsymbol{\varepsilon}$  are the corresponding components of applied strain of the system and  $U$  is the energy of the system. The elastic constant are calculated from the ratio of applied stress to change in cell size. The first derivative of potential energy with respect to strain is internal stress tensor  $\boldsymbol{\sigma}$ , and second derivative represents stiffness matrix. Consequently by applying the Voigt notation, elastic stiffness matrix is calculated using equation (5.10) below.

$$C_{ij} = \frac{1}{V_0} \frac{\delta^2 U}{\partial \varepsilon_i \partial \varepsilon_j} = \frac{(\sigma_{+i} - \sigma_{-i})}{(\varepsilon_{i+} - \varepsilon_{j-})} i, j = 1, \dots, 6 \quad (5.10)$$

Where  $\varepsilon_{i+}$  and  $\varepsilon_{j-}$  components are the strain tensor,  $\sigma_{+i}$  and  $\sigma_{-i}$  are the component associated with the stress tensor under tension and compressive deformation, respectively.

Small strains were applied to the amorphous polyurethane periodic structure at an energy minimum. Uniformly expanding the dimensions of the simulation cell in the direction of the deformation and re-scaling the new coordinates of the atoms to fit within the new dimensions accomplished the application of strain. The structure was then re-minimized using the conjugate gradient method keeping the lattice parameters fixed, and the resultant stress in the minimized structure was measured. This was repeated for a series of strains ( $\pm 0.01 - \pm 0.06$ ). Therefore applying compressive and tension deformation to the amorphous

polyurethane models measure the variation of strain energy as a function of applied strain. From these variations, a curve of applied strain vs. strain energy is generated and the stiffness matrix is obtained by estimating the parameters of the curve by fitting equation 5.10 at equilibrium volume.

It is important to note that the elastic constants estimated by using the molecular mechanics methods do not include the entropic effects and therefore these constants are regarded elastic constants at 0 K temperatures. As a result, the calculations give an upper estimate of the of the axial, shear and bulk modulus. On the contrary, entropic effects are included in the dynamics method, and in the next section we briefly explain this method.

### 5.2.2. Elastic Constants by Molecular Dynamics

An alternative approach to calculate the elastic properties of material system is using constant stress molecular dynamics method. In this method, subjecting the material to an external stress and measuring the corresponding strains in a NPT ensemble calculate elastic constants. In this approach there is no volume constrain, thus the size and shape of the simulation cell is allowed to vary, making it possible for the microstructure to adjust the imbalances between an externally applied pressure and internally measured pressure tensor. The change in pressure is obtained by changing the coordinates of the atoms. The pressure imbalance is coupled to the first derivative of the basis vectors. The first derivative gives the pressure tensor; the second derivative produces averages of fluctuation of pressure tensor components. These so-called fluctuation terms arise from the changes in the relative probability of the system's states brought about by the deformation itself. This kind of coupling reduces the tendency to unphysical oscillatory response: in fact the motions of the cell are over damped.

In this approach, uniform stress is applied in all three directions, i.e. x, y and z directions to simulate the bulk behavior of the polyurethane models. An external stress was applied, isotropically in an NPT ensemble from 0 to 2000 atmospheres in increments of 500atm. The structure was then relaxed for 200ps. This was repeated for each external pressure and the volume fluctuations obtained. By applying a uniform external load to the amorphous polyurethane models, the variation of external load vs. volume is obtained; from

this variation one can plot a graph of pressure vs. volume. From this plot, the bulk modulus is calculated as follows:

$$K = -V \frac{\delta P}{\delta V} \quad (5.11)$$

where  $V$ , is the equilibrium volume at room pressure.

### 5.3. Computational Details

Formulation of molecular level simulations problem involves specification of three aspects (a) molecular model consisting of atoms, functional groups and/or molecules (b) a set of potential/force field functions (c) computational methods to be used in the simulations. The polyurethane models were constructed using Material Studio 6.0, a molecular modeling software package by Accelrys[32]. The subsequent molecular dynamics simulations were performed with the large-scale atomic/molecular massively parallel simulator (LAMMPS) package [31].

#### 5.3.1. Generation of Amorphous Polymer Models

Different configurations of polyurethane chains generated starting from the repeat unit in Figure 17, using the build polymer tool of the Material Studio. The chains are based on the atactic tacticity, which places the substituent's randomly along the carbon backbone chain. Head-to-tail connectivity of the monomers is assumed for all polyurethane models. The number of repeat units ( $n$ ) is selected so as to look at the different effects of chain length and different number of chains to understand the effect of size and chain length on the bulk properties. The charges of the isolated polyurethane chains are calculated based on the charge equilibration method ( $Q_{eq}$ ) [113]. The  $Q_{eq}$  method is widely used to predict charges for any polymer, ceramic, or biological system amongst others. The calculation of the charges of the isolated chains minimizes the computational cost, compared to evaluating the charges of the periodic system, which can be computational intensive.

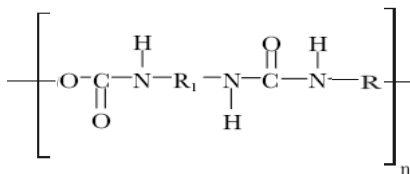


Figure 17: Monomer of polyurethane matrix (a) schematic (b) material studio model

Table 6: Characteristic of computational models polyurethane systems

Polyurethane (models)	repeat units (n)	No. of chains(m)	No. of atoms	Dimension of the model(Å) a=b=c	Mass g (10 <sup>-20</sup> )
PUR-1	[R'-NH-COO-R''] <sub>10</sub>	20	8040	45.68	8.59
PUR-2	[R'-NH-COO-R''] <sub>20</sub>	10	8020	45.68	8.58
PUR-3	[R'-NH-COO-R''] <sub>40</sub>	5	8010	45.68	8.58
PUR-4	[R'-NH-COO-R''] <sub>20</sub>	5	4010	36.26	4.29
PUR-5	[R'-NH-COO-R''] <sub>20</sub>	20	16040	57.56	17.2
	R'=[CH <sub>2</sub> ] <sub>4</sub>	R''=[CH <sub>2</sub> ] <sub>6</sub>			

To estimate the density of the material for an infinite chain length, different amorphous polyurethane models were placed in a cubic periodic box using the Amorphous Cell module of the Material Studio suite of software with increasing chain lengths ( $[(C_{12}H_{24}N_2O_4)]_n$  with  $n = 10, 20, 30$  and  $40$ ). Each of the cubic bulk models consist of 4000, 8000 and 16000 atoms, with different number of end hydrogen groups, and dimensions of about 36Å, 46Å and 57Å, respectively. The main features of the polyurethane molecular models are shown in Table 6. The periodic box is used to create boundary conditions that alleviate surface effects and allows simulating processes in a small part of a bulk system, which allows us to estimate the bulk properties the system. After developing the polyurethane molecular structures, we simultaneously defined the potential energy functions using the Dreiding[124] potential parameters. The method force field is described in detail in the previous section with the functional form of the force field shown in Table 3, and parameters described in detail in appendix.

When developing any amorphous polymer molecular models, two issues have to be taken into considerations. First is the time factor,[126] building of bulk polymers can be time consuming, therefore it is important to choose a building scheme so that the final structure is as correct as possible and built within a reasonable time. Second is the wide range of spatial conformations available to the polymer chains[125]. These different considerations were controlled to some degree via two most important parameters affecting the sample configuration, these include, the backbone dihedral angles which determines the orientation of different bonds with respect to each other, and the initial density which determines the chain packing in the unit cell.

To overcome these issues, first, we used the widely used approach of Fan et al[126]. This approach assigns the backbone dihedrals via Monte Carlo method, which allows the orientation of different bonds thus resulting in the generation of the polymer chains randomly. Second, the density of a model depends greatly on how it was constructed as well as on the further simulation treatment. It is much easier to construct a perfectly crystalline structure at its maximum density, however for amorphous bulk polymers it is necessary to build a model at low starting density, then use energy minimization or molecular dynamics to obtain a target density[112]. The low starting density not only determines the chain packing in the unit cell, but also mitigates the self-avoidance failure [125, 126]. Ideally the density of the final structure should match experimental values and be independent of their initial densities. The amorphous polyurethane bulk models were generated at very low initial density of  $0.35 \text{ g/cm}^3$ .

In MD, one solves the equation of motions for many body systems to obtain the phase space trajectories of the system, and then the physical properties such as energy, pressure, stress, etc can be calculated as time averages over trajectory. Any MD “run” contains two phases, equilibration and production. Equilibration phase allows the molecular structure to obtain the desired thermodynamic state, while the production phase enables one to calculate thermodynamic parameters: specific heat, thermal expansion, elastic moduli over a specified period of time

Equilibration phase is the first step in establishing the bulk properties for a pristine or nanocomposite material in MD is to obtain an equilibrated state. In MD, attainment of the equilibrated state necessitates the fulfillment of two major criteria i.e., to achieve energy

stabilized at a prescribed temperature, and to obtain the minimum initial stress state for the periodic boundary box. To achieve these criteria, all amorphous polyurethane models were subjected to an energy minimization and NVT dynamic simulations with temperature-annealing cycle consecutively. Temperature annealing cycle involves a periodic increase in temperature from 100K to 700K allowing the minimization of energy gradually without trapping the structure in a meta-stable, high-energy but “local” minimum. We increased the density gradually by reducing the lattice parameter of the unit cell but keeping the axis ( $\alpha=\beta=\gamma=90$ ) orthogonal to each other. In the second step, the unit cell was adjusted to minimize the initial stresses using isothermal-isobaric (NPT) ensembles for 500ps for all the amorphous polyurethane models. The NPT dynamics allows for the relaxation of the cell parameters and angles in order to obtain a final reasonable equilibrated structure. Once we obtained an equilibrated model, polymer densities for all the models were calculated. Calculation of the equilibrium density gives us confidence over simulations, since they predict the properties the properties with the same order of magnitudes.

Production phase is the second in establishing the bulk properties of a material. After obtaining an equilibrated amorphous polyurethane microscopic structure, calculation of the thermodynamic parameters: specific heat, thermal expansion, elastic moduli over a specified period of time can be performed utilizing several different methods. In the production phase, one relates the macroscopic properties to the microscopic state of a system. In the following section, we provide a brief overview of all the structure and thermodynamic properties observed at the production phase of our MD simulations.

### 5.3.2. Graphene Structure

We constructed a pristine graphene structure from a graphite unit cell with lattice parameters  $a = 4.26\text{\AA}$ ,  $a = 2.46\text{\AA}$ ,  $c = 3.4\text{\AA}$ , and  $\alpha = \beta = \gamma = 90^\circ$ , making sure all atomic bonds were formed across the cell boundaries. The unit cell was then replicated to cell dimension of  $a = 41.8\text{\AA}$ ,  $a = 42.6\text{\AA}$ ,  $c = 42.6\text{\AA}$ , the keeping the lattice angles orthogonal to match the equilibrated lattice parameters of the already calculated polyurethane model, presented in the previous section. The pristine graphene is constructed of 680 carbon atoms. Additionally, we constructed functionalized graphene sheets with hydroxyl groups and

hydrogen from the pristine structure. Figure 1.2, shows display of Material Studio constructed atomic models of pristine graphene, and functionalized with hydrogen (H).

### 5.3.3. Graphene-polyurethane Nanocomposite Structure

The graphene ( $C_{240}$ ), ( $C_{680}$ ), and ( $C_{620}H_{70}$ ) structures considered for this work as mention before were bulk supercell with dimensions  $a = 41.8 \text{ \AA}$ ,  $b = 42.60 \text{ \AA}$ , and  $c = 42.60 \text{ \AA}$ . The approach implemented to develop the nanocomposite was a modified version of building amorphous polymer samples[162]. Consequently a polymer sample with an initial low density using the amorphous module in Material Studio, with the initial lattice parameters set to the values of  $a = 41.8 \text{ \AA}$ ,  $b = 42.60 \text{ \AA}$ , to match that of the graphene structures. Both the graphene and polyurethane models were geometrically minimized separately before constructing the nanocomposite. We utilized the Build Layer option in Material Studio to develop the polyurethane-graphene nanocomposite. In this process, a large vacuum space of  $30 \text{ \AA}$ , was added above the polymer to minimize the interaction forces between the graphene and polyurethane. The matching lattice parameter of the graphene structures was imposed on the polyurethane. Thus the final graphene-polyurethane nanocomposite constructed from the Build Layer option in Material Studio program has lattice parameters with dimensions  $a = 41.8$ ,  $b = 42.60$ , and  $c = 95.448 \text{ \AA}$

After the construction of the nanocomposite, the equilibration procedure similar the pristine polyurethane model was applied to the nanocomposite. However, the process was adjusted slightly to treat the graphene as a rigid structure in and canonical ensemble (Constant number of atoms, volume and temperature) (NVT)) anneal dynamics and minimization cycles, while adjusting the cell dimension in the z-direction. The rationale behind this is to relax the chains of the polymer structure to an equilibrated structure without changing the graphene structure.

This is important in terms of conserving the computational resources. In addition, the process helps to preserve the already minimized graphene structure as opposed to allowing the graphene atoms to explore the available abundant space around the low-density PUR structure resulting in a distorted graphene structure for no physical reason. In all the nanocomposite systems, i.e., PUR with  $C_{680}$ , and  $C_{620}H_{70}$  the excluded volume due to van der



Waals distance between the GNS and PUR was accounted for during this adjustment of the density.

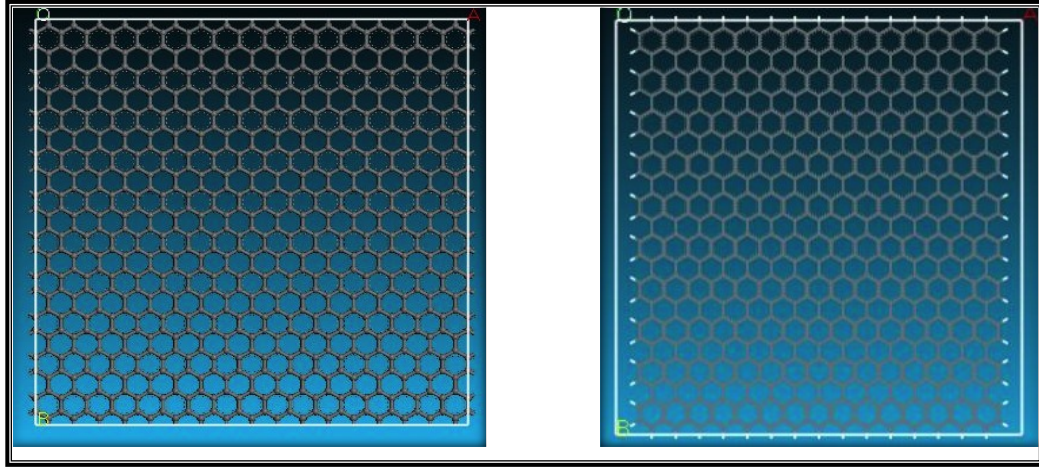


Figure 18: Atomic model for (a) pristine graphene (C680) (b) pristine graphene with hydrogen end groups G(H)-(C620H70).

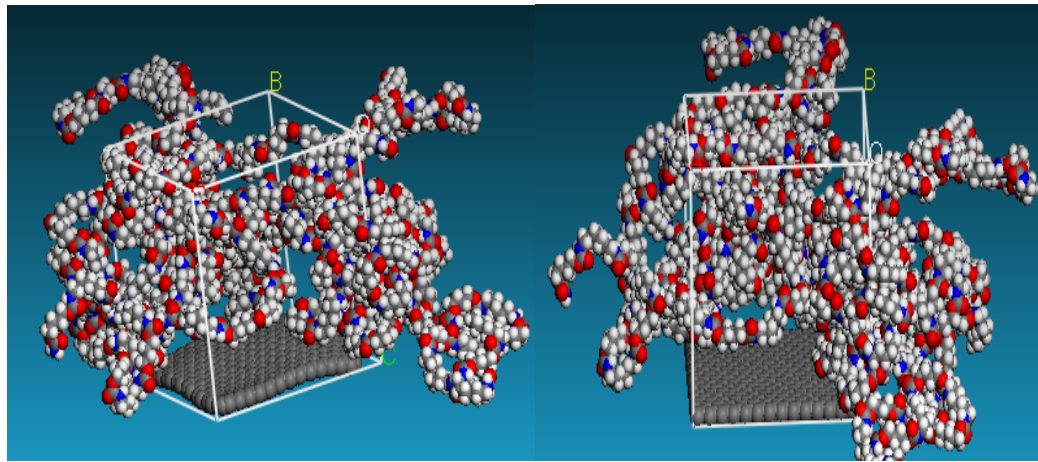


Figure 19: Snapshot of Gr-PUR nanocomposite structure with graphene at the bottom of simulations cell; (right) snapshot of Gr-PUR nanocomposite with graphene flakes at the bottom of the bottom of the simulations cell.

To obtain a structure for comparison with the equilibrated model of the pristine polymer, the graphene atoms were constrained in such a way that the compression-energy minimization-anneal dynamic cycle applied in the z direction had no effect on bulk structure. Thus the non-constrained part of the bulk structure, i.e. the polymer was compressed to a somewhat higher density of 1.3g/cc that the estimated experimental values. Nevertheless, the initial low-density polymer sample in nanocomposite went through the same approach of the

equilibrated model polyurethane models. The resulting structure was allowed to relax at in an isobaric-isothermal (NPT) ensemble at temperature of 300K and pressure of 1.0atm for duration of 0.5ns with a time step used of 1 femtosecond (fs) to attain an accurate and stable structure before calculating the mechanical properties of the system.

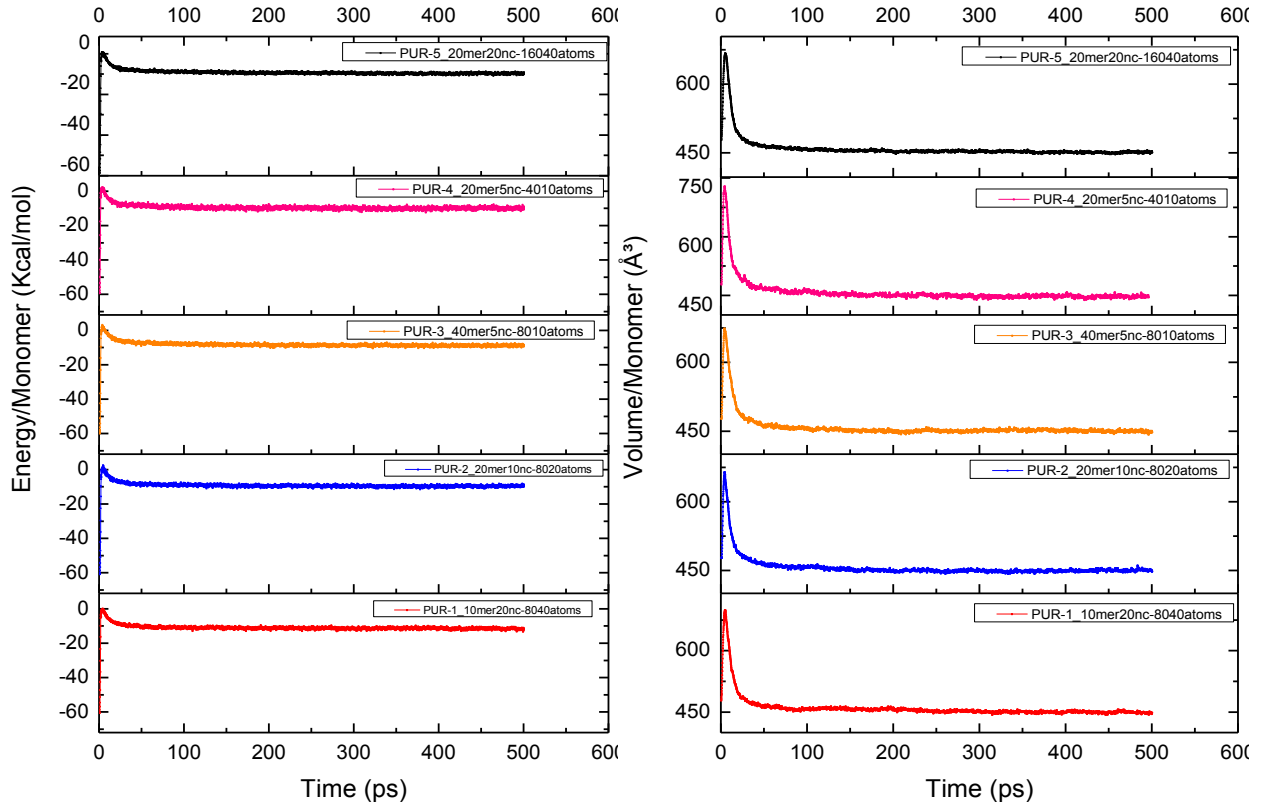


Figure 20: Volume (a) and total energy (b) evolution during the equilibration of the individual polyurethane samples (PUR-1–PUR-5) at 300K and 1atm.

The optimized Dreiding potential was used for all simulations. The van der Waals interactions were treated with a cutoff distance of 12.5 nm, and the Long-range electrostatic interactions were treated using the particle-particle-particle-mesh Ewald (PPPM) summation method[120]. A Nose-Hoover thermostat with a temperature-damping constant of 100fs was used to maintain the constant temperature of the simulation cell. In this work, the weight percent of the pristine graphene is calculated is varied in two samples of 13.65wt % and 15.28 wt%. As an initial step we used the PUR-1 sample as described in the polymer section. We observed the same properties in the pristine polymer sample, in both the equilibration

and productions runs. These properties are discussed in detail in the next section and are also compared with properties obtained for the pristine polyurethane model.

#### 5.4. Results and Discussion

Data analysis from MD simulations involves two stages. (1) Equilibration and (2) productions run. In the equilibration stage, NPT-MD simulations were carried out for 500ps at room temperature and pressure. This stage is necessary to generate a profile of various first-order thermodynamics properties such as energy, pressure and temperature, versus time. These quantities should fluctuate around their average and remaining constant over time, thus confirming the most stable configuration with minimum initial stress of the molecular structure. Figure 2 and 3 shows the volume and total energy of the individual the polyurethane models and the combined for all the models respectively. The profile of instantaneous values of energy and volume were used to decide the cutoff between equilibration and production runs (Figure 20). We observe all the samples are equilibrated at  $\sim 50$ ps. Since there are no fluctuations after 50ps, this provides ample confidence in the properties estimated from the corresponding production run.

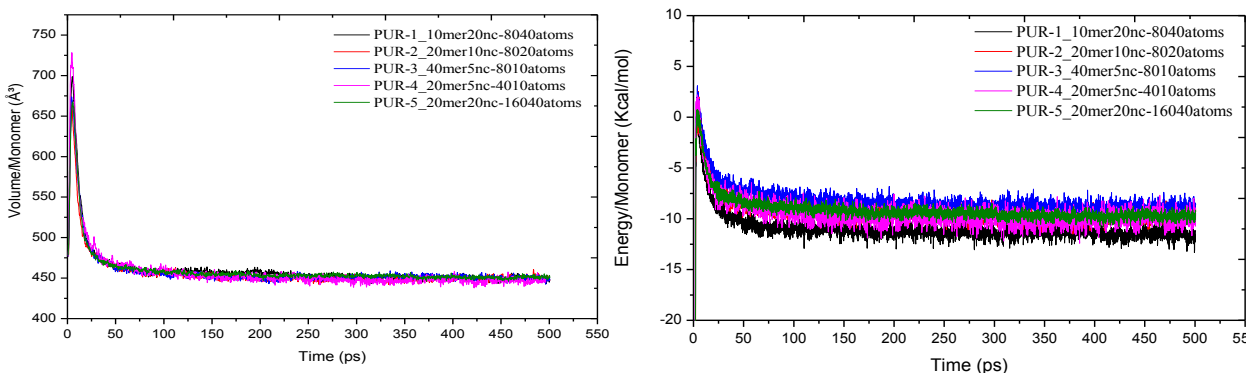


Figure 21: Combined volume (a) and total energy (b) evolution during the equilibration of the initial polyurethane sample at 300K and 1atm.

The initial and final densities for each polyurethane sample are listed in Table 7. Ideally, the densities of the final structure should match the experimental values and be independent of their initial densities. At the end of the equilibrations, the density of the polyurethane samples stabilized at an average density of 0.95 g/cc with a standard deviation

of 0.014 g/cc. It is important to note that the density observed from the equilibration phase, may differ from experimental data (1.00-1.12g/cc)[164] for polyurethane because simulations deal with material free from mechanical defects and impurities. In addition, simulations are also affected by the difference in the overall chain conformations of each sample, as well as the accuracy of the parameterization in the force field. Charge equilibration may also introduce errors. Additionally, a comparison of the potential energies of each sample listed in Table 7 indicates similar values, which illustrates effectiveness of the generation of amorphous polyurethane model procedure.

Additionally, for the nanocomposite, Figure 22 shows the density versus time plots of the pristine polyurethane and graphene based nanocomposite based on 14wt% graphene, 17wt% graphene nanosheets and 13wt% graphene flakes. The graphs are obtained after performing NPT-MD simulations at 300K for final equilibrated structures. On average nanocomposite takes a few nanoseconds of MD simulations to equilibrate.

Table 7: Initial density, final density and potential energies of polyurethane samples

Polyurethane Models	Initial density (g/cm <sup>3</sup> )	Final density (g/cm <sup>3</sup> )	Potential Energy Kcal/mol/monomer
PUR-1	1.24	0.94	10.99
PUR-2	1.24	0.95	9.30
PUR-3	1.24	0.95	8.75
PUR-4	1.24	0.97	9.97
PUR-5	1.22	0.95	9.62
Average	-	0.95	9.72
Std deviation	-	0.014	0.83
Experimental [28, 164, 165]	<b>1.00-1.2</b>		

The average densities of the equilibrated structures samples are tabulated in Table 8. There is an increase in density with the graphene nanosheets compared to the polyurethane and the graphene flakes nanocomposites. This is due to formation of aggregates producing a

very low-bulk density. The results suggest that graphene need to be exfoliated in the form of graphene sheets and uniformly dispersed into a matrix system.

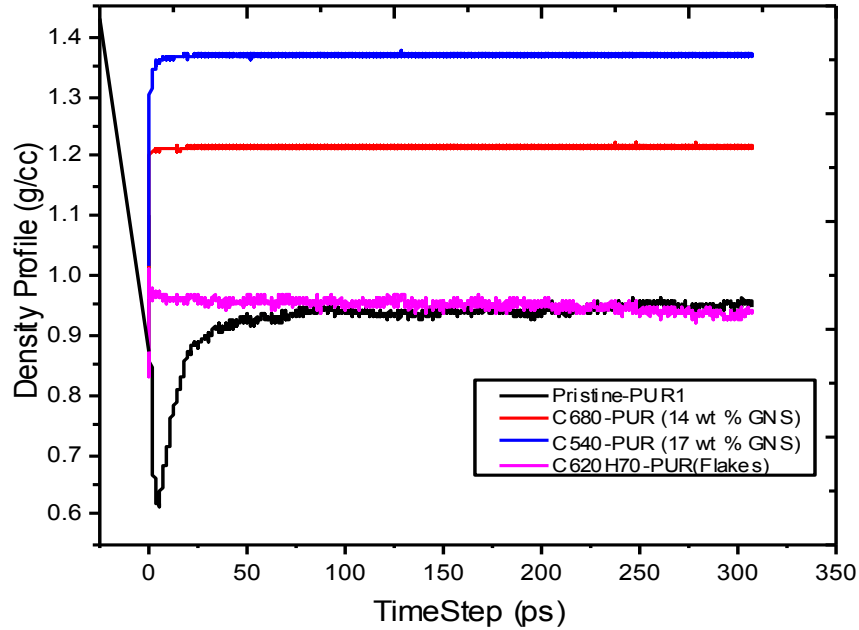


Figure 22: Density vs. time plots of (a) pristine polyurethane, (b) nanocomposites of 14wt% and 17wt% of graphene nanosheet in polyurethane, and (c) 13wt% of graphene flakes in polyurethane

Table 8: Bulk densities of polyurethane in pristine PUR and in nanocomposite.

System	Model	Density, (g/cm <sup>3</sup> )
Neat Polymer (Average)	PUR-I	0.95
Nanocomposite	C <sub>680</sub> -PUR (14 wt % GNS)	1.23
	C <sub>540</sub> -PUR (17 wt % GNS)	1.34
	C <sub>240</sub> -PUR (graphene flakes)	0.96

The amorphous nature of simulated polyurethane structures is determined by calculating the pair distribution function. A complete set of all pair distribution functions is essential in order to completely characterize the correlations corresponding to different types of atoms. However, for amorphous materials, analysis of pair correlations between atom pairs is determined by examining the total pair distribution functions  $g(r)$ .

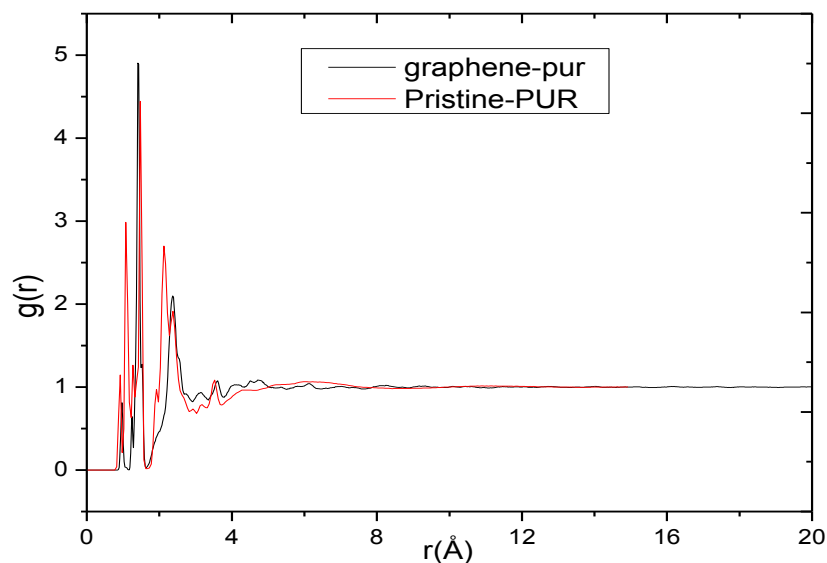


Figure 23: RDF of entire system for pristine PUR and graphene nanocomposite.

The  $g(r)$  for the amorphous polyurethane models is plotted vs. distance ( $r$ ) in Figure 24(a). No long range order is observed at distances greater than  $5\text{\AA}$ . This means that beyond this point the structural order due to intermolecular connections disappears and structures are completely randomized as far as the nearest neighbor atom positions are concerned. This is clearly defined in our plot that shows no peaks at distances greater than  $5\text{\AA}$  indicating an absence of long-range order, which is a defining characteristic of the atomic arrangement in amorphous system. In Figure 23, we plot the radial distribution function of a pristine polyurethane model and its graphene composite. The RDF is expected to be of similar pattern in the entire graphene-polyurethane nanocomposite as well as the polyurethane models, which is clearly observe in Figure 23.

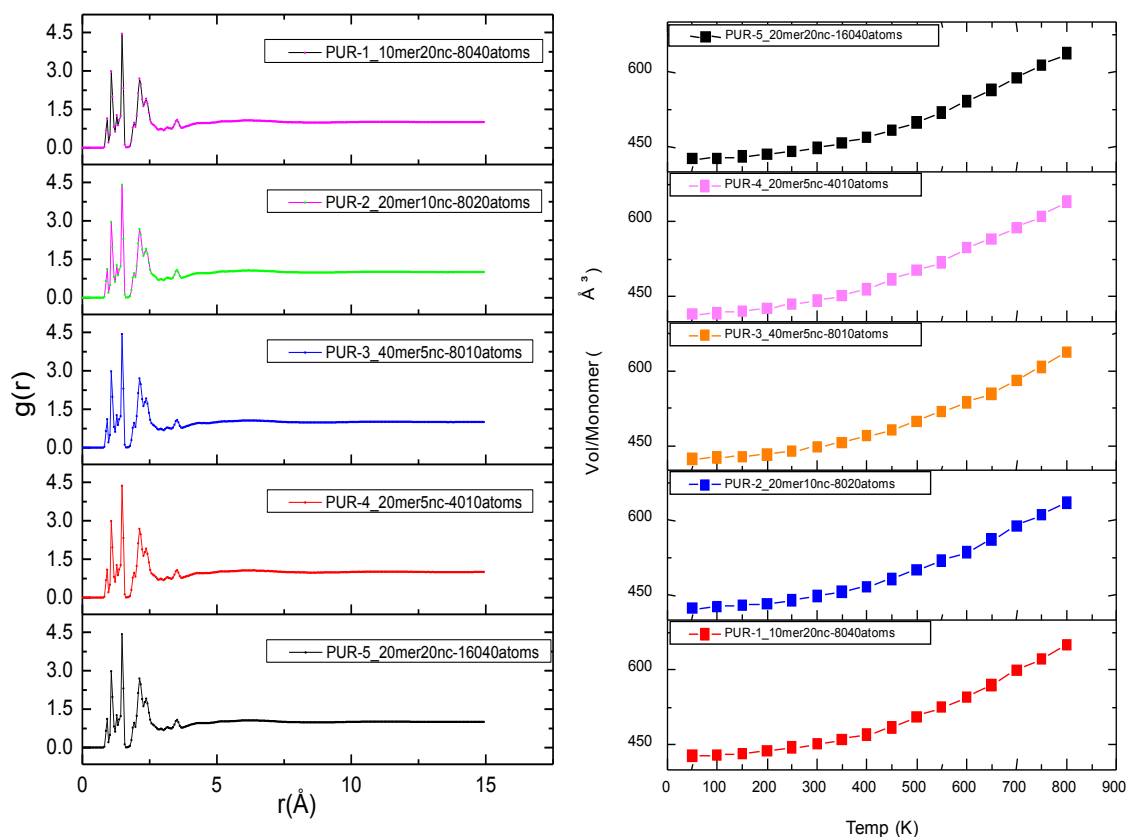


Figure 24: Graphs of (a) average RDF for the equilibrated polyurethane models (b) the V-T curves at 1atm from NPT dynamics, the arrow locates the position of the  $T_g$  as determined from the MD simulations.

#### 5.4.1. Volume Dependence on Temperature

To study the temperature dependence on thermodynamic quantities, we performed an NPT-MD simulation in the temperatures range of 50 - 700K at 1atm in 50K increments on the pristine PUR, PUR-graphene sheet and PUR-graphene flakes model at temperature range 100K-700K. The duration of each dynamic run was 200ps with an integration time step of 1 femto-second. In Figure 24(b), we plot the average volume as a function for the amorphous polyurethane models. The distinct discontinuity in the slope represents the location of the  $T_g$ . Our simulation results reveal a  $T_g$  which occurs in the range of 285-305°C, for pristine polyurethane models, which is within the experimentally determined range of 223-323°C[27, 164].

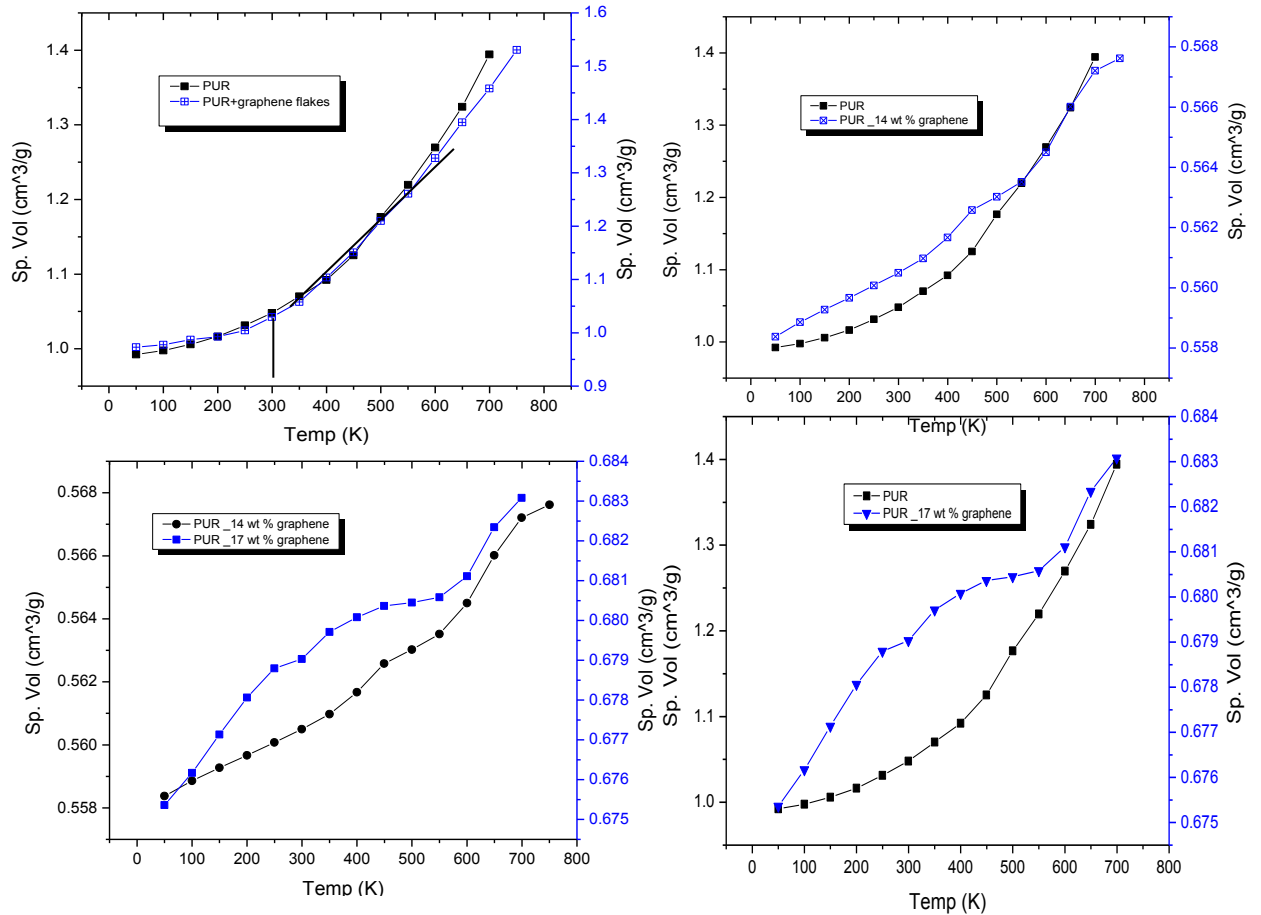


Figure 25: Specific volume vs temperature for (a) PUR vs. PUR+ graphene flakes, (b) PUR vs. PUR with 14wt%graphene sheet (c) comparison of PUR nanocomposite with 14wt% and 17wt<sup>0</sup> graphene (d) comparison of PUR and PUR with 17wt<sup>0</sup> graphene.

Figure 25, displays specific volume as a function of temperature for the amorphous polyurethane, and its different graphene nanocomposites. The glass transition is identified from the discontinuity in the curves. For shows a graphene for the nanocomposite samples 350K for the graphene sheet and around 275K for the graphene flakes nanocomposites. There is an increase of 25K with the graphene sheet and decrease of 50K with the graphene flake. Experimentally, T<sub>g</sub> of polyurethane has been reported to range between 223K and 323K. The V–T results are important for two reasons; first, the results, when compared to experimental data, provide a means of determining the quality of the force-field parameters used in the simulations, and second, it allows for a direct prediction of the volumetric glass transition temperature (T<sub>g</sub>). T<sub>g</sub> is of fundamental importance in determining the material properties of the polymer. Comparing this diagram with experimentally determined volume



versus temperature curves generally observed for amorphous materials, it is apparent that the molecular dynamics simulations are successful in producing a glass transition.

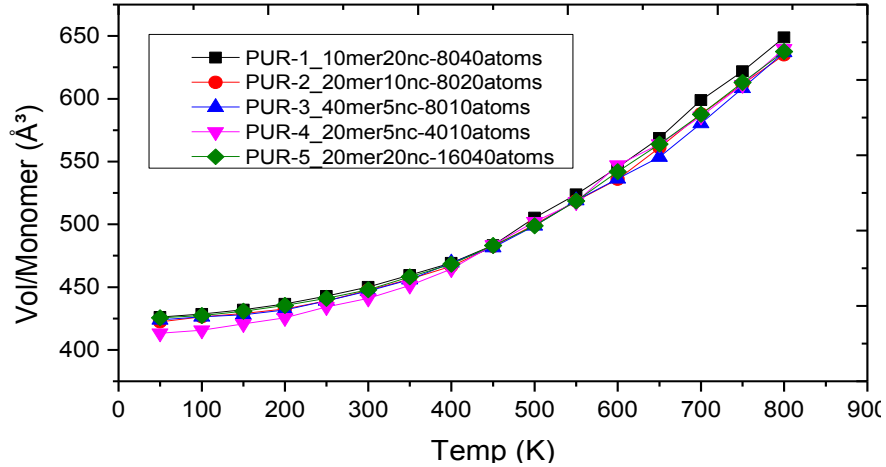


Figure 26: Temperature vs. volume of simulates samples of amorphous polyurethane models.

Figure 26, indicated a combined V-T graph of five different polyurethane samples. From the V-T curve we calculated the average volumetric coefficient of thermal expansion ( $\alpha_p$ ) evaluated from the slope above and below  $T_g$ , to be between  $1.93 \times 10^{-4}$  -  $1.98 \times 10^{-4}$  and  $5.79 \times 10^{-4}$  -  $6.91 \times 10^{-4}$  Kcal/MolK, respectively for PUR-I to PUR-5. The combined average of this values, give a coefficient of thermal expansion  $4.05 \times 10^{-4}$  Kcal/MolK with a standard deviation of  $\pm 2.05 \times 10^{-5}$  Kcal/MolK. Compared to the experimental value of  $3.15 \times 10^{-4}$  Kcal/MolK for polyurethane reported in literature, the simulations results are in excellent agreement with experiment and demonstrate the accuracy of Dreiding force-field parameter set used for simulation of polyurethane models.

Additionally, we calculated the coefficient of thermal explanation above and below  $T_g$ , tabulated in Table 9. From our calculation, we can infer that there is a decrease of 87% and 63% in the coefficient of thermal expansion above and below  $T_g$  respectively for the polyurethane reinforced with the graphene sheet. While there is an increase of 60% and 25% in the coefficient of thermal explanation above and below  $T_g$  for the polyurethane reinforced with graphene flakes. This significant difference between the graphene sheet and graphene flakes is attributed to lack of surface effects in the graphene sheet compared to the graphene

flakes, causing the flakes to form aggregates which limits the contact surface afforded in graphene sheets and reducing its effects on improving the properties.

Table 9: Calculation from glass transition temperature ( $T_g$ ), coefficient of thermal expansion above and below  $T_g$ , Specific heat ( $C_p$ ), Isothermal compressibility ( $KT$ ) and bulk modulus ( $K$ ) from atomistic simulations

Model #	$T_g$ /K	$\alpha_p$ below $T_g/K^{-1}$	$\alpha_p$ Above $T_g/K^{-1}$	$C_p$ (Kcal/mol-K)	Bulk modulus (K) Gpa
PUR-I	325	$1.93 \times 10^{-4}$	$5.79 \times 10^{-4}$	31.24	2.24
Gr-PUR-I	350	$2.60 \times 10^{-5}$	$2.13 \times 10^{-4}$	28.52	66.36
Gr-flake –PUR 1	275	$3.09 \times 10^{-4}$	$7.21 \times 10^{-4}$	34.49	1.07
<b>Experimental</b>	<b>223-323</b>	<b><math>3.15 \times 10^{-4}</math></b>			

Table 10: Elastic constants of amorphous polyurethane calculated by molecular mechanic approach:  $C_{11}$ - $C_{23}$  are elastic constants in Gpa, bulk modulus (B), young modulus (Y), shear modulus (G) in Gpa and Poisson's ratio  $\nu$ .

Model	Atoms	$C_{11}$	$C_{22}$	$C_{33}$	$C_{12}$	$C_{13}$	$C_{23}$	B	Y	G	N
PUR-I	8040	7.83	7.95	7.64	2.95	2.59	2.76	4.57	6.22	2.44	0.27
PUR-2	8020	8.26	7.76	9.80	2.95	2.86	2.84	4.72	6.70	2.66	0.26
PUR-3	8010	7.85	7.72	8.20	2.85	3.31	3.83	4.52	6.27	2.50	0.27
PUR-4	4010	8.03	7.16	7.07	2.26	2.80	2.70	4.18	7.03	2.89	0.22
PUR-5	16040	7.71	7.72	7.79	3.07	3.18	3.31	4.62	5.96	2.32	0.28
Average	-	7.94	7.66	8.10	2.82	2.95	3.01	4.52	6.44	2.52	0.26
Std. Dev $\pm$	-	0.21	0.30	1.03	0.32	0.30	0.48	0.20	0.42	0.22	0.02

#### 5.4.2. Evaluation Mechanical Properties

We estimated the mechanical properties of the polyurethane models using the molecular mechanics and molecular dynamics methods. In molecular mechanics approach the system was deformed by tensile, compression, and shear deformations of magnitude  $\pm$

0.01 and after each deformation the system was re-minimized using the conjugate gradient method. In this method, after applying the deformation, the structure does not settle to a unique global minimum, but rather on one of the many local minima. As such the strain energy being slightly dependent on the deformation path leads to the non-symmetric nature of the stiffness matrix.

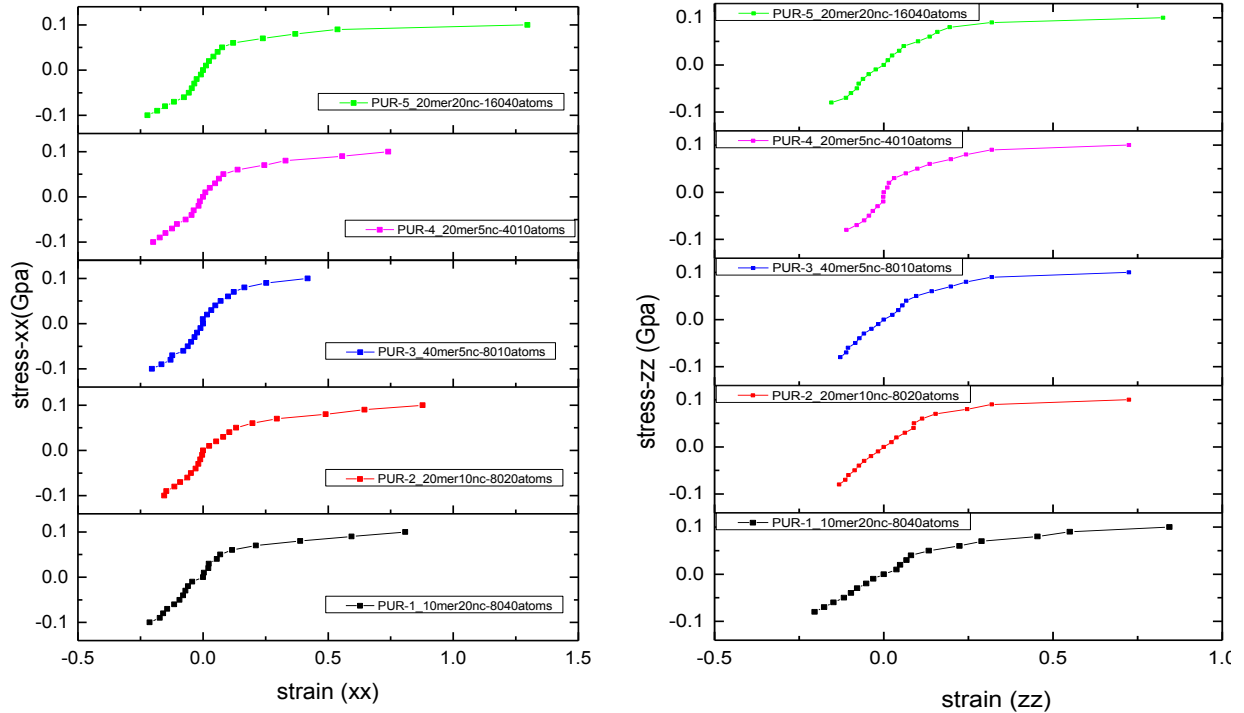


Figure 27: Comparing amorphous polyurethane models in terms of uniaxial deformation in  $xx$  and  $zz$  using molecular dynamics simulation in NPT ensemble at 300K.

The Young's modulus ( $Y$ ), bulk modulus ( $B$ ), the Poisson's ratio and shear modulus ( $G$ ) derived from the stiffness matrix are listed in Table 10. The calculated values are twice as high compared to those obtained experimentally (6.44Gpa vs. 1.69Gpa for the Young modulus, and 2.52 Gpa vs. 0.592Gpa for shear modulus)[108]. As discussed previously, one reason for this discrepancy is due to the ideal nature of the simulated systems, while the experimental samples, which may contain impurities or defects during preparation of even handling, proper storage amongst other factors. As such, one would therefore expect simulations to obtain higher results compared to experiments. Furthermore minimizing internal energy and neglecting entropic effects we obtain stiffness constants. Consequently, the temperature difference between 0K and room temperature may also play a vital role.

Subsequently, these calculations show an upper estimate of the axial moduli of the sample. However, observing the average values of the stiffness matrix for the polyurethane models in Table 10, one can deduce the basic feature of an isotropic material.

In MD approach, the equilibrated polyurethanes models were subjected to a uniform tensile and compressive stress along the  $x, y, \text{ and } z$  directions from for 0 to 2000 atmospheres in increments of 100 atmospheres in the compressive and tensile nature. After each external stress, the polyurethane models were allowed to relax for 200ps and the stress value increased, which translated to a stress rate of  $5 \times 10^7 \text{ Gpa} / \text{sec}$ . The stress-strain data for each of the six samples were averaged for all three directions, and the moduli calculated from the region showing linear response in average stress versus strain graphs shown in Figure 23.

Table 11: Elastic constants of amorphous polyurethane calculated by molecular dynamics approach, modulus in Gpa

Model	Atoms	Bulk Modulus	Young Modulus	Shear Modulus	Poisson's ratio
PUR-I	8040	$0.76 \pm 0.26$	$0.61 \pm 0.16$	$0.23 \pm 0.06$	$0.35 \pm 0.01$
PUR-2	8020	$0.56 \pm 0.20$	$0.52 \pm 0.04$	$0.20 \pm 0.02$	$0.35 \pm 0.07$
PUR-3	8010	$1.03 \pm 0.09$	$0.64 \pm 0.08$	$0.27 \pm 0.01$	$0.38 \pm 0.02$
PUR-4	4010	$1.58 \pm 0.29$	$0.96 \pm 0.23$	$0.34 \pm 0.08$	$0.39 \pm 0.04$
PUR-5	16040	$1.16 \pm 0.27$	$0.64 \pm 0.11$	$0.23 \pm 0.03$	$0.40 \pm 0.01$
Average	-	$1.02 \pm 0.35$	$0.67 \pm 0.15$	$0.25 \pm 0.04$	$0.37 \pm 0.02$
**Martienssen et al[165]	-	-	0.015-0.7	0.006-0.23	-
Bicerano et al[108]	-	3.93	1.69	0.592	0.43

By further observing the stress vs. strain in Figure 27, we find the axial modulus is high in the compressive state compared to the tensile state. This difference is attributed to the atoms moving close together under compressive stress while undergoing repulsion due van der Waals repulsive forces. Under this constraint, there is not enough room for the atoms to wiggle around and hence the polymer is stiffer and behaves stronger under compressive stress as opposed to tension. In addition, the polymer samples responds to the applied stress elastically in both the x and z direction up to a certain stress, where an onset of plastic behavior is observed. Furthermore, the graph clearly indicates a significant increase in strain after a reaching close to the plastic region, which is attributed to the sudden increase in stress value after reaching close to the plastic flow region, may shock the system resulting in a large increase in strain in the polymer samples.

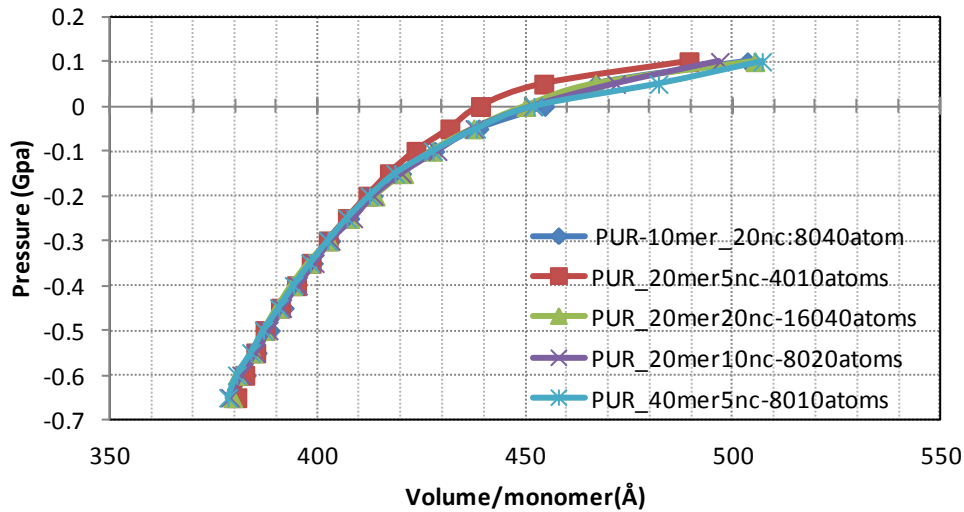


Figure 28: Average volume/monomer vs. pressure curve of polyurethane models.

To calculate the elastic properties using the MD approach, we estimated slope of straight line in the elastic region covering both the response from tensile and compressive stress in Figure 27. Using a linear fit in the linear region of the stress-strain curve, the values of bulk, young and elastic modulus as well as Poisson’s ratio for the different polymer samples are shown in Table 11. The calculated values are much lower than experimental values of Young Modulus of 1.69Gpa, reported by Bicerano et al. However, Martinessen et al.[165] reported different values of Young modulus between 0.015-0.7Gpa. One can argue the dynamic method yields lower limit of property predications. Furthermore, comparison with experimental values is not straightforward. In addition, experimental values refer to

thermoplastic polyurethanes with different chain extenders, which play an important role in polymer morphology.

Table 12: Bulk modulus K for various polyurethane models by hydrostatic pressure

Polyurethane	No. of atoms	K(Gpa)
PUR-1	8040	4.15
PUR-2	8020	3.82
PUR-3	8010	3.84
PUR-4	4010	4.81
PUR-5	16040	3.20
Average		3.96 ± 0.5

We subjected the sample to equal compression and tension pressures on all the faces in an NPT (isothermal-isobaric) ensemble to measure the volumetric response. The tensile and compressive loading conditions were incrementally applied one at a time, starting with room pressure conditions. The temperature was kept at 300 K. polyurethane reinforced with graphene sheet shows significantly larger bulk modulus of 66.36Gpa, than polyurethane-graphene flakes nanocomposite, 1.07Gpa. This significant difference in bulk modulus between graphene sheet and graphene flakes, suggest that to achieve better mechanical properties of nanocomposites, aggregated graphene flakes need to be exfoliated in form of graphene sheets and uniformly dispersed into a matrix system.

Table 13: Elastic constants, bulk modulus, young modulus and Poisson's ratio of pristine polymer, graphene and graphene flakes calculated from stiffness matrix

Model #	C11 (Gpa)	C22 (Gpa)	C33 (Gpa)	C12 (Gpa)	Young Modulus (Gpa)	Bulk Modulus (Gpa)	Poisson's ratio
PUR-I	5.430	4.97	5.22	3.194	3.245	3.938	0.370
Gr-PUR-I	126.52	120.17	63.08	52.24	95.98	76.8	0.292
Gr-flakes-PUR-I	5.001	3.913	3.66	2.09	3.76	3.06	0.294
Experimental PUR Values (169)					1.690	3.930	0.500

In addition to the uniaxial deformation of the polyurethane samples, we subjected to samples to a hydrostatic tension and compression using NPT ensemble in molecular dynamics. The temperature was kept at 300K. In our simulation results, we observed an increase in volume with application of tensile pressure and increase in the case of compressive pressure. The slope of the density variation with pressure near zero atmospheres gives a measure of bulk modulus (K) given by equation 5.11 is the equilibrium volume at room pressure. We used the linear region of the pressure volume data in Figure 24 to obtain the slope at small deformation. The bulk modulus for each polymer model was evaluated and summarized in Table 10. From the graphs, the average value of the bulk modulus under volumetric deformation for the six polyurethane models is given in 3.96Gpa. The simulated values are in close agreement with the experimental values provided by Bicerano et al of 3.93Gpa.

By following the same approach used to calculate the elastic constant of the amorphous polymer model in the early section, the elastic constants Elastic constants, bulk modulus, young modulus and Poisson's ratio of the polymer reinforced with graphene sheet (Gr-PUR-1) and polymer reinforced with graphene flakes (Gr-flakes-PUR-I) are evaluated from the stiffness matrix. The results are shown in Table 9, showing a significant increase in the Bulk and Young modulus as well as the elastic constants, compared to the sample with the graphene flakes. Another clear indication on the importance of surface effects of graphene sheet versus the graphene flakes on the effects on both the thermal-mechanical properties of polyurethane.

## 5.5. Concluding Remarks

Amorphous polyurethane models were successfully generated with the use of Dreiding force fields, with the exponential six forms of van der Waals interactions. The electrostatic interactions were evaluated using Ewald Summation Method where the atomic charges are determined from charge equilibration method. We calculated the properties relating to inter-molecular interactions, such as density, glass transition temperature and mechanical properties. To obtain the mechanical properties we utilized both the molecular mechanics and molecular dynamics using uniaxial deformation. The stiffness matrix results show the basic feature of an isotropic material. We have calculated the moduli and poisons

ratio for all polyurethane models; these properties are essential in characterizing the mechanical properties of a system. Calculation of equilibrium density and mechanical tests gives us confidence over the simulations, since they predict the properties with the same order of magnitude as experimental, this is important because later investigation of polymer nanocomposite will have significant credibility.

The elastic and thermodynamics properties on the effect of graphene sheets and graphene flakes on amorphous polyurethane were investigated with molecular dynamics simulation. Young's modulus of 95.98Gpa was estimated for polyurethane reinforced with graphene sheet compared to 3.76Gpa for polyurethane reinforced with graphene flakes. Elastic properties obtained for were significantly higher for the polyurethane/graphene sheet nanocomposite compared with the graphene flakes.

This work highlights the promise of atomically thin, periodic nanostructures like graphene for shock wave mitigation. Our approach strongly suggests that a bottom-up, systematic redesign of composite materials can yield significant improvements over existing technological methods. We expect that this work will add to the understanding of next generation nanocomposites for materials for extreme environment technology.



## 6. DYNAMIC RESPONSE OF AMORPHOUS POLYURETHANE AND ITS GRAPHENE NANOCOMPOSITE TO SHOCK-WAVE LOADING

### 6.1. Motivation

Currently, there is an increased interest in blast resistant properties of multi-phase polymeric elastomers such as polyureas [166] and polyurethanes [36, 37]. Of interest in this work is the use of graphene in polyurethane (PUR) matrix, to enhance the high impact and shock mitigation properties of PUR for potential use in military and defense applications [36, 37]. Application of PURs coating can help to minimize fragmentation that results in injury-causing blast-pressure propelled debris [3, 33]. Likewise, PUR coatings are applied to military armor to increase resistance to ballistic penetration because of their intrinsic large strain ability critical for energy absorption, even at low ambient temperature [3, 33, 38, 40, 41]. Moreover, their dynamic properties can be appropriately tailored under high strain rates of the order of  $10^5 \text{ s}^{-1}$  to  $10^6 \text{ s}^{-1}$  ubiquitous during shock-wave or high impact loading[36].

PUR can dissipate and divert shock pressure in a controlled manner[36]. The dissipative nature of polyurethane could arise from its complex nano-meter scale morphology of repeating units of hard and soft segments. The alternating soft and hard segments self-assemble into two phases. Such phase separation contributes to the excellent mechanical properties of PUR [33], hence its use in structural application. Furthermore, PUR is only lightweight, thus its dynamic properties can be appropriately tailored under high pressures of the order of thousands of atmospheres ubiquitous during shock or impact loading [36, 37, 159, 166, 167].

Interactions of shockwaves in polymers and their nanocomposite occur at all levels and scales, from nano-to micro and to continuum and thus can be designed at all levels. Additionally, owing to imbalance of forces on atoms arising from shock wave, highly non-equilibrium regions may exist, resulting to the formation of unexpected meta-stable states of matter. This will in turn determine the time dependent structure, instabilities, and time evolution of the shock wave [168-170]. Whereas numerical and experimental studies on polyurethane (PUR) foam under impact loading have been proposed [36, 37], there is still a substantial uncertainty in understanding the mechanisms responsible for the shock-mitigation properties of polyurethane. Despite the numerous studies investigating the effect of graphene

nanofiller on the various properties of polymers, there are no studies investigating the dynamic response of graphene nanocomposite on shock wave loading. Incorporation of low weight percentage graphene layer in the polymer matrix has the potential to attenuate the strength of the traveling shock waves because of the high surface-to volume ratio.

Shock wave cause an abrupt and discontinuous complex changes in a material that include elastic-plastic deformation, fracture, chemical transformation and phase transitions[170]. Although, early studies measured the dependence of internal structure on static pressure [4–6], and more recent experiments have shown that the shock loading response of polymers is different from that observed in metals[171]. Unlike metals, polymers exhibit characteristics of packing, chain folding, free volume, and interaction between adjacent chains from the nano to the micro and continuum level. These structural and complex changes in polymers during shock events limit the use of experiments in examining the shock wave phenomena occurring in polymeric material.

Additionally, the highly dynamic nature of shock waves makes instantaneous measurements for predicting high-velocity impact and other dynamic loading of materials and structure responses highly challenging[170, 172]. These limitations can be offset by the use of simulation techniques, such as molecular dynamics[173], coarse grain dynamics [174], and first-principle simulations[175]. These techniques have gained traction in offering insights into the shock-wave phenomena of materials at atomistic scales.

In this work we investigate the effect of shock wave loading of polyurethane and its graphene-based nanocomposite using MD simulations. The use of MD simulations to examine the shock-wave phenomena is rare. However, few studies have successfully examined the shock wave phenomena in polyurea and phenolic/CNT systems. For example Grujic et al. [166] performed MD simulation to simulate the shock wave propagation in polyurea. Result from this simulation show various phenomena accompanying the formation and propagation of a planar shock wave within polyurea. Arman et al demonstrated the elastic-plastic transition in phenolic resin and its carbon-nanotube composite is characterized by shear stress relaxations and atomic-level slip. Phenolic resin shows a strong strain hardening and the phenolic/carbon nanotube composite demonstrate anisotropy in wave propagations, yield and CNT deformation. Consequently, the detailed information obtained for MD simulations can easily be used to either design experiments that will transform the

materials to a desired state upon shock, or to design new materials with tailored shock properties. There is an increased interest in the importance having accurate models based on fundamental understanding of material behavior. Thus modeling qualitative and quantitative aspects of shock propagation in polymers and polymer composites is of great significant importance.

In this study we aim to examine the phenomena and processes accompanying the formation and propagations of shock waves in polyurethane elastomer and subsequently its graphene based nanocomposite using molecular dynamics simulation. The investigations are important to achieve a deeper understanding on the shock-wave phenomena in both polymeric and nano-structures systems. Understanding this phenomenon will give prospect to new application based on cross-disciplinary approaches, in aerospace, defense, and astrophysics application.

## 6.2. Basics of Shock-wave Physics

When an air-borne blast-wave impacts on a head-protective gear, it creates inward-propagating (compressive) shock waves within the headgear component(s). A shock wave is a non-linear wave propagating through a medium at a speed faster than sound. The basis of shock wave is formed when an external force is applied to a material/system, resulting in compressive failure and deformation under unequal stress of shear stress. Loading due to uniaxial nature of the shock process contributes to the compressive-wave propagations characteristics.

The passage causes abrupt and significant changes in the material state variables (e.g., pressure, mass density, internal energy density, etc.). An increase in the shock strength increases its propagating speed and the extent of the state variables. A distinguishing from the acoustic waves, changes in materials states are isentropic in nature, that the passage of a shock wave causes irreversible changes in the same variable. The disparity arises from the fact that, at the shock-wave front, the material is subjected to high strain rates and, hence, energy dissipation via the activation of various viscous and inelastic-deformation processes is enhanced. In the case of acoustic waves, on the other hand, the wave front is highly diffuse and, hence, the material experiences low deformation rates. Excellent coverage of the basics of shock-physics can be found in a number of monographs and books [13]. In shock

experiments, it is very imperative to distinguish between particle velocity and shock velocity. Shock velocity is the speed of disturbance that goes through the material under the shock loading. On the other hand, the particle velocity is the velocity of an element of the material, which the shock wave passes over, and is lower than the shock wave velocity. Shock velocity and particle velocity form the basis of equations of state in shock experiments.

### 6.2.1. Equation of State and Jump Conditions

The basis of shock wave propagation and interaction is formed by the jump conditions in combination with a Hugoniot curve for the material in question. The propagation of shock wave in a material causes an abrupt and discontinuous change in thermodynamic quantities (e.g. pressure, density, temperature, and particle velocity).

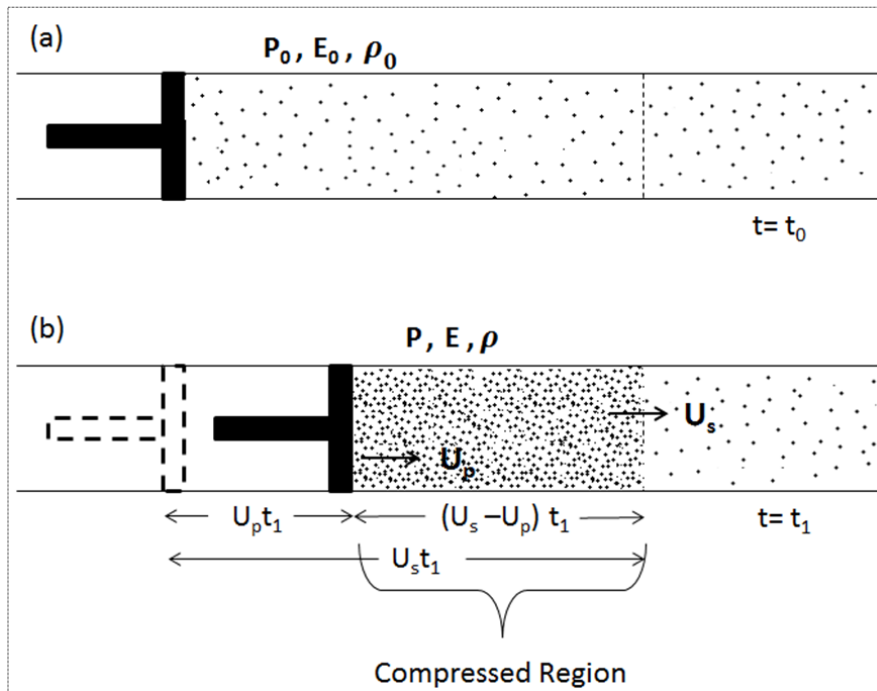


Figure 29: Schematic of rigid piston moving and driving shock into compressible fluid[172].

For an ideal shock, driven created when a piston is moved from an initial rest  $t = t_0$  into the compressible material at a rate of constant particle velocity  $U_p$ , after a time  $t = t_1$ , the compressed region in front of the piston moves forward by a distance  $U_s t_1$ . Where the

propagation of the disturbance ahead of the piston is the shock velocity  $U_s$  and the piston velocity is constant particle velocity  $U_p$ . Assuming the shocked material remains at initial conditions, the shock equation of state (EOS) is measured from the particle velocity  $u_p$ , and shock velocity  $u_s$  using the equation 6.0, 6.1 and 6.2 for the pressure applied to the shock (P), change of the energy respectively (E), and density ratio across the shock.

$$\rho_1 = \rho_0 \left( \frac{u_s - u_p}{u_s} \right) \quad (6.0)$$

$$P_1 - P_o = \rho_o (u_p - u_o)(u_s - u_o) \quad (6.1)$$

$$E_1 - E_o = \frac{(P_1 + P_o) \left( \frac{1}{\rho_o} - \frac{1}{\rho_1} \right)}{2} = \frac{1}{2} (u_p - u_o)^2 \quad (6.2)$$

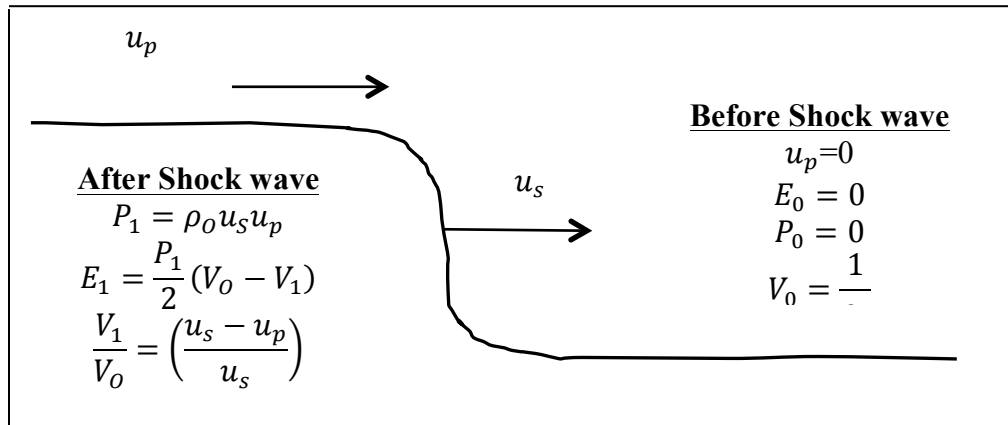


Figure 30: A schematic diagram of shock wave conditions with density  $\rho_o$ , particle velocity  $u_p$ , shock velocity  $u_s$  pressure (P), energy (E) and volume (V) before and shock wave and after shock wave.

These equations describe the discontinuous and abrupt nature of five thermodynamic variables; density ( $\rho$ ), particle velocity ( $u_p$ ), shock velocity ( $u_s$ ), pressure (P), and energy (E). These equations are commonly referred to as Rankine-Hugoniot equations. The equations describe the conservation of mass, momentum, and energy across a shock induced material transition, assuming that equilibrium exists on either side of the shock front zone. To

express the parameters as a function of one of the equations 6.0 to 6.2, we need to define the equation of state (EOS) the material equation 6.3.

$$u_s = c_0 + s_1 u_p \quad (6.3)$$

where  $c_0$  is the material bulk sound velocity and  $s_1$  is the empirical parameter giving the relationship between the shock and particle velocities. This equation defines the relationship between  $u_p$ , and  $u_s$  and can be obtained experimentally or theoretically. EOS data for a wide range of materials are found in literature, making it possible to obtain relationships between the five variable such as given in the Table 12, and example, pressure-particle velocity for some materials is given in Figure 31.

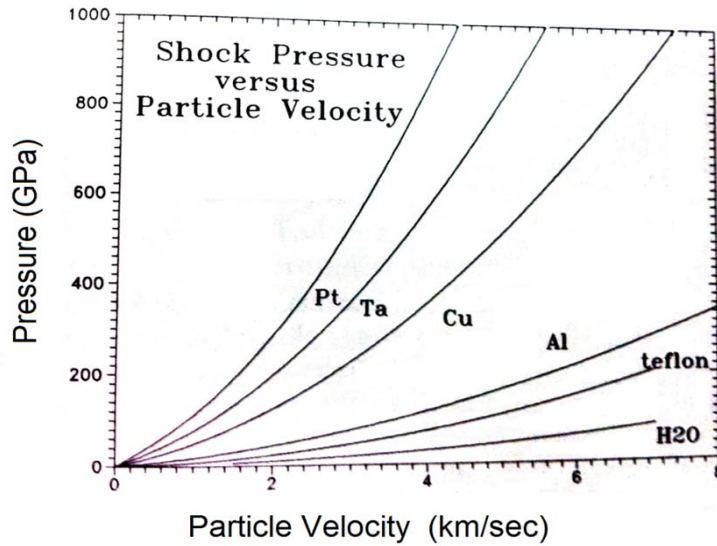


Figure 31: Shock pressure vs particle velocity for some standard materials [176].

Combing equations 6.0 and 6.1 and solving for  $U_s$  and  $U_p$  the following equations for the jump conditions are obtained.

$$U_s = V_0 \sqrt{(P - P_0) / (V - V_0)}, \quad (6.4)$$

$$U_p = \sqrt{(P - P_0)(V_0 - V)} \quad (6.5)$$

Table 14: Relationship between variables obtained during shock simulations

Variable relationship	Description
$P = \rho$	Pressure vs. density
P-V	Pressure-volume relationship
P- $U_s$	Pressure-shock velocity relationship
P- $U_p$	Pressure-particle velocity relationship

Both equations 6.4 and 6.5 can be plotted as shown in figure 4. With the initial states for pressure and volume denoted as  $P_0$ ,  $V_0$  and  $P$  and  $V$  respectively. It is important to note that the Hugoniot curve is not the path of states during the shock loading.

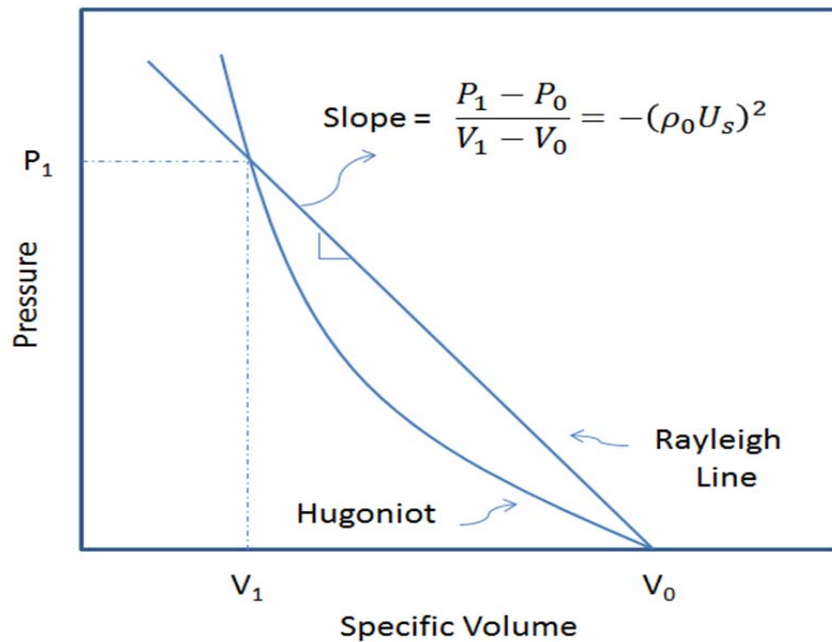


Figure 32: P-V Hugoniot curve and the Rayleigh line relationship ([172]).

It only represents the locus states of final shock states, which are  $P_0$  and  $P$ . On the other hand, the Rayleigh line, which connects the initial and final shock states linearly, represents the path for thermodynamic state of Hugoniot  $P_1$  and  $V_1$  (Figure 33) since this line can directly express the combination of the jump conditions (equation 6.4 and 6.5).

### 6.2.2. Experimental Techniques

One of the main objectives of shock compression experiments is it to obtain information on the high-pressure state attained by shock compression. The simplest way is to measure the two shock wave parameters in equations 6.0 and 6.2. In most cases, the shock and particle velocity are measured simultaneously. Additionally, the time profiles of the physical variable are also measured, giving information on the dynamic processes that occur inside a shock rise. Such information includes, elastic-plastic transition, structural phase transition at high pressure, relaxation structure due to stress relaxation etc. The duration of the shock compression dynamic process is about a microsecond or less, and accurate measurements requires a high time resolution of nanoseconds or higher.

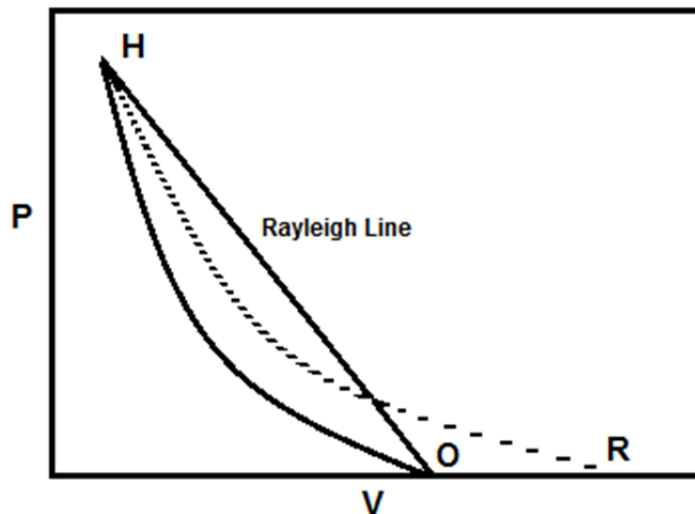


Figure 33: Hugoniot (OH curve), HR is the isentropic release paths and OH straight line is the Rayleigh line[172].

Historically, shock compression experiments were first used for military applications such as high impact tests and armor. After the World War II, there was a surge in research area of nuclear weapons, probing various techniques to obtain Hugoniot data for various materials [172]. Consequently, there was a need to generate accurate results of pressure, volume or energy values at locus points after the shock compression. Thus, to obtain reliable results, the shock front generated at the test specimen should be planar and the pressure should be uniform [172, 176]. Additionally, besides post damage analyses, to obtain shock wave and particle velocity values, there was a dire need to develop new instruments. Thus



the development of plane wave experiments and diagnostic tools to analyze the Hugoniot data, pioneered shock compression science in materials[170]. Beyond Hugoniot data, other material properties the study of phase transitions, chemical activity and melt boundaries during shock compression became possible [170, 172, 176].

As a planar wave propagates through a material under high pressure in the shock direction, the strain values are equal to zero in two lateral positions. However, at a finite dimension, edge effects exist, propagating at a speed of sound, resulting to uniaxial strain nature of the material under shock compression[37, 177]. In order to cancel out the lateral edge effect, initial measurements are imperative at the beginning of the shock experiments. Generally, there are three types of experiments used to create planar shock. These experiments use one of the followings: *i*) explosives or *ii*) guns or *iii*) energy deposition.

In explosive-driven shock experiments, the initiation of high explosives is performed by initiating devices or initiators, where initiation is defined as brining an explosive into the state of detonation[177]. Thus in shock compressions a planar detonation front is generated by the explosion creating a planar shock front in the specimen. This method is also called explosive plane-wave generator. Early designed plane-wave generators, depending on the impedance of material can create shock pressures at several tens of GPa[176]. A limitation of the early explosive plane-wave generators is the poor duration of the peak shock pressure values. However, using a flyer plate and giving acceleration via the plane-wave generator greatly increases the initial peak pressures (~ a few hundreds of GPa)[170, 172].

In the use of guns in shock experiments, a flat projectile is accelerated in order to make impact onto a flat surface, generating planar shock waves. Compared to the explosive shock experiments, guns provide a more controlled environment for the shock pressure magnitude and unloading conditions ([172])The most advance approach is he use of two-stage gas guns where high impact velocities in the range of 7 – 8 km/s and peak shock pressures on the order of 1Tpa is achieved [170, 177]. Additionally, the use of electromagnetic guns, such as rail guns is another approach for shock wave experiments to produce electromagnetic forces. Theoretically, Rail guns have very high projectile velocities even though there are still some improvements needed to reach velocities above 6 km/s [172]

Lastly the use of energy deposition is another method used to create planar shock. By superheating a specific area of a material in such a way it exhibits the behavior of a detonated

explosive initiates a high-pressure shock in the rest of the material. This is achieved by exerting an extreme amount of energy over a specific area instantaneous heat above vaporization temperature. Laser-driven shock generation has been widely used for high energy deposition [33]. Lasers are either directed onto the specimen resulting in ablation of the target into a high pressure plasma or used in a confined region such as glass enabling higher and longer pressure peaks [170, 172, 176]. Fast expansion of plasma creates high-pressure compressive shock waves inside the specimen. Plasma pressures having a range of a few GPa to hundreds of TPa were reported [170, 172, 176].

### 6.3. Computational Details

#### 6.3.1. Generation of Polyurethane Model for Shock Simulation

The goal of atomistic shock-simulations is to achieve some measure of continuum behavior. As such, bigger samples in terms of size and long simulation times are better. The shock simulation model was generated after verifying the thermal-mechanical properties of the amorphous polymer, to ensure a robust enough structure for shock simulations. As an initial step, we have constructed a unit configuration of amorphous polyurethane using Accelrys Material Studio [178] by randomly placing 30 repeat units of 4 polymeric chains into a 4.5 x 4.5 x 4.5 nm unit cell.

We have constructed a unit configuration of amorphous polyurethane by randomly placing 20 repeat units of 10 polyurethane chains into a 4.5 x 4.5 x 4.5 nm unit cell. This unit configuration of 8040 atoms is equilibrated with the constant-pressure-temperature NPT ensemble. Temperature and pressure were controlled using the Nose-Hoover thermostat with a 100 fs coupling constant and the Nose-Hoover barostat with 1000 fs coupling constant, respectively. For the NPT simulations, the three diagonal components were coupled together when the pressure was computed, and the dimensions dilated and contracted in concert a time step of 1 fs was used for all simulations to obtain a robust structure. The final equilibrium density calculated from simulation is 0.97 g/cm<sup>3</sup>. The density observed may differ from experimental data (1.00-1.12 g/cc) [164] because simulations deal with material free from mechanical defects and impurities.

As a first step to prepare shock structures for polyurethane we replicate the unit cell by

$2 \times 2 \times 2$  by equilibrium molecular dynamics using microcanonical (NVE) ensemble with Berendsen thermostat[179] at 600K. The system is further replicated in  $1 \times 1 \times 2$  followed at 700K. The second step is repeated at 900K and 1000K. The corresponding final structure is replicated by  $2 \times 2 \times 16$  with the resulting configuration with 514560 atoms and edge length of  $1.0 \times 1.0 \times 2.0 \text{ nm}^3$  is equilibrated with the constant-pressure temperature (NVT) ensembles at a time step of 1fs with periodic boundary conditions. The resulting polyurethane super cell configuration of is adopted for the shock simulations.

Table 15: Steps to generate shock simulation structure

Step	Replicate unit cell	No. of atoms polyurethane	Replication Temp(K)
1	$2 \times 2 \times 2$	64320	600
2	$1 \times 1 \times 2$	128640	700
3	$1 \times 1 \times 2$	257280	800
4	$1 \times 1 \times 2$	514560	900

### 6.3.2. Graphene-polyurethane Nanocomposite Consists of Graphene

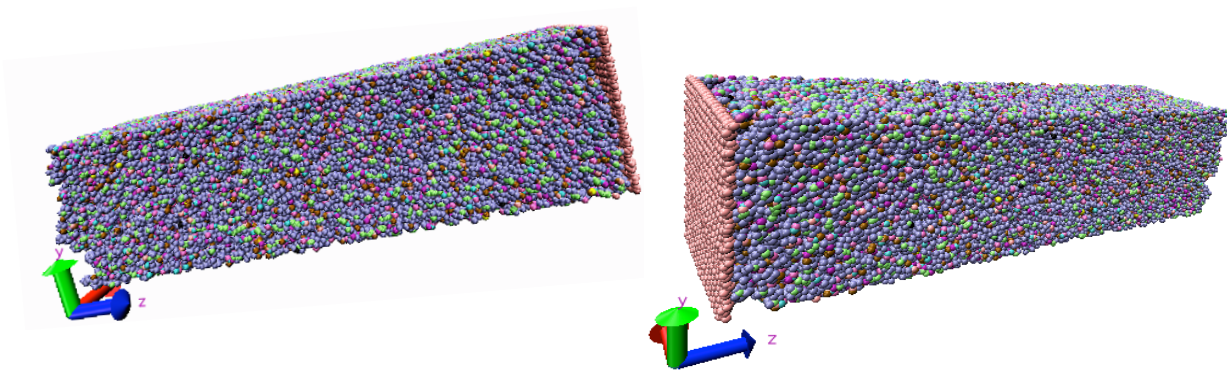


Figure 34: Graphene-polyurethane composite molecular level computational cell with graphene positions in (a) Zhi and (b) at the origin Zlow, density  $0.845 \text{ g/cm}^3$ .

We generated a graphene sheet unit configuration of 3024 atoms with dimension  $a = 88.56 \text{ \AA}$  and  $b = 89.46 \text{ \AA}$ , equal to the x and y dimension of the pristine amorphous

polyurethane using Material Studio software. Two samples, one with the graphene sheet at the origin, Zlow and the other at the edge of the graphene sheet, Zhi as seen in Figure xx, a and b respectively. The van der Waals distance between the polyurethane and graphene sheet is 0.34 nm, similar to an earlier work in this study for graphene-polyurethane composite modeled in the previous section. This van der Waals distance thus induces the excluded volume between the graphene sheet and the polymer matrix.

The composite unit is first equilibrated at constant-volume-temperature (*NVT*) ensemble for 50ps, followed by thermal annealing procedure at constant volume, where the system is heated to 600K, equilibrated at 600 K for 20ps and then cooled to 300 K. The resulting configurations are then equilibrated for 100ps with the isobaric-isothermal *NPT* ensemble at ambient conditions in the x and y dimensions for shock simulations ( $\rho = 0.845\text{g/cm}^3$ ) which is comparable to the density of the pristine polymer of  $\rho = 0.850\text{ g/cm}^3$  from MD simulations.

### 6.3.3. Shock Simulations

We performed the shock experiments by adopting projectile wall geometry and microcanonical (*NVE*) ensemble to mimic adiabatic conditions. In this approach, the shock is initiated by imposing a desired initial particle velocity  $u_p$  pointing in the positive z direction, with  $u_p$  ranging from 0.1km/s to 2.0km/s with increments of 0.5km/s. The particle position and initial Maxwell-Boltzmann velocities corresponding to a temperature of 300K are augmented by the particle velocity is added to the thermal velocity of polymer. The simulation direction is fixed in x and y directions such that 1D strain loading mimicking the experiments are generated. As soon as the polymer collides with the stationary wall a shock waves begins to move to the right or in the direction opposite to  $u_p$  at a velocity of  $u_s - u_p$ . The energetic interaction between the wall particles and the polymer are treated using a 12-6 Lennard-Jones potential. Setting the piston velocity, which was held constant throughout the simulations, controlled the shock strength. These velocities produced pressures ranging from tens to hundreds of GPa. All observables were calculated by averaging per-atom quantities over 5 Å wide bands perpendicular to the propagation direction.

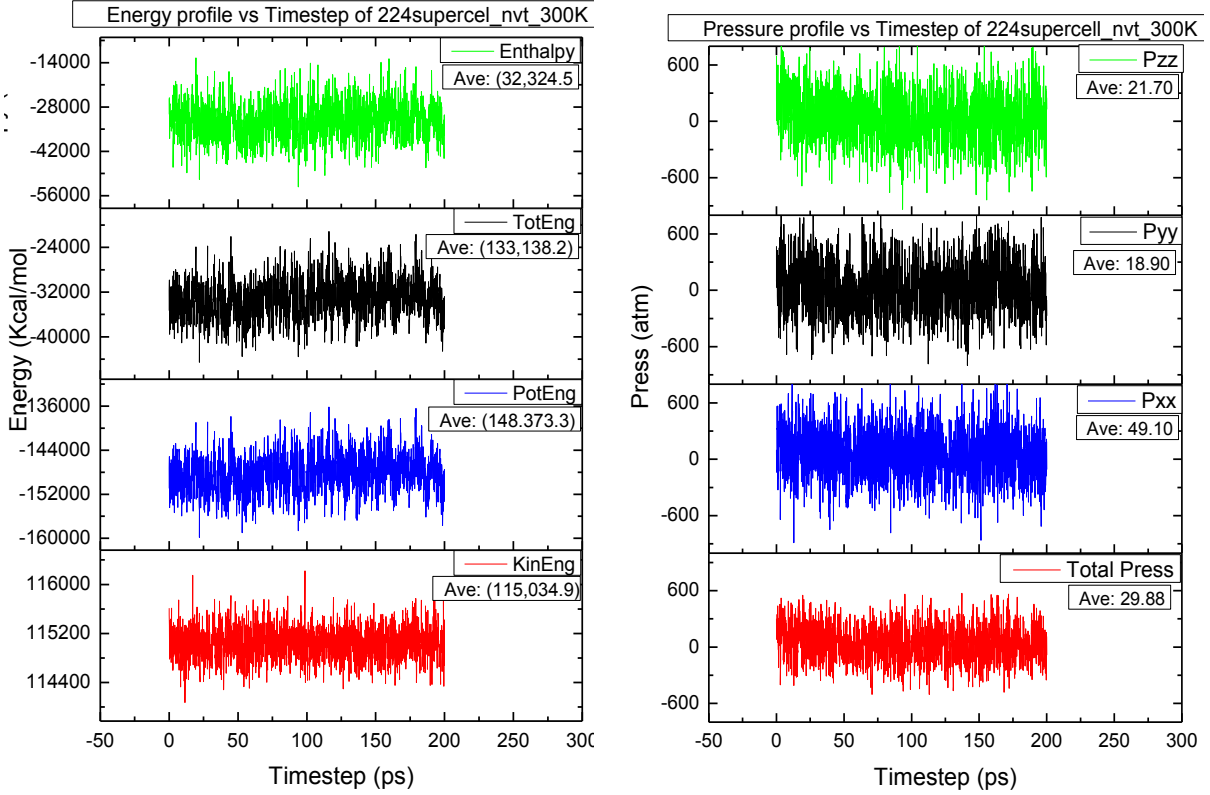


Figure 35: Energy and pressure profiles for polyurethane 2x2x4 (128640 atoms) super cell structure at 1 atom and 300 K using NVT-MD.

Our molecular dynamics (MD) simulations were performed using the open-source classical MD code large-scale atomic/molecular massively parallel simulator (LAMMPS) package[31]. All molecular models were generated using amorphous polymer builder in the commercial package, Material Studio [32]. We used Dreiding force field[124] to describe the interaction in the polyurethane and its graphene nanocomposite. Bond and angle interaction are harmonic while van der Waals interactions are evaluated using the Lennard-Jones potential truncated at a cut-off distance of 12.5Å. The local structure is characterized with profiles of stress ( $\sigma_{ij}$ ), velocity ( $u$ ) and temperature ( $T$ ) at a given time  $t$ , via one-dimensional binning along shock direction. Similar simulation and analysis details were presented elsewhere [166, 180].

## 6.4. Results and Discussion

### 6.4.1. Shock Response in Polyurethane

NVT molecular dynamics were conducted to determine the pressure and energy profiles at 1atm and 300K of the 2x2x4 (128640 atoms) and 2x2x8 (514560atoms) polyurethane super cell structures. The final density for the polyurethane super cell configuration is  $\rho = 0.845g/cm^3$ . This value is 14% lower than the initial density of  $\rho = 0.970g/cm^3$ , which is the calculated polyurethane unit cell. This difference is attributed to shifting the chains across boundaries while changing the system from periodic to non-periodic and compacting the system so as no to have chains from one unit cell being lost in the non-periodic system.

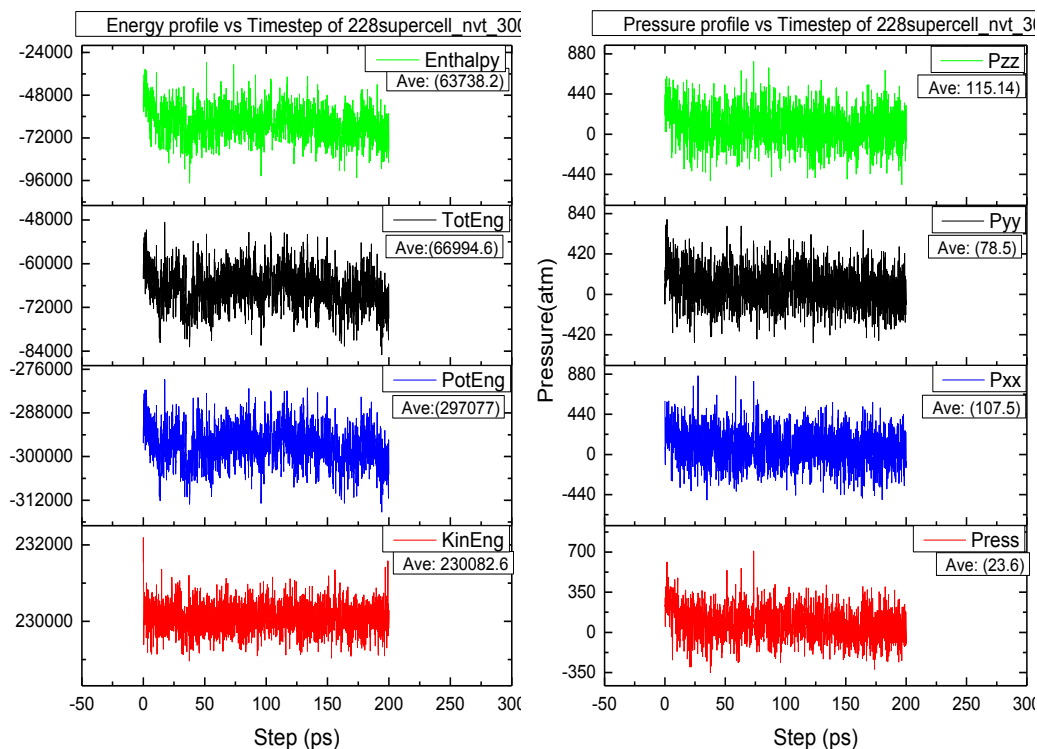


Figure 36: Energy and pressure profiles for polyurethane 2x2x4 (128640 atoms) super cell structure at 1 atm and 300 K using NVT-MD.

Figure 35 and 36 show the energy and stress tensor profiles for both samples respectively. The results of both profiles remain constants with no indication of significant drift during the 50ps simulations. This is important when running shock simulations in that, a

robust structure is essential to obtain sound results, not only in shock simulations, but also in performing any type of simulation experiments.

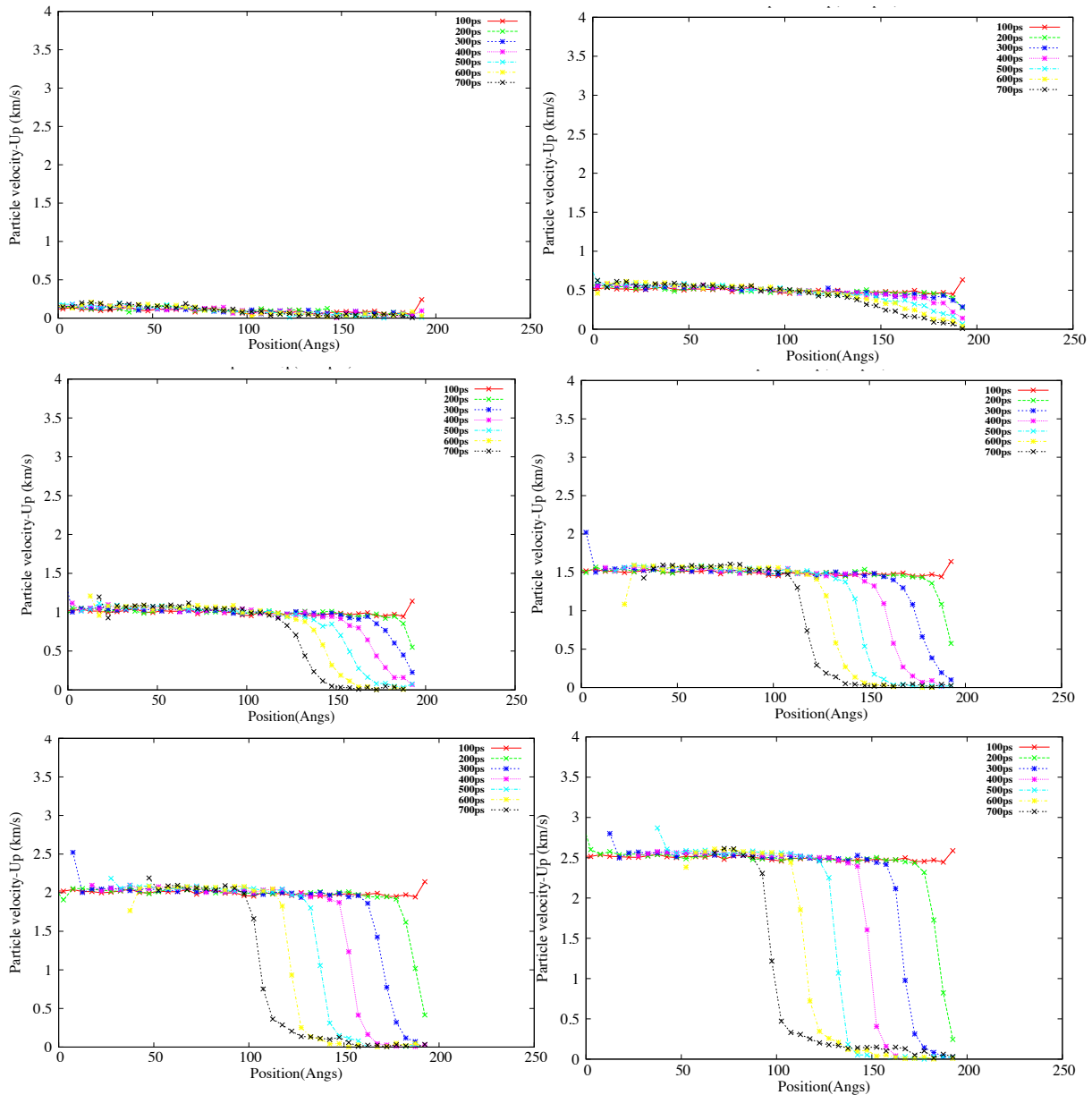


Figure 37: Spatial shock wave profiles as a function of propagation distance, with piston velocity of (a) 0.1km/s, (b) 0.5m/s, (c) 1.0km/s (d) 1.5km/s, (e) 2.0km/s and (f) 2.5km/s respectively in amorphous polyurethane from MD simulations.

From the sample, we performed shock simulations under velocities ranging from 0.1 km/s to 2.5 km/s, using the 2x2x4 (128640 atoms) polyurethane sample. Ideally, one would use a sample with a higher number of atoms, but with atomistic simulation, comes challenges

of computational time and cost. However, the prediction of material properties using simplistic models is quite sufficient for understanding material response under shock simulations for practical applications. For the shock simulations, we observed for spatial shock wave profiles by plotting the particle velocities against the bin center in the z direction, i.e. the direction of shock propagation.

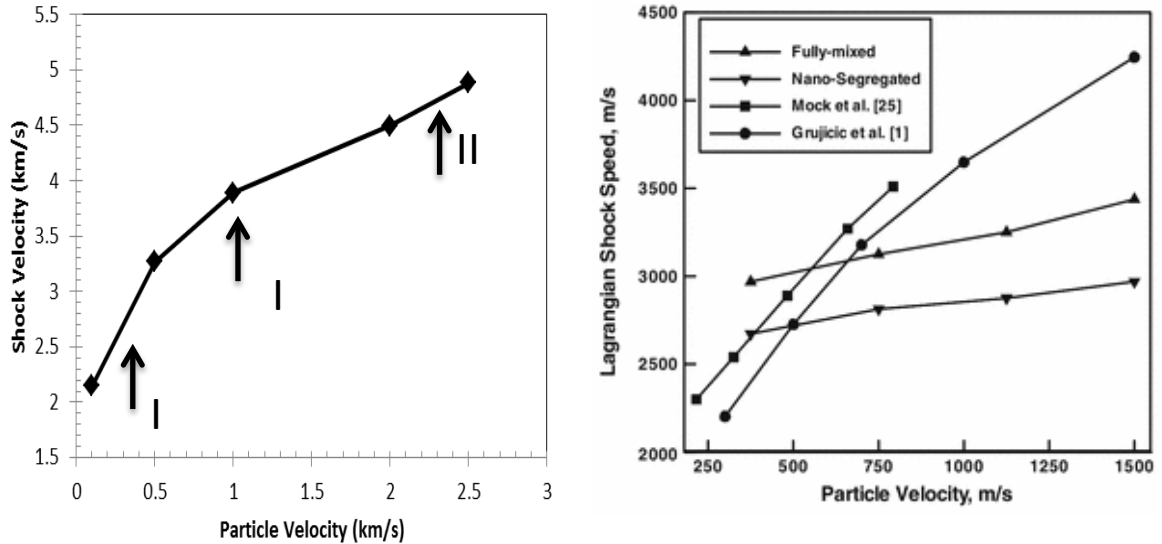


Figure 38: Molecular-level computational analysis of (a) Hugoniot of relations particle-velocity dependence of the shock velocity for pristine amorphous polyurethane from direct MD shock simulations, and (b) For comparison, similar polymer (polyuria) experimental results obtained in the study of Mock et al. [25] and the ones predicted by the continuum-level polyurea material model of curve labeled Grujicic et al. [1] are also displayed.

The results are displayed in Figure 37, were obtained under identical conditions, except for the magnitude of the imposed particle velocities in the case of Figure 37a 0.5km/s to Figure 37d of 2.5km/s. The simulation times expressed in picoseconds are used to label the corresponding curves in the plots. Examination of the results, reveal that at a particle velocity of 0.1km/s that there is hardly any observable or change in structure in the material response. However, as you increase as the particle velocity one can observe that after a brief transient period, the shock appear to reach steady state wave profile, which is as a result of continuous momentum to the system. Furthermore, the plots also reveal that as the shock strength increases (from imposed particle velocity), the shock speed increases, while the shock wave



thickness decreases. This behavior is identical to one predicted by continuum-level theory of shock solids[181].

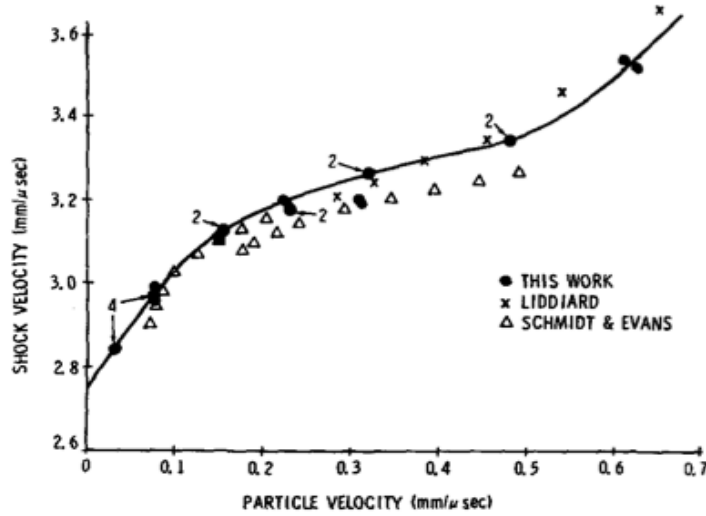


Figure 39: Shock velocity vs particle velocity of PMM, (adapted from ref [182]), to highlight the curvature that characterizes the three different regimes found in polymers under shock compression.

The different shock propagation regimes are understood using the shock Hugoniot EOS. EOS gives the dependency of shock velocity on piston velocity. To estimate the EOS for the amorphous polyurethane, we utilized the Equations 6.0 and 6.1 described in sections 6.2 to obtain shock speed ( $u_s$ ). The results of shock dependency on particle velocity are shown in Figure 38. For comparison, experimental results obtained in the work of Mock et al. [25] (the curve labeled “Mock et al. [25]”) and the ones predicted by the continuum-level polyurea material model of Grujicic et al. [166](the curve labeled ‘Grujicic et al. [1]’) are also displayed in this figure 39(b). The Hugoniot of many polymers, metals and ceramics can be fitted assuming a linear shock velocity-particle velocity relationship. There are two points to note here. First, a linear regression applied to data points and utilizing equation 6.3 for polyurethane gives an EOS,  $U_s = 2.494 + 1.0192U_p km/s$ , where,  $c_o$  and  $S$  values of 2.494km/s and 1.019 respectively. Additionally, other researcher [171] have shown from theoretically studies, that the Hugoniot for many polymers over a large particle velocity range is parabolic, which is the case for our polyurethane simulations results. Secondly, the fitted line provides a bulk sound speed of 2.49km/s, which is slightly lower than the polyurethane value of 2.54km/s for  $U_p$  ranging from 0.6-2.6km/s as, reported in Cater and

Marsh[171]. Furthermore, this behavior is consistent with most polymer behavior surveyed by Carter and Marsh, and can be explained as due to a rapidly varying rate of change in compressibility in low-particle velocity region.

Experimental studies [171] on the Hugoniot EOS of a large number of polymers are characterized by three distinct regimes. The two arrows schematically divide these regimes as shown in Figure 38. Regime I is characterized by a distinct curvature. Regime II shows a linear  $u_s-u_p$  correlation. Consequently, the extrapolation this regime to zero  $u_p$  results to a  $u_s$  number that is above ambient bulk sound speed. The meticulous experimental studies on polymethyl methacrylate (PMMA)[182] have shown this general behavior as shown in Figure 39.

Regime I curvature is explained with interatomic potentials. Regime III is also linear. Furthermore, a substantial volume reduction is evident in the transition from regime II to III. Barker et al, expounded on “phase transition” to be neither polymorphic transformation nor crystallographic sense nor melting/vaporization[171, 182]. In addition, the breaking of covalent bonds within chains and subsequent reformation of tetravalent bonds between chains lead to large volume changes[182]. The limited nature of our simulations to fully capture the II–III transition is in line with its chemical behavior, since the bond breaking and formation is not inherent in the Dreiding force field[124]. Hence, reactive force field such as, ReaxFF[152] are essential to predict bond-breaking and bond formation, thus provide a clear presence of phase transition in the dynamic behavior of materials.

Figure 41 (b), we show the average final shock temperature behind the shock front for several shock pressures. The shock temperature near transition is about 450K at  $u_p = 1.5\text{kms}^{-1}$  and Hugoniot pressure  $P_H$  at 33.24Gpa. Simulation profiles results appear to be accurate, however the estimated temperature much lower than the value estimated by Carter and Marsh[171] of high-pressure of (20–30GPa), experience high-temperature(2000K) phase transformation as a the second feature common to the polymers with the possible exception of two of the fluoro plastics.

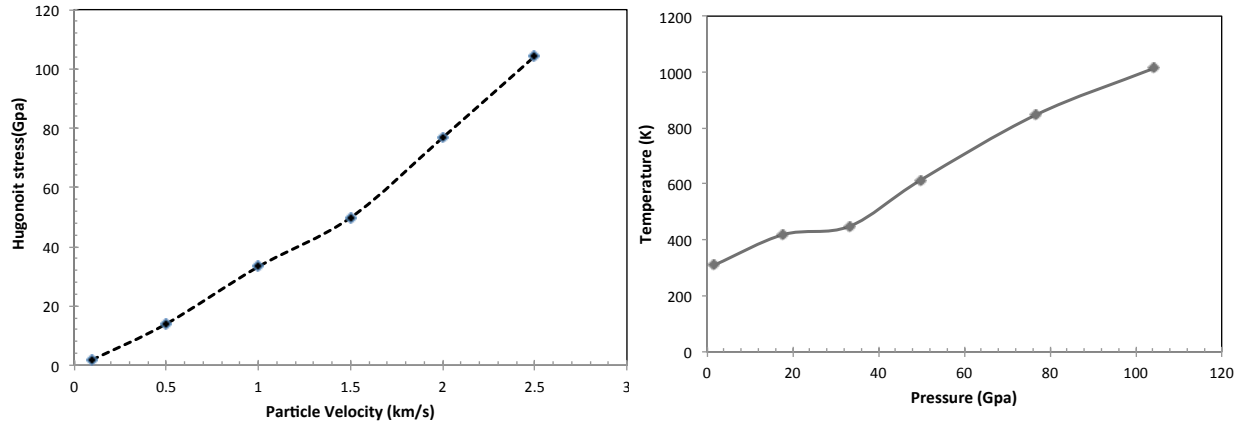


Figure 40: Graphs of (a) Hugoniot stress vs. particle velocity (b) Hugoniot stress versus strain of amorphous polyurethane using MD simulations.

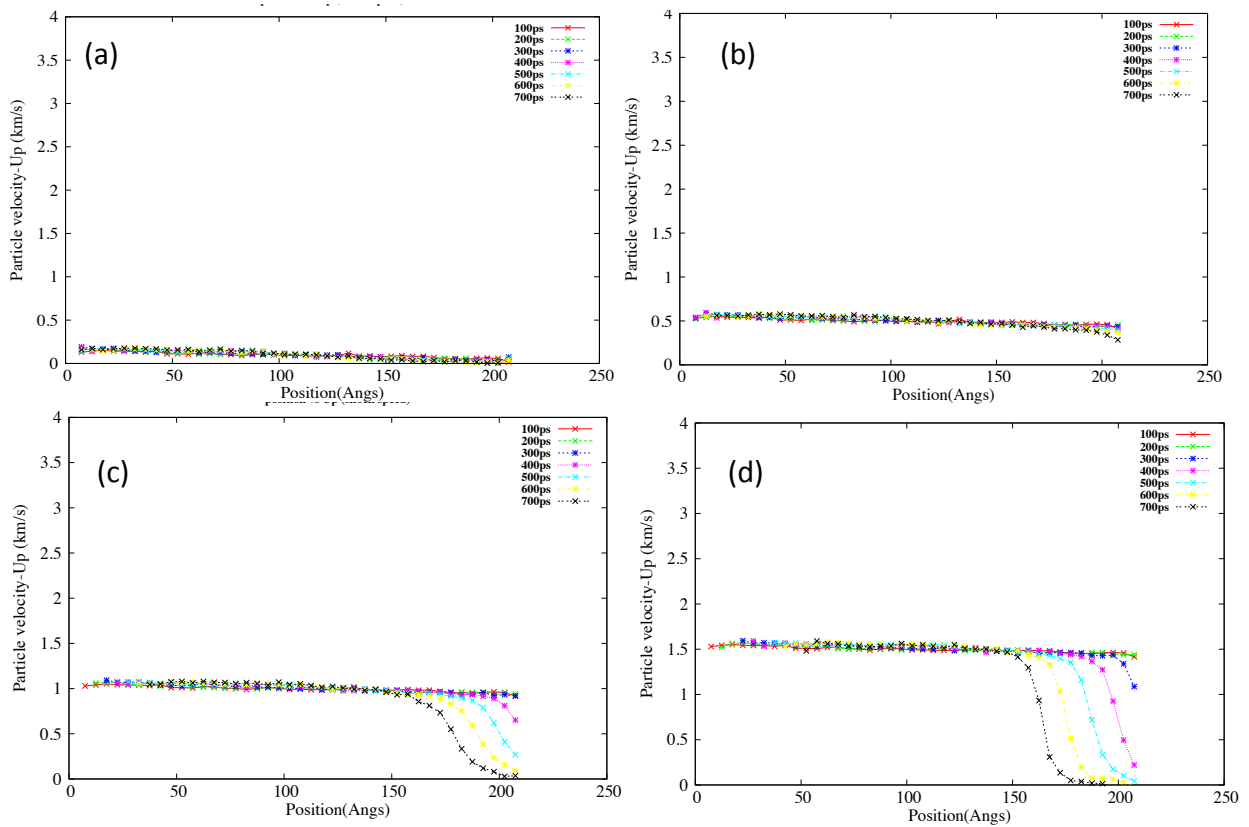


Figure 41: Spatial shock wave profiles as a function of propagation distance, with piston velocity of (a) 0.1 km/s, (b) 0.5 m/s, (c) 1.0 km/s, and (d) 1.5 km/s respectively in Graphene-polyurethane (Gr-pur) from MD simulations.

By utilizing the Rankine-Hugoniot relationship and the EOS, the relationship between Hugoniot Stress and particle velocity can be determined as long as the sound velocity,  $c_0$

,and empirical constant  $S$  in the EOS are known. Figure 41(a), shows the Hugoniot stress vs particle velocity of amorphous polyurethane from out MD simulations shock studies. As observed from the data obtained, the curve obtained has a regular concave –up profile.

#### 6.4.2. Shock Response in Nanocomposite

For the graphene-polyurethane (Gr-pur) nanocomposite, we applied shock loading at the same particle velocity as  $u_p$  in 0.1km/s to 1.5km/s. Figure42 (a)-(d) compares four wave profiles where the shocks are initiated at the same position  $z_{low}$  and recorded at the same time (100ps-700 ps). Where position, specifies the shock direction. The wave profiles similar to pristine polyurethane demonstrates the existence of well-supported shocks. In addition, wave profiles illustrate difference in the shock velocity developed within the nanocomposite. Furthermore, the plots show an increase in slope with increasingly particle velocity.

In Figure 42 (a), we have plotted the comparison of the two systems, nanocomposite and the polyurethane at  $U_p=1.5\text{km/s}$ . The three shocks wave profiles are initiated at the same position and recorded at the same time (800ps). The shock from for the nanocomposite with graphene at the Zhi position (Gr-pur l zhi) leads slightly that of graphene at Zlo position (Gr-pur l zlow). Also the shock wave front of the pure polyurethane (pur) lags significantly behind the nanocomposite samples. The higher wave speed in nanocomposite and the geometry of graphene directly leads to the differences in the shock fronts. Additionally, we obtained the stress components in the shock directions, Figure 43 (b), as a function of shock wave propagation in the composite is slightly lower than the pure polyurethane. Also, Gr-pur Zhi is slightly higher than Gr-pur Zlow. After an initial rise in pressure in the pur and Gr-pur at Z low, the Hugoniot elastic limit (HEL) is reached at pressure  $\sim 10\text{Gpa}$ , consequently, the Gr-pur zhi, does not similar characteristics, with the shock pressure staying continuously at 7Gpa. Beyond the HEL, the pressure rises continuously to the reach the Hugoniot state.

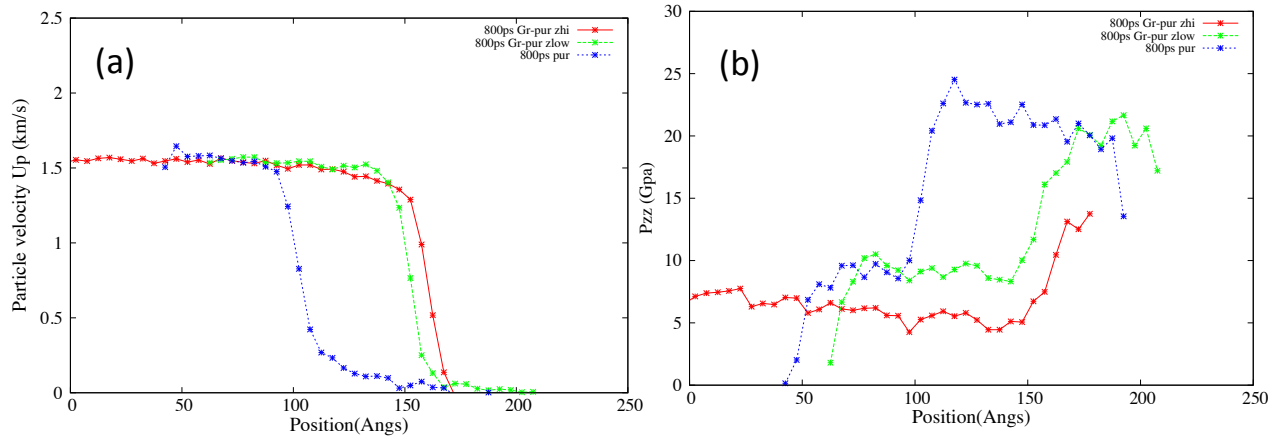


Figure 42: Shock profiles of (a) shock speed ( $U_p$ ), stress ( $P_{zz}$ ) and with piston velocity of 1.5km/s after 800ps respectively of graphene-polyurethane nanocomposite at Zhi (Gr-pur Zhi), at Zlow (Gr-pur Zlow), and amorphous polyurethane (pur) from NEMD simulations.

Thus graphene in general has a significant effect on the shock wave profiles of polyurethane. Consequently as a result, graphene increase the compressional stiffness of polyurethane. The volume ratio of graphene in the nanocomposites is about 9%, increasing the number of layers and volume ratios should have a positive effect both on the shock front characteristics and shock states.

## 6.5. Concluding Remarks

In this work, we have used non-equilibrium molecular dynamics (NEMD) simulations to study the shock propagation and material response of polyurethane and its graphene based nanocomposite. Calculation of the Hugonit states of polyurethane agrees with the experimental studies. However the phase change phenomena observed in experimental work was not visible in the present work. This is likely due to the bond breaking and formation, which is a clear characterization of the phase changes. The graphene-polyurethane nanocomposites demonstrate similar shock wave propagation slowing down the shock wave propagation. This is likely due to graphene inducing stress concentrations in the composite and may increase the yield strength. Moreover, our simulations suggest that the bulk shock response of the composites depends on the position of the graphene, with a slight difference being observed between the shock response in the Zlow position (initial direct contact with the projectile) or Zhi, (initial direct contact with the polymer).

## 7. SUMMARY

In this work, we have applied computational techniques to simulate processes at the atomistic level in investigating the structure-properties relationship, and dynamic response of hybrid material (polymer-nanocomposite). We have calculated the mechanical properties of 2-D graphene structure using two different approaches; the *ab-initio* calculation using density functional theory and atomistic simulation using molecular mechanics approach. Firstly, we employed the *ab-initio* approach within density functional theory (DFT) to perform total energy calculations on elastic constants on graphene. In order to obtain accurate and comparable results to previously published work we initially determined the total energy convergence of graphene with respect to the energy cutoff and k-point sampling of the Brillouin zone. The energy cut-off was found to be comparable with other studies. Once convergence was successfully achieved, we then proceeded to calculate the elastic properties of monolayer graphene. We compared our results with previous theoretical and experimental results available. Interestingly our calculated results is very close to the theoretical and experimental data, leading us to conclude that our structure is plausible.

In addition to *ab-initio* calculation, we calculated elastic constant of monolayer graphene using MM simulations. The general anisotropic, non-linear mechanical behavior of graphene is evident on both approaches. However, the accuracy of the mechanical properties predicted by this approach are limited by empirical potentials. Both the Tersoff and New\_Tersoff potential used in this study do predict a reasonable value of elastic modulus of graphene.

Furthermore, we have successfully developed amorphous polyurethane models were using of Dreiding force fields, with the exponential six forms of van der Waals interactions. The electrostatic interactions were evaluated using Ewald Summation Method where the atomic charges are determined from charge equilibration method. We calculated the properties relating to inter-molecular interactions, such as density, glass transition temperature and mechanical properties. To obtain the mechanical properties we utilized both the molecular mechanics and molecular dynamics using uniaxial deformation. The stiffness matrix results show the basic feature of an isotropic material. We have calculated the moduli and Poisson's ratio for all polyurethane models; these properties are essential in characterizing

the mechanical properties of a system. Calculation of equilibrium density and mechanical tests gives us confidence over the simulations, since they predict the properties with the same order of magnitude as experimental, this is important because later investigation of polymer nanocomposite will have significant credibility. The elastic and thermodynamics properties on the effect of graphene sheets and graphene flakes on amorphous polyurethane were investigated with molecular dynamics simulation. Young's modulus of 95.98 Gpa was estimated for polyurethane reinforced with graphene sheet compared to 3.76 Gpa for polyurethane reinforced with graphene flakes. Elastic properties obtained for were significantly higher for the polyurethane/graphene sheet nanocomposite compared with the graphene flakes.

Furthermore, we have used non-equilibrium molecular dynamics (NEMD) simulations to investigate the dynamic response behavior of polyurethane and its graphene nanocomposite. Calculation of the Hugonit states of polyurethane agrees with the experimental studies. However the phase change phenomena observed in experimental work was not visible in the present work. This is likely due to the bond breaking and formation, which is a clear characterization of the phase changes. The graphene-polyurethane nanocomposites demonstrate similar shock wave propagation illustrating characteristics of impeding the shock wave when subjected to difference particle velocities. This is likely due to graphene inducing stress concentrations in the composite and may increase the yield strength. Moreover, our simulations suggest that the bulk shock response of the composites depends on the position of the graphene, with a slight difference being observed between the shock response in the Zlow position (initial direct contact with the projectile) or Zhi, (initial direct contact with the polymer).

Conventionally, molecular simulations, in general computational experiments, will never replace conventional laboratory experiments. Nevertheless, with the ever-increasing computational power, the use of computational experiments is gaining much attention in research in more areas of physics, chemistry, biology and material science. Furthermore information obtained in simulations are only reliable when compared with experimental studies. Hence providing a supplemental understanding to experiments, and guide the future of experiments in solving problems in engineering. The major advantage of molecular

simulations is that it provides fundamental information at the very basic electronic and atomistic level.



## REFERENCES

1. Naik, N.K. and A.V. Doshi, *Ballistic impact behaviour of thick composites: Parametric studies*. Composite Structures, 2008. **82**(3): p. 447-464.
2. Cheeseman, B.A. and T.A. Bogetti, *Ballistic impact into fabric and compliant composite laminates*. Composite Structures, 2003. **61**(1-2): p. 161-173.
3. Bahei-El-Din, Y.A., G.J. Dvorak, and O.J. Fredricksen, *A blast-tolerant sandwich plate design with a polyurea interlayer*. International Journal of Solids and Structures, 2006. **43**(25-26): p. 7644-7658.
4. Kandola, K.B., *Nanocomposites in Fire Retardant Materials*. 2001, New Jersey: John Wiley & Sons Inc.
5. Sharpe, J., William N, *Springer Handbook of Experimental Solid Mechanics*. 2008, New York: Springer Science+Business Media.
6. Allen, M.P. and D.J. Tildesley, *Computer Simulation of Liquids*. 1987, New York: Oxford University Press.
7. Vivekchand, S.R.C., U. Ramamurty, and C.N.R. Rao, *Mechanical properties of inorganic nanowire reinforced polymer–matrix composites*. Nanotechnology, 2006. **17**(11): p. S344.
8. Njuguna, J., K. Pielichowski, and S. Desai, *Nanofiller-reinforced polymer nanocomposites*. Polymers for Advanced Technologies, 2008. **19**(8): p. 947-959.
9. Coleman, J.N., et al., *Small but strong: A review of the mechanical properties of carbon nanotube-polymer composites*. Carbon, 2006. **44**(9): p. 1624-1652.
10. Kojima, Y., et al., *Fine structure of nylon-6-clay hybrid*. Journal of Polymer Science. Part B: Polymer Physics, 1994. **32**: p. 625.
11. Paul, D.R. and L.M. Robeson, *Polymer nanotechnology: Nanocomposites*. Polymer, 2008. **49**(15): p. 3187-3204.
12. Kashiwagi, T., et al., *Thermal and flammability properties of polypropylene/carbon nanotube nanocomposites*. Polymer, 2004. **45**(12): p. 4227-4239.
13. Bernholc, J., et al., *Mechanical and electrical properties of nanotubes*. Annual Review Material Research, 2002. **32**(1): p. 347-375.
14. Fischer, H., *Polymer nanocomposites: From fundamental research to specific applications*. Materials Science and Engineering: C, 2003. **23**(6-8): p. 763-772.

15. Mai, Y. and Z. Yu, *Polymer Nanocomposite*. 2006, Cambridge: Woodhead and Maney Publishing.
16. Thomas, S. and E.G. Zaikov, *Progress in Polymer Nanocomposite Research*. 2008, New York: Nova Science Inc.
17. Jorio, A., G. Dresselhaus, and M.S. Dresselhaus, *Carbon nanotubes: Advanced Topics in the Synthesis, Structure, Properties and Applications*. Topics in Applied Physics. Vol. 111. 2008, Heidelberg: Springer.
18. Papazoglou, S.E., *Fire Retardant Materials*. 2001, Cambridge: Woodhead
19. Morgan, B.A. and A.C. Wilkie, *Flame Retardant Polymer Nanocomposites*. 2007, New Jersey: John Wiley & Sons.
20. Hussain, F., et al., *Review article: Polymer-matrix nanocomposites, processing, manufacturing and application: An overview*. Journal of Composite Material, 2006. **40**(17).
21. Messersmith, P.B. and E.P. Giannelis, *Synthesis and characterization of layered silicate-epoxy nanocomposites*. Chemistry of Materials, 1994. **6**(10): p. 1719-1725.
22. Yano, K., A. Usuki, and A. Okada, *Synthesis and properties of polyimide-clay hybrid films*. Journal of Polymer Science Part A: Polymer Chemistry, 1997. **35**(11): p. 2289-2294.
23. Kuilla, T., et al., *Recent advances in graphene based polymer composites*. Progress in Polymer Science, 2010. **35**(11): p. 1350-1375.
24. Stankovich, S., et al., *Graphene-based composite materials*. Nature, 2006. **442**(7100): p. 282-286.
25. Laoutid, F., et al., *New prospects in flame retardant polymer materials: From fundamentals to nanocomposites*. Materials Science and Engineering: R: Reports, 2009. **63**(3): p. 100-125.
26. MO., S., *Computational Multiscale Modeling of Solids and Fluids—Theory and Applications*. 2008, New York: Springer.
27. Saunders, J.H. and K.C. Frisch, *Polyurethane Chemistry and Technology Part II: Technology*. 1964, New York: John Wiley & Sons.
28. Petrovic, Z.S. and J. Ferguson, *Polyurethane elastomers*. Progress in Polymer Science, 1991. **16**(5): p. 695-836.

29. Chattopadhyay, D.K. and K.V.S.N. Raju, *Structural engineering of polyurethane coatings for high performance applications*. Progress in Polymer Science, 2007. **32**(3): p. 352-418.
30. Król, P., *Synthesis methods, chemical structures and phase structures of linear polyurethanes. Properties and applications of linear polyurethanes in polyurethane elastomers, copolymers and ionomers*. Progress in Materials Science, 2007. **52**(6): p. 915-1015.
31. Chattopadhyay, D.K. and D.C. Webster, *Thermal stability and flame retardancy of polyurethanes*. Progress in Polymer Science, 2009. **34**(10): p. 1068-1133.
32. Zdrahala, R.J. and I.J. Zdrahala, *Biomedical applications of polyurethanes: A review of past promises, present realities, and a vibrant future*. J Biomater Appl, 1999. **14**(1): p. 67-90.
33. Roland, C.M., et al., *High strain rate mechanical behavior of polyurea*. Polymer, 2007. **48**(2): p. 574-578.
34. Stenhouse, P.J., et al., *Thermal and rheological properties of a liquid-crystalline polyurethane*. Macromolecules, 1989. **22**(3): p. 1467-1473.
35. Hood, M.A., et al., *Morphology control of segmented polyurethanes by crystallization of hard and soft segments*. Polymer, 2010. **51**(10): p. 2191-2198.
36. Kasparek, E., et al., *Numerical and experimental studies of polyurethane foam under impact loading*. Computational Materials Science, 2011. **50**(4): p. 1353-1358.
37. Maw, J.R. and N.J. Whitworth, *Shock compression and the equation of state of fully dense and porous polyurethane*. AIP Conference Proceedings, 1998. **429**(1): p. 111-114.
38. Tekalur, S.A., A. Shukla, and K. Shivakumar, *Blast resistance of polyurea based layered composite materials*. Composite Structures, 2008. **84**(3): p. 271-281.
39. Bahei-El-Din, Y.A. and G.J. Dvorak, *Behavior of sandwich plates reinforced with polyurethane/polyurea interlayers under blast loads*. Journal of Sandwich Structures and Materials, 2007. **9**: p. 261.
40. Sarva, S.S., et al., *Stress-strain behavior of a polyurea and a polyurethane from low to high strain rates*. Polymer, 2007. **48**(8): p. 2208-2213.
41. Amirkhizi, A.V., et al., *An experimentally-based viscoelastic constitutive model for polyurea, including pressure and temperature effects*. Philosophical Magazine, 2006. **86**(36): p. 5847-5866.

42. Katsnelson, M.I., *Graphene: carbon in two dimensions*. Materials Today, 2007. **10**(1–2): p. 20-27.
43. Iijima, S., *Carbon nanotubes: past, present, and future*. Physica B: Condensed Matter, 2002. **323**(1–4): p. 1-5.
44. Iijima, S., *Helical microtubules of graphitic carbon*. Nature, 1991. **354**(6348): p. 56-58.
45. Kroto, H.W., et al., *C60: Buckminsterfullerene*. Nature, 1985. **318**(6042): p. 162-163.
46. Iijima, S. and T. Ichihashi, *Single-shell carbon nanotubes of 1-nm diameter*. Nature, 1993. **363**(6430): p. 603-605.
47. Saito, R., G. Dresselhaus, and M.S. Dresselhaus, *Physical Properties of Carbon Nanotubes*. 2004, London: Imperial College Press.
48. Rafii-Tabar, H., *Computational Physics of Carbon Nanotubes*. 2008, Cambridge: Cambridge University Press.
49. Katsnelson, I.M., *Graphene Carbon in two dimensions*. Materials Today, 2007. **10**(1–2).
50. Wallace, P.R., *The band theory of graphite*. Physical Review, 1947. **71**(9): p. 622-634.
51. McClure, J.W., *Diamagnetism of graphite*. Physical Review, 1956. **104**(3): p. 666-671.
52. Novoselov, K.S., et al., *Electric field effect in atomically thin carbon films*. Science, 2004. **306**(5296): p. 666-669.
53. Sun, X., et al., *Nano-graphene oxide for cellular imaging and drug delivery*. Nano Research, 2008. **1**(3): p. 203-212.
54. Gomez-Navarro, C., M. Burghard, and K. Kern, *Elastic properties of chemically derived single graphene sheets*. Nano Letters, 2008. **8**(7): p. 2045-2049.
55. Balandin, A.A., et al., *Superior thermal conductivity of single-layer graphene*. Nano Letters, 2008. **8**(3): p. 902-907.
56. Chen, J.-H., et al., *Intrinsic and extrinsic performance limits of graphene devices on SiO2*. Nature Nanotechnology, 2008(3): p. 206 - 209.

57. Ruoff, R.S., D. Qian, and W.K. Liu, *Mechanical properties of carbon nanotubes: theoretical predictions and experimental measurements*. Comptes Rendus Physique, 2003. **4**(9): p. 993-1008.
58. Rafii-Tabar, H., *Computational modelling of thermo-mechanical and transport properties of carbon nanotubes*. Physics Reports, 2004. **390**(4-5): p. 235-452.
59. Krishnan, A., et al., *Young's modulus of single-walled nanotubes*. Physical Review B, 1998. **58**(20): p. 14013-14019.
60. Liu, L. and Z. Shen, *Bandgap engineering of graphene: A density functional theory study*. Applied Physics Letters, 2009. **95**(25): p. 252104-3.
61. Lu, J.P., *Elastic properties of carbon nanotubes and nanoropes*. Physical Review Letters, 1997. **79**(7): p. 1297-1300.
62. Gao, G., T. Cagin, and W.A. Goddard, *Energetics, structure, thermodynamic and mechanical properties of nanotubes*. Nanotechnology, 1998. **9**: p. 183-191.
63. Yu, M.F., B.S. Files, and R.S. Ruoff, *Tensile loading of ropes of single wall carbon nanotubes and their mechanical properties*. Phys. Rev. Lett, 2000. **84**: p. 5552-5555.
64. Salvetat, J.-P., et al., *Elastic and shear moduli of single-walled carbon nanotube ropes*. Physical Review Letters, 1999. **82**(5): p. 944-947.
65. Belytschko, T., et al., *Atomistic simulations of nanotube fracture*. Phys. Rev. B, 2002. **65**: p. 235430.
66. Kudin, K.N., G.E. Scuseria, and B.I. Yakobson, *Nanoshell elasticity from ab Initio computations*. Phys. Rev. B, 2001. **64**: p. 235406.
67. Lee, C., et al., *Measurement of the elastic properties and intrinsic strength of monolayer graphene*. Science, 2008. **321**(5887): p. 385-388.
68. Ricardo, F., et al., *Mechanical properties of graphene nanoribbons*. Journal of Physics: Condensed Matter, 2009. **21**(28): p. 285304.
69. Van Lier, G., et al., *Ab initio study of the elastic properties of single-walled carbon nanotubes and graphene*. Chemical Physics Letters, 2000. **326**(1-2): p. 181-185.
70. Sánchez-Portal, D., et al., *Ab initio structural, elastic, and vibrational properties of carbon nanotubes*. Physical Review B, 1999. **59**(19): p. 12678-12688.
71. Awasthi, A.P., D.C. Lagoudas, and D.C. Hammerand, *Modeling of graphene-polymer interfacial mechanical behavior using molecular dynamics*. Modelling and Simulation in Materials Science and Engineering, 2009(1): p. 015002.

72. Lin, Y.-M., et al., *Operation of graphene transistors at gigahertz frequencies*. Nano Letters, 2008. **9**(1): p. 422-426.
73. Li, X., et al., *Large-area synthesis of high-quality and uniform graphene films on copper foils*. Science, 2009. **324**(5932): p. 1312-1314.
74. Geim, A.K., *Graphene: Status and prospects*. Science, 2009. **324**(5934): p. 1530-1534.
75. Al-Mashat, L., et al., *Graphene/polyaniline nanocomposite for hydrogen sensing*. Journal of Physical Chemistry C, 2010. **114**(39): p. 16168-16173.
76. Subrahmanyam, K.S., et al., *Chemical storage of hydrogen in few-layer graphene*. Proceedings of the National Academy of Sciences, 2011.
77. Zhang, Q.A., et al., *Fabrication of a biocompatible and conductive platform based on a single-stranded DNA/graphene nanocomposite for direct electrochemistry and electrocatalysis*. Chemistry-a European Journal, 2010. **16**(27): p. 8133-8139.
78. Park, S., et al., *Graphene-based actuators*. Small, 2010. **6**(2): p. 210-212.
79. Park, S. and R.S. Ruoff, *Chemical methods for the production of graphenes*. Nat Nano, 2009. **4**(4): p. 217-224.
80. Geim, A.K. and K.S. Novoselov, *The rise of graphene*. Nature Materials, 2007. **6**(3): p. 183-191.
81. Kim, H., Y. Miura, and C.W. Macosko, *Graphene/polyurethane nanocomposites for improved gas barrier and electrical conductivity*. Chemistry of Materials, 2010. **22**(11): p. 3441-3450.
82. Kim, H., A.A. Abdala, and C.W. Macosko, *Graphene/polymer nanocomposites*. Macromolecules, 2010. **43**(16): p. 6515-6530.
83. Gong, L., et al., *Interfacial Stress Transfer in a Graphene Monolayer Nanocomposite*. Advanced Materials, 2010. **22**(24): p. 2694-+.
84. Fukushima, H., et al., *Thermal conductivity of exfoliated graphite nanocomposites*. Journal of Thermal Analysis and Calorimetry, 2006. **85**(1): p. 235-238.
85. Ramanathan, T., et al., *Functionalized graphene sheets for polymer nanocomposites*. nature nanotechnology, 2008. **3**: p. 327-331.
86. Sakhaee-Pour, A., . *Elastic properties of single-layered graphene sheet*. Solid State Communications, 2009. **149**(1-2): p. 91-95.

87. Zhang, H.-B., et al., *Electrically conductive polyethylene terephthalate/graphene nanocomposites prepared by melt compounding*. *Polymer*, 2010. **51**(5): p. 1191-1196.
88. Kim, I.-H. and Y.G. Jeong, *Poly(lactide)/exfoliated graphite nanocomposites with enhanced thermal stability, mechanical modulus, and electrical conductivity*. *Journal of Polymer Science Part B: Polymer Physics*, 2010. **48**(8): p. 850-858.
89. Kim, S., I. Do, and L.T. Drzal, *Thermal stability and dynamic mechanical behavior of exfoliated graphite nanoplatelets-LLDPE nanocomposites*. *Polymer Composites*, 2010. **31**(5): p. 755-761.
90. Kalaitzidou, K., H. Fukushima, and L.T. Drzal, *Mechanical properties and morphological characterization of exfoliated graphite-polypropylene nanocomposites*. *Composites Part A: Applied Science and Manufacturing*, 2007. **38**(7): p. 1675-1682.
91. Tkalya, E., et al., *Latex-based concept for the preparation of graphene-based polymer nanocomposites*. *Journal of Materials Chemistry*, 2010. **20**(15): p. 3035-3039.
92. Lee, H.B., et al., *Preparation and characterization of poly(ethylene oxide)/graphene nanocomposites from an aqueous medium*. *Journal of Macromolecular Science, Part B*, 2010. **49**(4): p. 802-809.
93. Kalaitzidou, K., H. Fukushima, and L.T. Drzal, *Multifunctional polypropylene composites produced by incorporation of exfoliated graphite nanoplatelets*. *Carbon*, 2007. **45**(7): p. 1446-1452.
94. Yu, A., et al., *Graphite nanoplatelet-epoxy composite thermal interface materials*. *The Journal of Physical Chemistry C*, 2007. **111**(21): p. 7565-7569.
95. Veca, L.M., et al., *Carbon nanosheets for polymeric nanocomposites with high thermal conductivity*. *Advanced Materials*, 2009. **21**(20): p. 2088-2092.
96. Teng, C.-C., et al., *Thermal conductivity and structure of non-covalent functionalized graphene/epoxy composites*. *Carbon*, 2011. **49**(15): p. 5107-5116.
97. Flory, A.L., T. Ramanathan, and L.C. Brinson, *Physical aging of single wall carbon nanotube polymer nanocomposites: Effect of functionalization of the nanotube on the enthalpy relaxation*. *Macromolecules*, 2010. **43**(9): p. 4247-4252.
98. Salavagione, H.J. and G. Martínez, *Importance of covalent linkages in the preparation of effective reduced graphene oxide-poly(vinyl chloride) nanocomposites*. *Macromolecules*, 2011. **44**(8): p. 2685-2692.
99. Xu, Y., et al., *Strong and ductile poly(vinyl alcohol)/graphene oxide composite films with a layered structure*. *Carbon*, 2009. **47**(15): p. 3538-3543.

100. Rafiee, M.A., et al., *Enhanced mechanical properties of nanocomposites at low graphene content*. *ACS Nano*, 2009. **3**(12): p. 3884-3890.
101. Liang, J., et al., *Molecular-level dispersion of graphene into poly(vinyl alcohol) and effective reinforcement of their nanocomposites*. *Advanced Functional Materials*, 2009. **19**(14): p. 2297-2302.
102. Kai, W., et al., *Thermal and mechanical properties of a poly( $\epsilon$ -caprolactone)/graphite oxide composite*. *Journal of Applied Polymer Science*, 2008. **107**(3): p. 1395-1400.
103. Jang, J.Y., et al., *Graphite oxide/poly(methyl methacrylate) nanocomposites prepared by a novel method utilizing macroazoinitiator*. *Composites Science and Technology*, 2009. **69**(2): p. 186-191.
104. Lee, Y.R., et al., *Properties of waterborne polyurethane/functionalized graphene sheet nanocomposites prepared by an in situ method*. *Macromolecular Chemistry and Physics*, 2009. **210**(15): p. 1247-1254.
105. Balandin, A.A., *Thermal properties of graphene and nanostructured carbon materials*. *Nature Materials*, 2011. **10**(8): p. 569-581.
106. Lewandowska, M., et al., *Structure and properties of nano-sized Eurofer 97 steel obtained by hydrostatic extrusion*. *Journal of Nuclear Materials*, 2009. **386-388**(0): p. 499-502.
107. Dobb, M.G., D.J. Johnson, and B.P. Saville, *Supramolecular structure of a high-modulus polyaromatic fiber (Kevlar 49)*. *Journal of Polymer Science: Polymer Physics Edition*, 1977. **15**(12): p. 2201-2211.
108. Becerano, J., *Prediction of polymer properties*, ed. 3rd. 2002, New York: Dekkar.
109. Barun, D. and et al., *Nano-indentation studies on polymer matrix composites reinforced by few-layer graphene*. *Nanotechnology*, 2009. **20**(12): p. 125705.
110. Callister, D.W., *Material Science and Engineering: An Introduction*. 2007, New York: John Wiley & Sons.
111. Stølen, S. and T. Grande, *Thermodynamics of materials: Macroscopic and Microscopic Aspects*. 2004, Wes Sussex. England: John Wiley & Sons.
112. Gelin, R.B., *Molecular Modeling of Polymer Structures and Properties*. 1994, Ohio: Hanser.



113. Chakrabarty, A., *Carbon Nanotubes polymer nanocomposites for electromechanical system applications*, in *Chemical Engineering* 2008, Texas A&M University: College Station, Tx. p. 257.
114. Glotzer, S.C. and W. Paul, *Molecular and Mesoscale Simulation Methods for Polymer Materials*. Annual Review Material Research, 2002. **32**(1): p. 401-436.
115. Kittel, C., *Introduction to Solid State Physics*. Fifth ed. 1976, New York: John Wiley and Sons.
116. Shankar, R., *Principles of Quantum Mechanics*. 2nd ed. 1994: Kluwer Academic/Plenum.
117. Parr, G.R. and Y. Weitao, *Density Functional Theory of Atoms and Molecules*. 1994: Oxford University Press.
118. Dreizler, R.M. and U.K.E. Gross, *Density Functional Theory*. 1990, Berlin: Springer.
119. Kohn, W. and L.J. Sham, *Self consistent equations including exchange and correlation effects*. Physical Review, 1965. **140**(4A): p. A1133-A1138.
120. Hafner, J., *Atomic-scale computational materials science*. Acta Materialia, 2000. **48**(1): p. 71-92.
121. Perdew, J.P., K. Burke, and M. Ernzerhof, *Generalized gradient approximation made simple*. Physical Review Letters, 1996. **77**(18): p. 3865-3868.
122. Haile, J.M., *Molecular Dynamics Simulation ;Elementary methods*. 1992, New York: John Wiley and Sons Inc.
123. Frenkel, D. and B. Smit, *Understanding Molecular Simulation: From Algorithms to Applications*. Vol. 1. 1996, San Diego, California: Academic Press.
124. Mayo, S.L., B.D. Olafson, and W.A. Goddard, *Dreiding: A generic force field for molecular simulations*. The Journal of Physical Chemistry, 1990. **94**(26): p. 8897-8909.
125. Sane, S.B., et al., *Molecular dynamics simulations to compute the bulk response of amorphous PMMA*. Journal of Computer-Aided Materials Design, 2002. **8**(2-3): p. 87-106.
126. Fan, C.F., et al., *Molecular modeling of polycarbonate: Force-Field, static structure, and mechanical properties*. Macromolecules, 1994. **27**(9): p. 2383-2391.
127. Gersten, J.I. and W.F. Smith, *The Physics and Chemistry of Materials*. 2001, New York: John Wiley & Sonce.

128. Cadelano, E., et al., *Elastic properties of hydrogenated graphene*. Physical Review B, 2010. **82**(23): p. 235414.
129. Andrew, R.C., et al., *Mechanical properties of graphene and boronitrene*. Physical Review B, 2012. **85**(12): p. 125428.
130. Huang, Y., J. Wu, and K.C. Hwang, *Thickness of graphene and single-wall carbon nanotubes*. Physical Review B, 2006. **74**(24): p. 245413.
131. Scarpa, F., S. Adhikari, and A.S. Phani, *Effective elastic mechanical properties of single layer graphene sheets*. Nanotechnology, 2009. **20**(6): p. 065709.
132. Lee, C., et al., *Frictional characteristics of atomically thin sheets*. Science, 2010. **328**(5974): p. 76-80.
133. Gómez-Navarro, C., M. Burghard, and K. Kern, *Elastic properties of chemically derived single graphene sheets*. Nano Letters, 2008. **8**(7): p. 2045-2049.
134. Poot, M. and H.S.J. van der Zant, *Nanomechanical properties of few-layer graphene membranes*. Applied Physics Letters, 2008. **92**(6): p. 063111-3.
135. Kudin, K.N., G.E. Scuseria, and B.I. Yakobson, *C<sub>2</sub>F, BN, and C nanoshell elasticity from ab initio computations*. Physical Review B, 2001. **64**(23): p. 235406.
136. Liu, F., P. Ming, and J. Li, *Ab initio calculation of ideal strength and phonon instability of graphene under tension*. Physical Review B, 2007. **76**(6): p. 064120.
137. Wei, X., et al., *Nonlinear elastic behavior of graphene: Ab initio calculations to continuum description*. Physical Review B, 2009. **80**(20): p. 205407.
138. Zhao, H., K. Min, and N.R. Aluru, *Size and chirality dependent elastic properties of graphene nanoribbons under uniaxial tension*. Nano Letters, 2009. **9**(8): p. 3012-3015.
139. Donald, W.B., et al., *A second-generation reactive empirical bond order (REBO) potential energy expression for hydrocarbons*. Journal of Physics: Condensed Matter, 2002. **14**(4): p. 783.
140. Khare, R., et al., *Multiscale coupling schemes spanning the quantum mechanical, atomistic forcefield, and continuum regimes*. Computer Methods in Applied Mechanics and Engineering, 2008. **197**(41–42): p. 3190-3202.
141. Khare, R., et al., *Coupled quantum mechanical/molecular mechanical modeling of the fracture of defective carbon nanotubes and graphene sheets*. Physical Review B, 2007. **75**(7): p. 075412.

142. Khare, R., et al., *A simple energy-scaling scheme for fine-tuning empirical potentials for coupled quantum mechanical/molecular mechanical studies*. Chemical Physics Letters, 2008. **460**(1–3): p. 311-314.
143. Pokluda, J., et al., *Calculations of theoretical strength: State of the art and history*. Journal of Computer-Aided Materials Design, 2004. **11**(1): p. 1-28.
144. Birch, F., *Finite strain isotherm and velocities for single-crystal and polycrystalline NaCl at high pressures and 300°K*. J. Geophys. Res., 1978. **83**(B3): p. 1257-1268.
145. Ziambaras, E. and E. Schröder, *Theory for structure and bulk modulus determination*. Physical Review B, 2003. **68**(6): p. 064112.
146. Cagin, T. and J.R. Ray, *3rd order elastic constants from molecular dynamics: Theory and an example calculation*. Physical Review B, 1988. **38**(12): p. 7940-7946.
147. Cagin, T. and B.M. Pettitt, *Elastic constants of nickel - variations with respect to temperature and pressure*. Physical Review B, 1989. **39**(17): p. 12484-12491.
148. Barua, B.P. and S.K. Sinha, *Pseudopotential of gold fitted to elastic data*. Journal of Applied Physics, 1978. **49**(7): p. 3967-3969.
149. Chantasiriwan, S. and F. Milstein, *Embedded-atom models of 12 cubic metals incorporating second- and third-order elastic-moduli data*. Physical Review B, 1998. **58**(10): p. 5996-6005.
150. Kresse, G. and J. Furthmüller, *Efficient iterative schemes for ab initio total-energy calculations using a plane-wave basis set*. Physical Review B, 1996. **54**(16): p. 11169-11186.
151. Tersoff, J., *Modeling solid-state chemistry: Interatomic potentials for multicomponent systems*. Physical Review B, 1989. **39**(8): p. 5566-5568.
152. Chenoweth, K., A.C.T. van Duin, and W.A. Goddard, *ReaxFF Reactive force field for molecular dynamics simulations of hydrocarbon oxidation*. The Journal of Physical Chemistry A, 2008. **112**(5): p. 1040-1053.
153. Hanfland, M., H. Beister, and K. Syassen, *Graphite under pressure: Equation of state and first-order Raman modes*. Physical Review B, 1989. **39**(17): p. 12598-12603.
154. Wang, R., et al., *First-principles calculations on third-order elastic constants and internal relaxation for monolayer graphene*. Physica B: Condensed Matter, 2010. **405**(16): p. 3501-3506.

155. Zhou, J. and R. Huang, *Internal lattice relaxation of single-layer graphene under in-plane deformation*. Journal of the Mechanics and Physics of Solids, 2008. **56**(4): p. 1609-1623.
156. Tersoff, J., *Empirical interatomic potential for carbon with applications to amorphous carbon*. Physical Review Letters, 1988. **61**(25): p. 2879-2882.
157. Al-Malaika, S., A. Golovoy, and C.A. Wilkie, *Chemistry and Technology of Polymer Additives*. 1999, Oxford,: Blackwell Sci,.
158. Moniruzzaman, M. and K.I. Winey, *Polymer Nanocomposites Containing Carbon Nanotubes*. Macromolecular Chemistry and Physics, 2006. **39**(16): p. 5194-5205.
159. Bilal Khan, M., *Intelligent viscoelastic polyurethane intrinsic nanocomposites*. Metallurgical and Materials Transactions A, 2010. **41**(4): p. 876-880.
160. Brown, D. and J.H.R. Clarke, *Molecular dynamics simulation of an amorphous polymer under tension: Phenomenology*. Macromolecules, 1991. **24**(8): p. 2075-2082.
161. Cagin, T., et al., *Thermodynamic and elastic properties of polyethylene at elevated temperatures*. Computational Methods in Materials Science, 1992. **278**: p. 61-66
- .
162. Sane, S., et al., *Molecular dynamics simulations to compute the bulk response of amorphous PMMA*. Journal of Computer-Aided Materials Design, 2001. **8**(2): p. 87-106.
163. Theodorou, D.N. and U.W. Suter, *Atomistic modeling of mechanical properties of polymeric glasses*. Macromolecules, 1986. **19**(1): p. 139-154.
164. Fedderly, J., E. Compton, and B. Hartmann, *Additive group contributions to density and glass transition temperature in polyurethanes*. Polymer Engineering & Science, 1998. **38**(12): p. 2072-2076.
165. Martienssen, W. and H. Warlimont, *Springer Handbook of Condensed Matter and Materials Data*. 2005, New York: Springer.
166. Grujicic, M., et al., *Molecular-level simulations of shock generation and propagation in polyurea*. Materials Science and Engineering: A, 2011. **528**(10-11): p. 3799-3808.
167. Grujicic, M., W.C. Bell, and B. Pandurangan, *Design and material selection guidelines and strategies for transparent armor systems*. Materials & Design, 2012. **34**(0): p. 808-819.

168. Knudson, M.D. and Y.M. Gupta, *Real time observation of a metastable state during the phase transition in shocked cadmium sulfide*. Physical Review Letters, 1998. **81**(14): p. 2938-2941.
169. Loveridge-Smith, A., et al., *Anomalous elastic response of silicon to uniaxial shock compression on nanosecond time scales*. Physical Review Letters, 2001. **86**(11): p. 2349-2352.
170. Kanel, I.G., V.S. Razorenov, and E.V. Fortov, *Shock-Wave Phenomena and the Properties of Condensed Matter*. 2004, New York: Springer.
171. Carter, J.W. and P.S. Marsha, *Hugoniot equation of state of polymers*. Los Alamos National Laboratory Report No. LA-13006-MS, 1995.
172. Meyers, M.A., *Dynamic Behavior of Materials*. 1994, New York: John Wiley.
173. Holian, B.L. and G.K. Straub, *Molecular dynamics of shock waves in three-dimensional solids: Transition from nonsteady to steady waves in perfect crystals and implications for the Rankine-Hugoniot conditions*. Physical Review Letters, 1979. **43**(21): p. 1598-1600.
174. Arman, B., A.S. Reddy, and G. Arya, *Viscoelastic properties and shock response of coarse-grained models of multiblock versus diblock copolymers: Insights into dissipative properties of polyurea*. Macromolecules, 2012. **45**(7): p. 3247-3255.
175. Holian, B.L., *Atomistic computer simulations of shock waves*. Shock Waves, 1995. **5**(3): p. 149-157.
176. Ben-Dor, C.I., O. Elperin, T., *Handbook of Shock Waves*. Vol. 1. 2001, California: Academic Press.
177. Bourne, N.K. and A.M. Milne, *Shock to detonation transition in a plastic bonded explosive*. Journal of Applied Physics, 2004. **95**(5): p. 2379-2385.
178. Accelrys Materials Studio, h.a.c. *Material Studio*. 2001-2007.
179. Berendsen, H.J.C., et al., *Molecular dynamics with coupling to an external bath*. The Journal of Chemical Physics, 1984. **81**(8): p. 3684-3690.
180. Arman, B., et al., *Dynamic response of phenolic resin and its carbon-nanotube composites to shock wave loading*. Journal of Applied Physics, 2011. **109**(1): p. 013503-7.
181. Davidson, L., *Fundamentals of Shock propagation in solids*. 2008, Berlin: Springer.

182. Barker, L.M. and R.E. Hollenbach, *Shock wave studies of PMMA, fused silica, and sapphire*. Journal of Applied Physics, 1970. **41**(10): p. 4208-4226.

## APPENDIX

### Dreiding/X 6 parameters used in the polyurethane system.

#### *Masses*

Atom type (9 )	Symbol	Atomic mass(amu)
Nitrogen	N_R	14.0067
Carbonyl carbon(c=o)	C_R	12.0115
Ester Oxygen	O_R	15.9994
Methyl carbon	C_2	12.01115
Carbonyl oxygen(c=o)	O_2	15.9994
Hydrogen involved in H-bonding	H_A	1.00797
Hydrogen	H_	1.00797
Carbon	C_3	12.01115
Nitrogen (with 1 hydrogen)	N_R	14.0067

#### *Bond parameters*

Bond type (12)	$r_o$ (Å)	$K_B$ (Kcal/mol)	$KB/2$
N_R-C_R	1.34	1050	525
N_R-H_A	0.97	700	350
N_R-C_3	1.41	700	350
C_R-O_R	1.35	1050	525
C_R-O_2	1.25	1400	700
O_R-C_3	1.42	700	350
C_3-C_3	1.53	700	350
C_3-H_	1.09	700	350
C_3-C_3	1.09	700	350
C_3-C_3	1.53	700	350
N_R-C_R	1.34	1050	525
N_R-H_A	0.97	700	350

#### *Van der Waals parameters*

Angle type	A (Kcal/m)	$\rho(1/A)$	C (Kcal/mol)
H_	3410.66	0.258015021	31.36677
C_3	88366.7	0.277775403	583.0177
C_2	88366.7	0.277775403	583.0177
O_R	55027.5	0.252510569	268.5464
O_2	55027.5	0.252510569	268.5464
H_A	16.2755	0.26625	0.212743
N_R	5818.88	0.264538034	31.49849

Angle parameters

Angle type (22)	$\phi_0$ (degree: $K_A$ (Kcal/mol)						
Angle type	$K_\phi$ (kcal/mol/rad <sup>2</sup> )	$\theta_j^\circ$ (degrees)	radians	$(\sin \theta_j)$	$(\sin \theta_j)^2$	$C_{ijk}$	$(C_{ijk})/2$ (kcal/mol/rad <sup>2</sup> )
X-N_R-X	100	120	2.094395	0.866025	0.75	133.3333	66.66667
X-N_R-X	100	120	2.094395	0.866025	0.75	133.3333	66.66667
X-N_R-X	100	120	2.094395	0.866025	0.75	133.3333	66.66667
X_C_R-X	100	120	2.094395	0.866025	0.75	133.3333	66.66667
X_C_R-X	100	120	2.094395	0.866025	0.75	133.3333	66.66667
X_C_R-X	100	120	2.094395	0.866025	0.75	133.3333	66.66667
X-O_R-X	100	120	2.094395	0.866025	0.75	133.3333	66.66667
X-C_3-X	100	109.471	1.910629	0.94281	0.888891	112.4997	56.24985
X-C_3-X	100	109.471	1.910629	0.94281	0.888891	112.4997	56.24985
X-C_3-X	100	109.471	1.910629	0.94281	0.888891	112.4997	56.24985
X-C_3-X	100	109.471	1.910629	0.94281	0.888891	112.4997	56.24985
X-C_3-X	100	109.471	1.910629	0.94281	0.888891	112.4997	56.24985
X-C_3-X	100	109.471	1.910629	0.94281	0.888891	112.4997	56.24985
X-C_3-X	100	109.471	1.910629	0.94281	0.888891	112.4997	56.24985
X-C_3-X	100	109.471	1.910629	0.94281	0.888891	112.4997	56.24985
X-C_3-X	100	109.471	1.910629	0.94281	0.888891	112.4997	56.24985
X-C_3-X	100	109.471	1.910629	0.94281	0.888891	112.4997	56.24985
X-C_3-X	100	109.471	1.910629	0.94281	0.888891	112.4997	56.24985
X-C_3-X	100	109.471	1.910629	0.94281	0.888891	112.4997	56.24985
X-N_R-X	100	120	2.094395	0.866025	0.75	133.3333	66.66667
X-N_R-X	100	120	2.094395	0.866025	0.75	133.3333	66.66667
X_C_R-X	100	120	2.094395	0.866025	0.75	133.3333	66.66667
X_C_R-X	100	120	2.094395	0.866025	0.75	133.3333	66.66667



*Torsion parameters*

Angle type (26)	$\phi_0$ (degree)	n	$K_A$ (Kcal/mol)
X-N_R-C_R-O_R	1	2	25
X-N_R-C_R-o_2	1	2	25
N_R-C_R-O_R-X	1	6	1
O_2-C_R-O_R-X	1	6	1
C_R-O_R-C_3-X	1	6	1
C_R-O_R-C_3-X	1	6	1
X-C_3-C_3-X	-1	3	2
X-C_3-C_3-X	-1	3	2
X-C_3-C_3-X	-1	3	2
X-C_3-C_3-X	-1	3	2
X-C_3-C_3-X	-1	3	2
N_R-C_R-O_R-X	1	6	1
X-C_R-N_R-X	1	2	25
X-N_R-C_R-X	1	2	25
X-C_R-N_R-X	1	2	25
o_2-C_R-N_R-X	1	2	25
X-C_3-N_R-X	-1	3	2
X-C_3-N_R-C_R	-1	3	2
X-C_3-N_R-X	-1	3	2
X-C_3-N_R-X	-1	3	2
X-C_3-C_3-X	-1	3	2
X-C_3-C_3-X	-1	3	2
X-C_3-C_3-X	-1	3	2
X-C_3-C_3-X	-1	3	2
X-C_3-C_3-X	-1	3	2
X-C_3-C_3-X	-1	3	2
X-C_3-C_3-X	-1	3	2
X-C_3-C_3-X	-1	3	2